

Copyright Warning & Restrictions

The copyright law of the United States (Title 17, United States Code) governs the making of photocopies or other reproductions of copyrighted material.

Under certain conditions specified in the law, libraries and archives are authorized to furnish a photocopy or other reproduction. One of these specified conditions is that the photocopy or reproduction is not to be “used for any purpose other than private study, scholarship, or research.” If a user makes a request for, or later uses, a photocopy or reproduction for purposes in excess of “fair use” that user may be liable for copyright infringement,

This institution reserves the right to refuse to accept a copying order if, in its judgment, fulfillment of the order would involve violation of copyright law.

Please Note: The author retains the copyright while the New Jersey Institute of Technology reserves the right to distribute this thesis or dissertation

Printing note: If you do not wish to print this page, then select “Pages from: first page # to: last page #” on the print dialog screen

The Van Houten library has removed some of the personal information and all signatures from the approval page and biographical sketches of theses and dissertations in order to protect the identity of NJIT graduates and faculty.

ABSTRACT

HIGH RESOLUTION SOLAR OBSERVATIONS IN THE CONTEXT OF SPACE WEATHER PREDICTION

**by
Guo Yang**

Space weather has a great impact on the Earth and human life. It is important to study and monitor active regions on the solar surface and ultimately to predict space weather based on the Sun's activity. In this study, a system that uses the full power of speckle masking imaging by parallel processing to obtain high-spatial resolution images of the solar surface in near real-time has been developed and built. The application of this system greatly improves the ability to monitor the evolution of solar active regions and to predict the adverse effects of space weather. The data obtained by this system have also been used to study fine structures on the solar surface and their effects on the upper solar atmosphere.

A solar active region has been studied using high resolution data obtained by speckle masking imaging. Evolution of a pore in an active region presented. Formation of a rudimentary penumbra is studied. The effects of the change of the magnetic fields on the upper level atmosphere is discussed.

Coronal Mass Ejections (CMEs) have a great impact on space weather. To study the relationship between CMEs and filament disappearance, a list of 431 filament and prominence disappearance events has been compiled. Comparison of this list with CME data obtained by satellite has shown that most filament disappearances seem to have no corresponding CME events. Even for the limb events, only thirty percent of filament disappearances are associated with CMEs.

A CME event that was observed on March 20, 2000 has been studied in detail. This event did not show the three-parts structure of typical CMEs. The kinematical and morphological properties of this event were examined.

**HIGH RESOLUTION SOLAR OBSERVATIONS
IN THE CONTEXT OF SPACE WEATHER PREDICTION**

by
Guo Yang

**A Dissertation
Submitted to the Faculty of
New Jersey Institute of Technology and
Rutgers, the State University of New Jersey - Newark
in Partial Fulfillment of the Requirements for the Degree of
Doctor of Philosophy**

Federated Physics Department

January 2004

**Copyright © 2004 by Guo Yang
ALL RIGHTS RESERVED**

APPROVAL PAGE

**HIGH RESOLUTION SOLAR OBSERVATIONS
IN THE CONTEXT OF SPACE WEATHER PREDICTION**

Guo Yang

Dr. Haimin Wang, Thesis Advisor Date
Professor of Physics, Associate Director of Center for
Solar-Terrestrial Research and Big Bear Solar Observatory, NJIT

Dr. Carsten Denker, Co-advisor Date
Assistant Professor of Physics, NJIT

Dr. Phil Goode, Committee Member Date
Distinguished Professor of Physics, Director of Center for
Solar-Terrestrial Research and Big Bear Solar Observatory, NJIT

Dr. Dale Gary, Committee Member Date
Professor of Physics, Director of Solar Array
in Owens Valley Radio Observatory, NJIT

Dr. Zhen Wu, Committee Member Date
Associate Professor of Physics,
Rutgers University, Newark

BIOGRAPHICAL SKETCH

Author: Guo Yang
Degree: Degree of Philosophy
Date: January 2004

Undergraduate and Graduate Education:

- Doctor of Philosophy in Applied Physics,
New Jersey Institute of Technology, Newark, New Jersey, 2004
- Master of Science in Astronomy,
Nanjing University, Nanjing, China, 1998
- Bachelor of Science in Astronomy,
Nanjing University, Nanjing, China, 1995

Major: Applied Physics

Publications in Refereed Journals:

- Yang, Guo; Xu Yan; Wang, Haimin & Denker, C., 2003, *High-Spatial Resolution Observations of Pores and the Formation of a Rudimentary Penumbra*, *Astrophysical Journal*, 597, 1190.
- Denker, Carsten; Yang, Guo & Wang, Haimin, 2001, *Near Real-Time Image Reconstruction*, *Solar Physics*, 202, 63.
- Moon, Y.-J.; Choe, G. S.; Wang, Haimin; Park, Y. D.; Gopalswamy, N.; Yang, Guo & Yashiro, S., 2002, *A Statistical Study of Two Classes of Coronal Mass Ejections*, *Astrophysical Journal*, 581, 694.
- Wang, Haimin; Gallagher, Peter; Yurchyshyn, Vasyl; Yang, Guo & Goode, Philip R., 2002, *Core and Large-Scale Structure of the 2000 November 24 X-Class Flare and Coronal Mass Ejection*, *Astrophysical Journal*, 569, 1026
- Wang, Haimin; Yurchyshyn, Vasyl; Chae, Jongchul; Yang, Guo; Steinegger, Michael & Goode, Philip, 2001, *Inter-Active Region Connection of Sympathetic Flaring on 2000 February 17*, *Astrophysical Journal*, 559, 1171
- Wang, Haimin; Goode, Philip R.; Denker, Carsten; Yang, Guo; Yurchishin, Vasyl; Nitta, Nariaki; Gurman, Joseph B.; St. Cyr, Chris & Kosovichev, Alexander G., 2000, *Comparison of the 1998 April 29 M6.8 and 1998 November 5 M8.4 Flares*, *Astrophysical Journal*, 536, 971
- Fu, Q.; Liu, Y.; Ji, H.; Cheng, Z.; Lao, D.; Qin, Z. & Yang, G., 1998, *A Broadband Radiospectrometer and Fine Structures in Microwave Bursts*, in: *Proceedings of the Nobeyama Symposium*, Kiyosato, Japan, T. S. Bastian, N. Gopalswamy, and K. Shibasaki (eds.), NRO Report No. 479, p. 433.

Publications in Conferences:

- Yang, Guo & Wang, Haimin, 2001, *Statistical Studies of Filament Disappearances and CMEs*, COSPAR Colloquium on Solar-Terrestrial Magnetic Activity and Space Environment, Beijing, China.
- Yang, Guo; Denker, Carsten; Xu, Yan & Wang, H., 2003, *Speckle Masking Imaging of Solar Active Regions*, in: *Current Theoretical Models and Future High Resolution Solar Observations: Preparing for ATST*, A. A. Pevtsov and H. Uitenbroek (eds.), ASP Conference Series, in press.
- Huang, G.L.; Yang, G. & Liu, Y. Y., 1998, *Energetic Spectrum of Non-Thermal Electrons Responsible for Solar Type III Bursts Close to Acceleration Region*, CESRA Workshop on Coronal Explosive Events, Metsaehovi Publications on Radio Science, HUT-MET-27, 1998, p. 73.

**This dissertation is dedicated to
Furen Yang and Liange Pang**

ACKNOWLEDGMENT

I wish to express my sincere gratitude to my advisor, Dr. Haimin Wang for his guidance, support throughout this research. Words are inadequate to express my appreciation for him who is always patient with his students. There seems to be no limit to his wisdom and his selfless concern for the students.

I also owe great debt of gratitude to my co-advisor, Dr. Carsten Denker. He guided me in the study of the speckle masking imaging. Dr. Denker also gave me a lot of help during writing of several papers. He is always ready to help and is always patient with his students.

I would like to thank Dr. Phil Goode, Dr. Dale Gary, and Dr. Zhen Wu, specially for taking time to be committee members. They spent a lot of precious time reviewing my dissertation and helping me to improve it. I appreciate their valuable help.

I appreciate the help and suggestions from Dr. Jiong Qiu during the course of the study. I would also like to thank Yan Xu for testing my programs tirelessly and the enormous amount of excellent feedbacks.

I would like to thank Drs. Richard Shine and Louis Strous (Lockheed Martin Solar and Astrophysics Laboratory) for providing the ANA/C code and DLMS that implement Local Correlation Tracking (LCT) in IDL and Drs. Franz Kneer and Claus-Rüdiger de Boer (Universitäts-Sternwarte Göttingen) for providing the original version of the IDL speckle masking algorithms. Also, I thank also to William H. Marquette, Jeff Nenow, Randy J. Fear, Thomas J. Spirock, and the BBSO observing staff for their assistance and support.

This work is supported by NASA and NSF through a number of grants.

TABLE OF CONTENTS

Chapter	Page
1 INTRODUCTION	1
1.1 The Need to Monitor and Study Space Weather	1
1.2 Overview of Relevant Solar Characteristics and Activities	3
1.3 Seeing Problem and The Need to Process Images in Real Time	7
1.4 The Goal of This Study	11
2 IMAGE PROCESSING	13
2.1 Preprocessing	13
2.1.1 Dark Current Frames	13
2.1.2 Flat Field Frames	14
2.2 Image Motion and Differential Image Motion	15
2.3 Speckle Masking Method	16
2.3.1 Speckle Interferometry	18
2.3.2 Speckle Masking Bi-spectrum	22
2.3.3 Reassembly of the Reconstructed Isoplanatic Patches	24
2.4 Rigid Alignment and Destretching of Reconstructed Time Series	24
2.5 Subsonic Filter	25
2.6 Local Correlation Tracking	26
3 IMPLEMENTING THE REAL-TIME IMAGE RECONSTRUCTION SYSTEM	28
3.1 Introduction	28
3.2 Hardware and Software Environment of RTIR System	32
3.2.1 Hardware Environment of RTIR System	32
3.2.2 Software Environment	34

TABLE OF CONTENTS
(Continued)

Chapter	Page
3.3 Test System	35
3.4 Implementation	39
3.4.1 Speckle Masking Algorithm	39
3.4.2 Camera Control Interface	40
3.4.3 Parallel Implementation of Speckle Masking Method	42
3.5 Results and Discussion	46
4 SPECKLE MASKING IMAGING OF SOLAR ACTIVE REGION NOAA 9539	49
4.1 Introduction	49
4.2 Observations	50
4.3 Data Reduction	51
4.4 Results	55
4.5 Discussion	57
5 FORMATION OF A RUDIMENTARY PENUMBRA	59
5.1 Introduction	59
5.2 Observations	63
5.3 Data Reduction	66
5.3.1 Data Preprocessing	66
5.3.2 Image Reconstruction	67
5.3.3 Calibration of the Line-of-Sight Magnetograms	68
5.3.4 Local Correlation Tracking	69
5.4 Results	71
5.4.1 Magnetic Field Evolution	73

TABLE OF CONTENTS
(Continued)

Chapter	Page
5.4.2 Ellerman Bombs	77
5.4.3 H α Filaments	79
5.4.4 Photospheric and Chromospheric Flow Fields	83
5.5 Summary	86
6 STATISTICAL STUDIES OF FILAMENT DISAPPEARANCES AND CMES	89
6.1 Introduction	89
6.2 Observations and Results	90
6.3 Discussion	93
7 A HIGHLY HELICAL CME OBSERVED BY LASCO AND EIT	95
7.1 Introduction	95
7.2 Coronal Mass Ejection of 2000 March 20	97
7.2.1 LASCO Data	97
7.2.2 EIT Data	101
7.3 Discussion	111
8 SUMMARY AND DISCUSSION	114
REFERENCES	117

LIST OF TABLES

Table	Page
1.1 The Sun's Basic Physical Characteristics	3
1.2 The Hierarchy of Solar Magnetic Structures	12
5.1 Observing Characteristics on 2001 July 15	61
5.2 Local Correlation Tracking	68
6.1 Part of the Filament Disappearance Data	91

LIST OF FIGURES

Figure	Page
1.1 The Sun's magnetic field and releases of plasma directly affect the space weather very much. Space weather can effect the near Earth environment, e. g., astronaut safety, interior and surface charging of satellites, computer and memory upsets and failures on satellites, damage to solar cells, an increased atmospheric drag in Low Earth Orbit (LEO), an increase of airline passenger radiation on polar routes, disturbances of radio wave communication, disruptions in telecommunication cables, interruptions in power distribution systems, and induction of earth currents corroding pipelines. In this figure, solar wind shapes the Earth's magnetosphere and magnetic storms are illustrated as approaching the Earth.	2
1.2 Big Bear Solar Observatory (BBSO) is located in a high mountain lake in the southern California. The unique weather condition and geographical location make BBSO an ideal site for daytime solar observations.	8
2.1 Schematic representation of the dark and flat field image calibration procedure. The image gradient visible in the raw data and the artifacts due to dust particles on the CCD chip have been removed. Note that the image panels were scaled individually, thus, contrasts are not directly comparable.	15
2.2 Same schematic as in Figure 2.1, however, here the dark and flat filed calibration procedures were applied to defocused raw images. These data are used in the signal-to-noise estimation process and as one can see only some large scale features and salt-and-pepper noise is left in the images. The image panels were scaled individually, thus, contrasts are not directly comparable.	16
2.3 Modified Hanning function as apodisation window for isoplanatic patches. . . .	17
3.1 A schematic view of the Near Real-Time Imaging Reconstruction system at BBSO.	33
3.2 A schematic view of the test system that was used to develop the RTIR system.	36
3.3 The overall procedure of the speckle masking imaging method. The parallelograms denote data sets that are used or produced during the processing. The rectangles denote operations on the data.	37
3.4 The flow diagram for computing the Fried-Parameter, r_0 , generating the amplitude calibration and optimum noise filter.	38

LIST OF FIGURES
(Continued)

Figure	Page
3.5 The flow diagram showing the estimation of Fourier amplitudes and the phases and getting the reconstructed isoplanatic patch through inverse FFT.	41
3.6 The data flow diagram of the RITR system. Note that only part of the data exchange between the nodes during the parallel processing are displayed in the figure. The figure does not represent the real configuration of the cluster used in the RITR system. Three nodes are drawn to illustrate the principal of the system.	44
3.7 Speckle reconstruction of active region NOAA 10375 on 2003 June 10 at 19:58 UT. The Fried-parameter was $r_0 = 13.2$ cm.	47
4.1 A speckle reconstructed image of the central part of active region NOAA 9439 observed at 20:14 UT on July 15, 2001.	52
4.2 Flow map of the horizontal proper motions derived from a 75-minute time series of speckle reconstructed images.	53
4.3 Dopplergram taken at 20:14 UT on July 15, 2001. The white box corresponds to the region of the speckle observations. The arrow indicates the down-flow area.	54
4.4 The line-of-sight magnetic field observed at 20:12 UT an July 15, 2001. The white box corresponds to the region of the speckle observations.	55
4.5 The evolution of the penumbra-like structure before the defragmentation of the pore. The FOV of the individual panels is $7.62'' \times 7.62''$. The last frame shows the fragments of the pores which dissolved into magnetic knots. The white box indicates a region that contains a peculiar filamentary structure. The times are given in UT.	56
5.1 Temporal evolution of the Fried-parameter r_0 of BBSO on 2001 July 15.	65
5.2 Speckle reconstructed continuum images at 5200 \AA showing two pores at the central part of active region NOAA 9539 on 2001 July 15 at (a) 19:58 UT and (b) 20:32 UT, respectively. At 20:32 UT, an approximately $5'' \times 5''$ penumbral region, which indicated with an arrow in (b), has formed at the edge of the light-bridge separating the two pores. The arrow indicates the forming penumbra region. The FOV is about $28'' \times 28''$	67

LIST OF FIGURES
(Continued)

Figure	Page
5.3 Scatter plot of magnetic flux density B of the KPNO magnetogram as function of the degree of polarization ρ of the BBSO magnetogram.	70
5.4 Schematic sketch of the emerging flux region within active region NOAA 9539 (LB: light-bridge, FL: filament, RP: rudimentary penumbra, DC: dark channel, BMF: bipolar magnetic feature). The light grey area corresponds to the region of interest.	72
5.5 (a) Ca I 6103 Å line wing filtergram and (b) Line-of-sight magnetogram of NOAA 9539 observed with the Digital Vector Magnetograph at BBSO on 2001 July 15 at 21:03 UT. In the small leading image the relative position of the region shown in (a) and (b) to the disk center are displayed by the black box. The end of the arrow indicates the center of the solar disk. The black boxes in (a) and (b) indicates the region of interest, which corresponds to the location of the speckle reconstructed continuum images.	73
5.6 Temporal evolution of the magnetic flux of the dominant flux in the emerging bipolar magnetic feature. The solid line represents an exponential fit of a rise-time of 40 minutes approximately. The position angle of the active region was considered in the calculation.	75
5.7 Time sequence of H α red line wing ($6562.8 + 0.6$ Å) filtergrams depicting the temporal evolution of Ellerman Bombs, which were located near the tips of the newly formed penumbral filaments. Detailed view of Ellerman Bombs and filament activation at (a) 20:14 UT, (b) 20:25 UT, (c) 20:35 UT, and (d) 20:45 UT, respectively. The FOV is about $55'' \times 55''$. The big box in (a) indicates the region observed in white-light. The evolution of three Ellerman Bombs are shown in the region indicated by the small boxes in all the sub-images.	78

LIST OF FIGURES
(Continued)

Figure	Page	
5.8	Temporal evolution of (a) the peak intensity of three EBs (See Figure 5.7 for selected time sequence images), and (b) the curve of total surface brightness of the region that contains the EBs. At the beginning there were two EBs which are corresponding to the two leading curves in (a). They disappeared during the evolution. Later another one emerged at the same region which is described by the following curve in (a). It is hard to tell if it was recurrence of the older ones. The dip in (b) is caused by the disappearance of the EBs.	81
5.9	$H\alpha$ off-band images taken on 2001 July 15 at 20:43 UT. (a) Blue line wing filtergram at $H\alpha - 0.6 \text{ \AA}$, (b) red line wing filtergram at $H\alpha + 0.6 \text{ \AA}$, and (c) the corresponding $H\alpha$ dopplergram. The $H\alpha$ off-band filtergrams are shown with superimposed contour lines of a co-temporal magnetogram (Light gray: positive magnetic fields; Dark gray: negative fields; White: neutral line). The contour lines are drawn at the $\pm 300 \text{ G}$, $\pm 500 \text{ G}$ and $\pm 800 \text{ G}$ levels, respectively. The contour lines superimposed on top of the $H\alpha$ dopplergrams correspond to a divergence map derived from the average horizontal proper motions that are present in the time sequence of $H\alpha$ dopplergrams. The white box in each panel indicates the region of interest.	82
5.10	The twisting motion of the filament (F1) when it was falling down to the surface of the Sun is shown in these images. Notice the variation of the intensity of the Doppler signal from the filament.	83
5.11	Average horizontal velocity derived from a time sequence of speckle reconstructed continuum images. (a) Velocity field and (b) corresponding divergence map. The background image was taken at 20:32 UT.	84
5.12	Average horizontal velocity derived from a time sequence of $H\alpha + 0.6 \text{ \AA}$ line wing filtergrams. (a) Velocity field and (b) corresponding divergence map. The background filtergram was taken at 20:43 UT.	85
6.1	Distribution of the filament disappearances as the function of the distance from the center of the Sun.	92
6.2	A prominence eruption observed at BBSO at 22:10UT, on April 15, 2001. The field of view is $300''$ by $300''$ This eruption did not have an obviously related CME.	94

LIST OF FIGURES
(Continued)

Figure	Page
7.1 Running difference images of the March 20 CME. It shows that the CME was coming out the occult disk of C2 coronagraph at around 07:54 UT. At the beginning its speed was very low. The arrow in panel (a) indicates the arcade of loops of the CME. It is very clear from these images that this CME did not have the three-part structure that typical CMEs have. Also the images clear show that the CME consisted of three groups of loops that move in different directions.	98
7.2 Enhanced LASCO C2 images of the very bright region of the March 20, 2000 CME. The image enhancement was done by application of a high-pass filter. The detailed delicate structures of the CME are revealed. In the image of 08:30:05 UT, the helical lines are clearly demonstrated.	100
7.3 The upper panel shows the height vs. time plot of the upper group of loops near the equator of the Sun. R_s denotes the radius of the Sun. A loop that is easily tracked was chosen to derive the height-time plot. The lower panel shows the speed of the loop which is calculated using relation $v[i] = (h[i + 1] - h[i]) / (t[i + 1] - t[i])$. This group of loops came out of the occulting disk of the C2 coronagraph after the filament eruption and the flare. Their speed achieved several hundreds kilometer per second right after they appeared in the C2 images. Most of the measured speeds are below 1000 km s^{-1} and there is no obvious acceleration with the rising of the loops.	102
7.4 The upper panel shows the height vs. time plot of the middle group of loops. The lower panel shows the corresponding speed of the loops. This group of loops were the earliest coming out of the C2 occult disk. They were blocked in C3 images. From this figure, it can be seen that the CME expanding very slowly before the filament eruption. It got accelerated greatly after the filament eruption and the flare. The method to calculate the speed is described in Figure 7.3.	103
7.5 The upper panel shows the height vs. time plot of the group of loops in the far south of east limb. The lower panel shows the corresponding speed of the loops. This group of loops appeared in the C2 images after the filament eruption and the flare.	104
7.6 Sequences of EIT 195 Å images observed on March 20, 2000. In Frame (b), the upper and the lower arrows indicate two loops that expand afterwards. The arrow in the middle indicates the bright region prior to the CME. In Frame (c) and (d), the arrows indicate the location where the loops expand and open. The arrow In Frame (f) indicates the materials that probably came from the filament.	105

LIST OF FIGURES
(Continued)

Figure	Page
7.7 Running difference images of EIT. The EIT dimming regions can be seen above or near the filament.	107
7.8 EIT 195 Å images are overlaid with MDI magnetogram contour lines. The MDI image was taken at 08:15:02 UT. In the left panel, the EIT image was taken at 08:12:10 UT. This image shows that the filament resided over a neutral line in the active region. The EIT image in the right panel was taken at 08:36:10 UT. An edge enhance filter was applied to this image to make loop structure of the erupted filament visible. In both panels the solar rotation of the MDI image was adjusted accordingly.	108
7.9 LASCO C2 images are overlaid with EIT 195 Å images. In the left panel, the LASCO image was 6 minutes earlier than the EIT image. In the right panel, the LASCO image was 18 minutes later than the EIT image. From this figure, it can be seen that the bright region that appeared in the LASCO C2 image might correspond to the filament.	110

CHAPTER 1

INTRODUCTION

The Sun is the nearest star to the Earth and the most important astronomical object to all life on the Earth. The Sun is the primary energy source of the Earth. The energy from the Sun provides a temperature range that accommodates life. This energy sustains, through photosynthesis, most of the life on the Earth. The energy of the Sun deposited into the Earth's atmosphere also drives the global weather patterns which influence living organisms profoundly. Without the solar ultraviolet (UV) radiative inputs, there would not be an ozone layer in the Earth's middle atmosphere and organic life forms would be exposed to damaging high-energy radiations from the space.

1.1 The Need to Monitor and Study Space Weather

The Sun is a variable star. The sunspot number, the total radiative output and the entire solar spectrum exhibit a pronounced 11-year cycle. Various activities on the surface and in the upper atmosphere of the Sun have great impact on the interplanetary medium of the outer space near the Earth environment. Space weather refers to conditions on the Sun and in the solar wind, magnetosphere, ionosphere, and thermosphere that can influence the performance and reliability of space-borne and ground-based technological systems and can endanger human life or health. Adverse conditions in the space environment can cause disruption of satellite operations, communications, navigation, and electric power distribution grids, leading to a variety of socioeconomic losses. Changes in space weather have various adverse effects on life and technological systems both on the Earth and in space. High levels of solar activity threaten the safety of spacecrafts and astronauts; interrupt radio communication; cause problems such as interior and surface charges, computer and memory upsets and failures, damage to solar cells, and increase of atmospheric drag in Low

Earth Orbit (LEO) for satellites; and endanger aircraft personnel on polar routed flights by accumulated high energy radiation. Large-scale electric currents caused by geomagnetic storms can also damage power grids and trans-continental pipelines. Figure 1.1 shows the solar wind and magnetic storms approaching the Earth. The image was taken and made by Solar and Heliospheric Observatory (SOHO). For these reasons, monitoring, studying, understanding and predicting the Sun's irradiance variability and space weather is essential for all human beings.

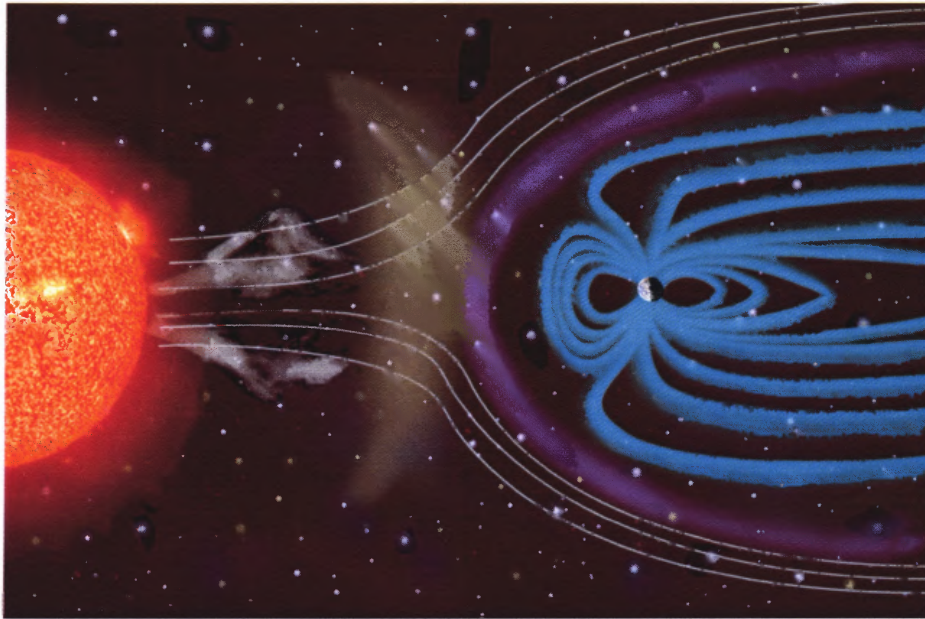


Figure 1.1 The Sun's magnetic field and releases of plasma directly affect the space weather very much. Space weather can effect the near Earth environment, e. g., astronaut safety, interior and surface charging of satellites, computer and memory upsets and failures on satellites, damage to solar cells, an increased atmospheric drag in Low Earth Orbit (LEO), an increase of airline passenger radiation on polar routes, disturbances of radio wave communication, disruptions in telecommunication cables, interruptions in power distribution systems, and induction of earth currents corroding pipelines. In this figure, solar wind shapes the Earth's magnetosphere and magnetic storms are illustrated as approaching the Earth.

1.2 Overview of Relevant Solar Characteristics and Activities

The close distance between the Sun and the Earth makes it possible to observe and follow solar fine structures and study the physics underlying all processes. Table 1.1 lists the basic physical parameters of the Sun. The Earth's orbit is not a circle. At the perihelion and the aphelion, $1''$, which is often used by solar physicists as length unit for solar fine structure, corresponds to 710 and 734 km respectively at the center of the solar disk. The angular radius of the Sun is about $960''$ at the mean solar distance.

The solar atmosphere is divided into three layers: photosphere, chromosphere, transition region and corona. The photosphere is a layer of about one hundred kilometers. There the solar atmosphere changes from almost completely opaque to completely transparent. The temperature of the photosphere is about 6000 K. The chromosphere derives its name from the colorful appearance observed during a solar eclipse. The corona can be seen by human eye during a total solar eclipse or at other times with dedicated instruments such as coronagraphs. The corona is a tenuous layer that extends to the planets and beyond. The chromosphere and corona are connected by a very thin layer in which the temperature rises radically from about 10^4 K to about 10^6 K and hence named as transition region.

Magnetic fields on the Sun play a vital role in almost all kinds of solar phenomena – almost all solar activity is an immediate consequence of the existence of magnetic fields. Observations of the solar surface have indicated that the magnetic flux in the solar atmosphere is confined to relatively small magnetic patches or ‘elements’ of high-field strength

Table 1.1 The Sun's Basic Physical Characteristics

Radius	$R = 6.960 \times 10^8$ m
Volume	$V = 1.412 \times 10^{27}$ m ³
Mass	$M = 1.991 \times 10^{30}$ kg
Mean Density	$\rho = 1.408$ g/cm ³
Gravity at surface	$g = 274$ m/s ²
Distance from the Earth	1 AU = 1.496×10^{11} m
Luminosity	$L = 3.844 \times 10^{26}$ W
Solar Constant	$S = 1367 \pm 3$ W/m ²

in the photosphere. These concentrations are surrounded by plasma of much weaker magnetic field.

The properties of these elements mainly depend on the total magnetic flux in them. According to different characteristics of the elements the magnetic structures form a hierarchy. Zwaan (1987) reviewed the hierarchy of the solar magnetic structures, which range in size from large to small, such as sunspots, pores, magnetic knots to faculae and network clusters, and individual flux fibers. The field strength of these structures are in the range from 1500 ~ 3000 Gauss. Table 1.2 (Located at the end of this chapter.) shows the hierarchy of the solar magnetic elements.

Sunspots are the largest compact magnetic concentrations on the surface of the Sun. A sunspot consists of two distinct parts: a dark central umbra and a penumbra, which at least partly surrounds the umbra. The magnetic flux observed in sunspots varies from 5×10^{20} Mx to 3×10^{22} Mx. High resolution observations show fine structures inside sunspots, e. g., light-bridges, umbral dots, and dark nuclei in umbra, bright and dark filaments, penumbral grains in penumbra (see Sobotka et al. 1993, 1997, 1999a). The magnetic field of sunspots decreases gradually from the center of umbrae, of about 3000 G, to the outer part of penumbra, of about 800 G, and vanishes abruptly slightly outside the penumbra in the photosphere. Near the center of a sunspot, the magnetic field is almost vertical. The inclination of the magnetic field increases with the increasing radial distance from the center of sunspots and becomes nearly horizontal in the penumbrae. The magnetic field continues as a magnetic canopy (Giovanelli 1982; Solanki et al. 1992) in the chromosphere outside the photospheric boundaries of the penumbra. Study of fine structures in sunspots play a very important role in understanding the dynamics and physical nature of sunspots.

Pores are small umbrae without surrounding penumbrae. The magnetic flux of pores varies from 2.5×10^{19} to 2.5×10^{20} Mx. The magnetic field lines appear to be close to vertical near the center of pores. The magnetic field of pores is over 2000 G. Some pores are identified as an early stage of sunspot evolution. Studying the evolution of

pores can lead to a better understanding of the interaction between magnetic fields and the surrounding convective motion.

One of the major breakthroughs in solar physics during the last 40 years has been the discovery that most photospheric magnetic flux outside of sunspots is in the form of small scale flux concentrations with field strengths of typically 1000 to 2000 G. Evolving from this discovery is the picture of small flux tubes with typical sizes of a few tens to a few 100 kilometers, as building blocks of plage and network magnetic fields. Sophisticated magneto-hydrodynamic (MHD) models now offer a variety of predictions that need to be tested. Also, precise measurements are necessary in order to define boundary conditions for these models.

The generation and dissipation of small-scale quiet solar magnetic features is responsible for the dynamics above the photosphere. Observation of small-scale magnetic fields, with the highest resolution, is crucial to understand small scale transition region and coronal brightenings, such as microflares and mini-filament eruptions. In active regions, magnetic fields also have small-scale magnetic structures that can be seen in high-resolution observations, such as moving magnetic features and small-scale bipoles. Complicated magnetic configurations would be likely to produce both large and small-scale activity. Obviously, finding the link between the evolution of magnetic fields and flares, filament eruptions, and Coronal Mass Ejections (CMEs) is one of the important tasks in solar physics.

Solar active regions are areas of high magnetic field strength on the surface of the Sun. The characteristics of active regions change over their lifetimes. In their period of maximum development, large active regions comprise sunspots, pores, plages, and enhanced network. The lifetime, size, and magnetic flux of active regions vary in a very large range at their maximum development.

Prominences are bright features above the solar limb when observed in strong chromospheric spectral lines. Prominences contain relative dense and cool ($5000 \lesssim T \lesssim$

8000 K) plasma. A prominence, when seen as a dark feature when observed against the solar disk, is called filament. All filaments reside over neutral lines – regions lying between two opposite magnetic polarities. Filaments or prominences can be seen in both active regions or quiet Sun. The size and shape of filaments vary greatly according to the underlying magnetic topology. Filaments may disappear suddenly when they erupt. Some studies show that filament eruptions may be associated with CMEs but the underlying physical process is still not clear.

Solar flares are the manifestation of a sudden, intense, and spatially concentrated rapid release of energy at the surface of the Sun. A solar flare occurs when magnetic energy that has built up in the solar atmosphere is suddenly released. Typically 10^{20} Js of energy is released during a flare every second. Large flares can release up to 10^{25} Js of energy. Radiation is emitted across virtually the entire electromagnetic spectrum, from radio waves at the long wavelength end, through optical emission to X-rays and gamma rays at the short wavelength end. Most flare models are somehow related to the theory of magnetic reconnection.

Coronal Mass Ejections (CMEs) were first observed in the early 1970s and since then have been studied intensively (Gosling et al. 1974, 1991; Howard et al. 1985; Illing & Hundhausen 1983; Hundhausen 1999). Each individual CME can carry away a mass of up to 10^{13} kg of plasma and release as much as 10^{25} J of magnetic energy (Gosling et al. 1974). With the observations of coronagraphs, a CME is identified by a discrete electron density enhancement expanding outward from the Sun. These structures generally have spatial scales of the order of the solar radius R_{\odot} or even much larger.

The CMEs play a very important role in the plasma coupling of the Sun and the Earth. A strong statistical correlation between CMEs and large geomagnetic storms has been confirmed by Gosling et al. (1991); Kahler (1992). There is also a strong statistical correlation between CMEs and interplanetary magnetic clouds (Wilson & Hildner 1984). Burlaga et al. (1981) first identified magnetic clouds and interpreted them as magnetic flux

ropes (Burlaga 1988). Several recent halo CMEs (when the CME is located near the center of the solar disk center) observed by the Large Angle and Spectrometric Coronagraph (LASCO) on board the Solar and Heliospheric Observatory (SoHO) were followed by magnetic clouds impinging on the Earth's magnetosphere observed by the *WIND* spacecraft at 1 AU, causing geomagnetic storms (Brueckner et al. 1998).

Although Earth-directed or halo CMEs have the most important geomagnetic effects, they are much harder to detect than those that occur near the solar limb where they appear against a dark background. Detecting the early manifestation of CMEs on the solar disk is essential to understanding Earth-directed CMEs. The connection of CMEs with solar surface phenomena, such as filament eruptions and flares has been a long-standing problem in solar physics. If firm relationships can be established between the correlated solar surface phenomena and Earth-directed CMEs, some early warnings can be provided well before harmful geomagnetic effects are induced.

1.3 Seeing Problem and The Need to Process Images in Real Time

In order to study the Sun, high quality observational data from both ground and space based observatories are needed to understand the basic physics processes of the solar activity. The primary data source used in this dissertation is Big Bear Solar Observatory (BBSO). Due to its unique weather conditions and geographical location, BBSO is an ideal site for daytime solar observations. BBSO is located 2,100 m high in Big Bear Lake in the mountains of southern California. The number of clear days exceeds 300 each year. Atmospheric turbulence ("seeing") is the primary factor restricting the angular resolution of ground based telescopes. The atmospheric turbulence that degrades images ("poor-seeing") comes primarily from two atmospheric layers – near the ground and at the level of the jet stream. BBSO is an ideal site for ground-based campaign-style observations because of its excellent "seeing" conditions all day long. The Big Bear Valley where Big Bear Lake resides orients east-west acting as a wind channel. The ground seeing problem is largely minimized

(Goode et al. 2000) due to the prevailing winds from the west, and the wind reaches the observatory building in a nearly laminar flow. Since the observatory is relatively close to the ocean, turbulence from the jet stream layer is reduced because the jet stream is calmest over the oceans. Further more, BBSO's observatory building is located at the end of a 300 m long causeway jutting into the lake. The lake, with its cool water, provides a natural inversion, and the dome has several kilometers of open water to its west. Figure 1.2 shows a picture of BBSO.

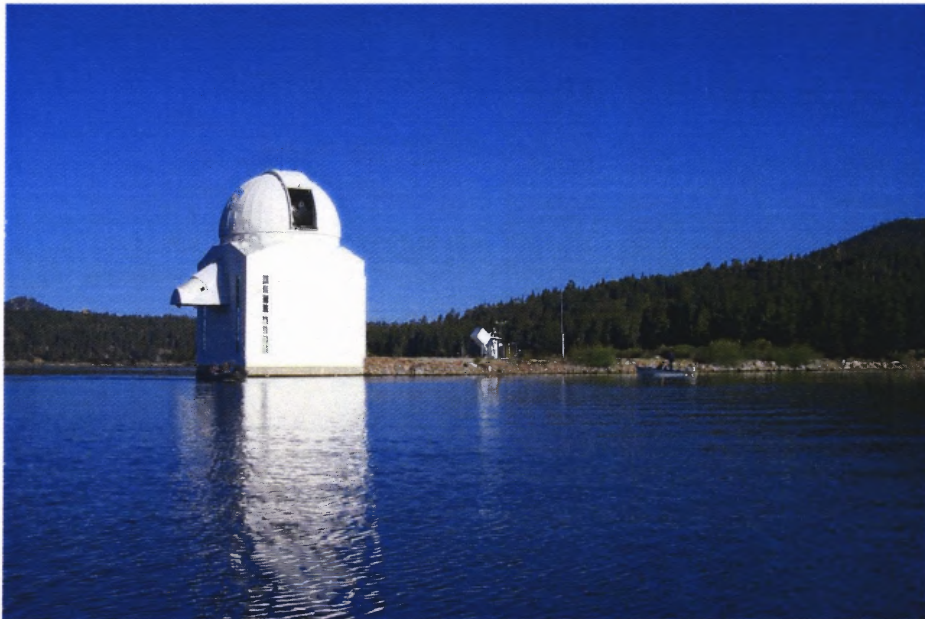


Figure 1.2 Big Bear Solar Observatory (BBSO) is located in a high mountain lake in the southern California. The unique weather condition and geographical location make BBSO an ideal site for daytime solar observations.

The BBSO's telescopes are specially designed for solar observations. The top floor of the observatory contains a single fork mount supporting the five main telescopes: a 65 cm vacuum reflector, a 25 cm vacuum refractor, a 20 cm refractor for $H\alpha$ full disk observations, a 15 cm photometric full disk telescope for $Ca II K$ and continuum observations, and a 15 cm refractor for earthshine observations. The telescopes are equipped with highly specialized filters and cameras that isolate small portions of the visible, as well as the near infrared and ultraviolet portions, of the Sun's spectrum.

Even though the BBSO site was selected very carefully to avoid serious seeing problem (Zirin & Mosher 1988), the Earth's atmospheric turbulence still imposes a serious limitation to solar imaging. An important goal in ground-based astronomy is to improve the angular resolution that can be achieved by modern large-aperture telescopes. Due to atmospheric turbulence, the refractive index of the Earth's atmosphere is nonuniform, which results in aberrations of the wavefront of light waves traveling through the atmosphere. Because of the atmospheric turbulence, the resolution of the ground-based telescope is limited to about $0.5''$ for short exposure images ($\lesssim 20$ ms) and to about $1''$ for long exposure (≈ 1 s) images in visible wavelength (e.g., around 5500 \AA) regardless the aperture size of the telescope. For a comparison, the theoretically achievable resolution for a 4-meter telescope (e.g. ATST, Advanced Technology Solar Telescope) would be about $0.013''$. For solar observations, the situation is made worse by heating of the ground, which in turn will cause increased turbulence near the ground that will greatly deteriorate seeing conditions. However, many basic processes on the Sun take place at scales below $1.0''$. The photon mean free path in the lower photosphere corresponds to about $0.1''$ at disk center. Magnetic elements outside sunspots have typical diameters smaller than $0.2''$ (Keller 1995). Magnetic structures may occur on even smaller scales. Despite their small size, these small structures are believed to play an important role in large-scale phenomena such as the solar magnetic dynamo or the triggering of solar flares and CMEs. To understand a variety of solar phenomena, it is, therefore, indispensable to reach a spatial resolution well below the seeing limit and possibly approaching the diffraction limit of existing and future large ground-based solar telescopes. Also in order to predict space weather, it is required to monitor solar's active regions continuously.

A number of sophisticated techniques have been conceived to combat the deleterious effects of atmospheric turbulence in astronomical imaging in general. Among these are speckle imaging (Labeyrie 1970) as a post detection computer processing method and adaptive optics (Babcock 1953) as a pre-detection method. Speckle imaging involves processing

a large set of short exposure, speckled images. In speckle imaging, the object is estimated generally first by estimating its Fourier transform, and then inverting the Fourier data to obtain an estimate of the object. Adaptive optics is a pre-detection method to mitigate the deleterious atmospheric turbulence effects. Adaptive optics provides a means of sensing the atmospheric turbulence-induced aberration and partially correcting for this aberration in real-time. The image quality is improved, both in spatial resolution and photometric accuracy, by reducing the aberration caused by the atmosphere.

Both methods have limitations. Speckle imaging is limited to broadband applications ($> 3\text{\AA}$). The degree of randomness in the atmospheric turbulence-imposed transfer function and the statistics associated with photoelectric detection of light also result in a low signal-to-noise ratio (SNR). Speckle imaging is also too computationally intensive to get the real-time images that are required for monitoring and prediction of space weather. The adaptive optics approach, in turn, is limited by the finite spatial sampling of the wave front by the wave front sensor, the finite number of degrees-of-freedom in the deformable mirror, finite signal levels available to the wave front sensor, and time delays between sensing and correcting the turbulence-induced aberration. Also the complexity and the expense of adaptive optics for a large telescope further restrict its application.

Speckle imaging applies complex numerical algorithms for data analysis. Historically, only a few data sets have been analyzed per year, and only at the end of this process does one discover whether something really interesting has been captured. This is due to the long computation time. So without a real-time imaging processing system, raw images have to be saved and processed off-line, and a hard disk is filled up very quickly. The time-lag between the observation and the data analysis has been far too long for any sort of rapid response, such as would be needed for space weather warnings and flare forecasting. Furthermore, the time lag renders the whole scientific enterprise less efficient than it needs to be considering today's computer technologies.

The power of parallel computing has just started to be exploited in solar physics.

Supercomputers located at a few national centers have been used for numerical calculations in astrophysics, however they cannot be used for real-time data processing because the observational data cannot be transferred to the supercomputer centers in real-time. With the development of network technology and cluster computing, parallel processing of solar data will literally provide a new window through which the solar physicists can observe the Sun in exquisite detail and study the evolution of granulation and sunspots in the active regions leading to major flares.

1.4 The Goal of This Study

The goal of this study is to explore the application of parallel computing to the speckle masking method and get high spatial resolution and high temporal resolution solar images. A system was built that can monitor solar active regions and using the speckle masking method, a variation of speckle interferometry, to obtain near diffraction limited images in real-time. Using these high quality images, the evolution of a pore and the development of a penumbral structure are studied in detail. A statistical study of filament disappearances and their association with CMEs was also conducted. Finally, as a case study, a highly helical CME has been studied. The morphological and kinetic properties of the CME were explored.

In Chapter 2, an introduction of data processing methods is presented that will be used in the subsequent chapters. In Chapter 3, an implementation of the speckle masking method using a parallel computer is described. Using the real-time data, a detailed study of a pore is presented in Chapter 4. The data are further explored to study the development of a penumbral structure around the pore in Chapter 5. In Chapter 6, a statistical study of filament disappearance and its association with CMEs is presented. Morphological and kinetic properties of a highly helical CME will be described in Chapter 7.

Table 1.2 The Hierarchy of Solar Magnetic Structures

Property	Sunspots with Penumbra		Pore	Magnetic Knot (micropore)	Faculae Network Clusters	Flux Fibre
	large	small				
Φ ($10^{18}\text{Mx} = 10^{10}\text{Wb}$)	3×10^4	500	250 – 25	≈ 10	$\lesssim 20$	≈ 0.5
R (Mm)	28	4	–	–	–	–
R_u (Mm)	11.5	2.0	1.8 – 0.7	≈ 0.5	–	≈ 0.1
B (1 G = 10^{-4} T)	2900 ± 400	2400 ± 200	2200 ± 200	$\approx 1500 - 2000$	–	≈ 1500
Overall contrast in continuum:	<i>dark</i>			–	<i>bright</i>	
Cohesion:	<i>single, compact structure</i>				<i>Cluster of flux fibers</i>	
Behavior in time	<i>remain sharp while shrinking during decay</i>			?	–	<i>modulated by granulation</i>
Occurrence:	<i>exclusively in active regions</i>				<i>both inside and outside active regions</i>	

Note. — Φ is the magnetic flux, R is the radius of a sunspot, R_u is the radius of a sunspot umbra of a smaller magnetic concentration, and B is the magnetic field strength at its center.

CHAPTER 2

IMAGE PROCESSING

Image processing is a very important part of solar physics. One of the purposes of image processing in solar physics is to correct the deteriorations of the images caused by the turbulent atmosphere of the Earth and optical systems. Due to imperfection of optical system and atmospheric seeing, all the images must be processed before they are used to study phenomena on the Sun.

In the following sections, various methods are described that are used to correct and enhance images. The image processing steps are described in the order that they are used in data analysis.

2.1 Preprocessing

2.1.1 Dark Current Frames

Conceived in the 1960s by AT&T (Boyle & Smith 1993), Charge-Coupled Devices (CCDs) have become the most commonly used detectors in astronomical imaging. A CCD consists of an array of metal-oxide-semiconductor (MOS) capacitors which can accumulate and store charges. When a CCD is exposed to incident light, charges are generated and accumulated in the grid of capacitors of the CCD due to the internal photoelectric effect of the semiconductor. The charges are then collected and transformed into a proportional voltage which is subsequently read out. The fast CCD that is used in this study is a large-format CCD (1024×1024) with low noise (e.g., the rms level is about 1.5 DN) and high speed (e.g., 15 fps).

Dark currents are unwanted signals generated by CCDs in addition to the signal generated by incoming light. They are caused mainly by imperfections and quantum-mechanical effects of CCD materials. The dark current is temperature dependent and ap-

appears as an addition to the readout noise. The dark current can be removed by subtracting dark current frames that are taken while blocking the CCD from incident light, using the same exposure time as the scientific observations.

2.1.2 Flat Field Frames

The response of CCD detectors is linear in most of the dynamic range, i.e, the ratio of the CCD's saturation level to its signal threshold. Pixel-to-pixel gain variations, even though they are small, have to be taken into account in high resolution photometry. They can be observed by directing a homogeneous parallel bundle of light onto the CCD. The optical system defects such as vignetting and dust can also cause some pixel-to-pixel variations. The pixel-to-pixel variations can be accounted for by dividing dark current corrected images with a flat field image.

There are several methods to derive flat field images in solar observations. One common way to obtain flat field images is to point the telescope to the center of the solar disk avoiding active regions. Then the CCD is exposed to defocused light and several solar images are taken using the same exposure time and filter settings as for the scientific observation. The defocused images are averaged to compute the flat field image. At BBSO, the method first proposed by Kuhn et al. (1991) is usually used. This method uses multiple spatially displaced images to obtain the pixel gain to within a spatially constant factor. In speckle masking observations, flat field images are obtained by moving the telescope fast in both the declination and right ascension axis while pointing and focusing at solar disk center. In the averaged flat field frame, the solar features will be washed out due to the fact solar granulation is an isotropic feature. Figure 2.1 shows an example of applying dark frame and flat field correction to raw images. Figure 2.2 shows the same corrections applied to defocused data.

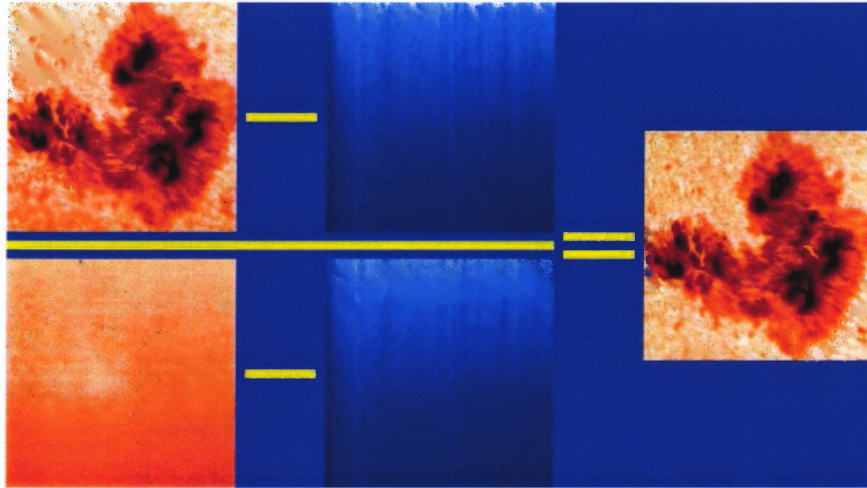


Figure 2.1 Schematic representation of the dark and flat field image calibration procedure. The image gradient visible in the raw data and the artifacts due to dust particles on the CCD chip have been removed. Note that the image panels were scaled individually, thus, contrasts are not directly comparable.

2.2 Image Motion and Differential Image Motion

Many factors, e.g. atmospheric turbulence, wind-shaking of the telescope and the pointing drift of the telescope, cause image motion in a time series of images. This motion must be removed in order to perform the speckle masking reconstruction and/or make movies to study the evolution of fine structures on the solar surface. Images are usually aligned with the image that has the highest root mean square (rms) contrast value. The alignment is done by locating the maximum of the cross-correlation function. In the future, this step in the data reduction could be saved by use of a correlation tracker which compensates image motion at a rate of up to 2000 Hz.

Since speckle interferometry is only valid for a small region – the size of an isoplanatic patch – the interferograms have to be divided into mosaics of partially overlapping images (von der Luehe 1993). In this study, each isoplanatic patch has a size of approximately $6'' \times 6''$, which corresponds to 64×64 pixels. The differential image displacement in these stacks of sub-images is also removed. Just as for the overall image motion, differential image displacement is also computed by locating the maximum of the cross-

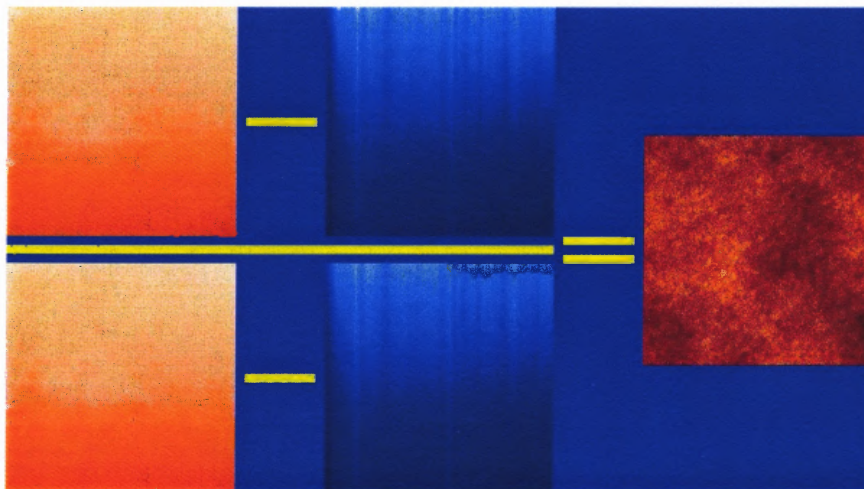


Figure 2.2 Same schematic as in Figure 2.1, however, here the dark and flat filed calibration procedures were applied to defocused raw images. These data are used in the signal-to-noise estimation process and as one can see only some large scale features and salt-and-pepper noise is left in the images. The image panels were scaled individually, thus, contrasts are not directly comparable.

correlation function in sub-images. To avoid leakage and aliasing effects, all images and isoplanatic patches were multiplied by an apodisation window. The apodisation window for the 64×64 pixel isoplanatic patches is a modified Hanning window (Figure 2.3) with a cosine square roll-off across 9 pixels and a central plateau of unity.

2.3 Speckle Masking Method

Speckle interferometry has become an important tool in astronomy to overcome image degradation due to the Earth's atmospheric turbulence. The original method was introduced by Labeyrie (1970) but it can only give corrected power spectra of objects. In order to obtain all image information, phases of the Fourier transforms have to be known in addition to the Fourier amplitudes. Further developments, e.g., the Knox-Thompson algorithm (Knox & Thompson 1974), give real diffraction-limited images of extended objects such as small scale structures on the solar surface (Stachnik et al. 1977; von der Luehe 1993) by recovering both phase and amplitude information from the interferograms. A qualitative improvement in solar speckle interferometry was the introduction of the speckle masking

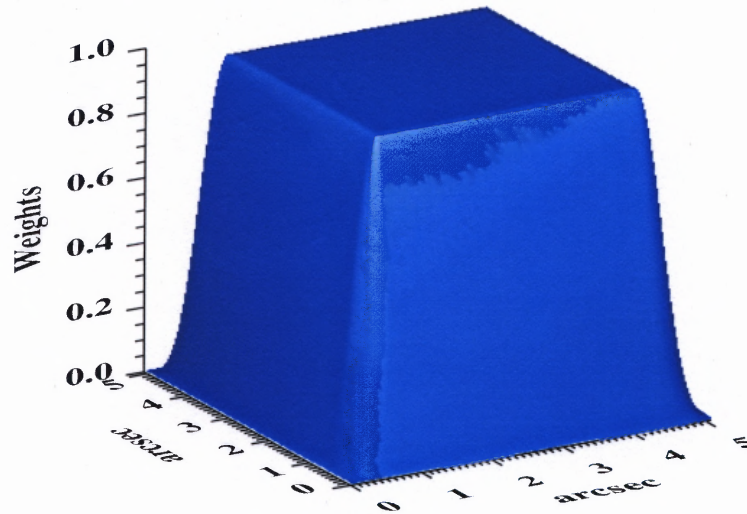


Figure 2.3 Modified Hanning function as apodisation window for isoplanatic patches.

method or triple correlation technique (Weigelt 1977; Weigelt & Wirmitzer 1983; Lohmann et al. 1983). It is a better choice in the study of solar fine structures for several reasons (see Pehlemann & von der Luehe 1989):

1. The signal-to-noise ratio of the reconstruction for an extended object such as small scale structures on the solar surface is increased due to the high redundancy of phase information inherent in speckle masking method. This is especially important to solar observations because of the low contrast of solar small scale features.
2. The high redundancy of phase information makes it possible to apply a very efficient noise filter, which is very important to the reconstruction (e.g., de Boer 1996).
3. For solar observations, the number of input images for reconstruction is limited to a couple of hundred because of the proper motion and evolution of solar fine structures. This makes the high signal-to-noise ratio even more important.

The speckle masking method requires a sequence of short-exposure images (less than 10 ms) to “freeze” the wavefront aberrations, which makes it possible to separate the object information from the information about atmospheric turbulence. Analyzing com-

plex objects, such as sunspots or pores, requires calculating the modulus and phase of their Fourier transform at the same time. The spectral ratio technique is used to derive the Fried-parameter r_0 (von der Luehe 1984). Roughly, the Fried parameter corresponds to the aperture of the largest telescope that would be diffraction limited at that location. The observed spectral ratios have been compared with the theoretical values derived from Fried's model (Fried 1966) and Korff's model (Korff 1973) of the average short-exposure modulation transfer function (MTF). The amplitudes of the object's Fourier transform are then corrected according to the classical method of Labeyrie (1970), since this is more reliable than the amplitude recovery by means of the bi-spectrum (see 2.3.2 for a detailed description). A more complete bibliography on solar speckle interferometry is given by Denker (1998) and recent results from speckle masking imaging at BBSO are given by Denker & Wang (1998) and Yang et al. (2003). In the following subsections the speckle masking method is described in more detail. Note that the description is applied to the 64×64 sub-images mentioned above.

2.3.1 Speckle Interferometry

The intensity distribution in the focal plane of a telescope $i(\vec{x})$ is given by the convolution of the intensity distribution of the object $o(\vec{x})$ and the instantaneous point spread function (PSF) $h(\vec{x})$ which describes the combined system of the atmospheric turbulence along the line-of-sight and the telescope

$$i(\vec{x}) = o(\vec{x}) \otimes h(\vec{x}), \quad (2.1)$$

where \vec{x} denotes a two-dimensional spatial coordinate and \otimes stands for the convolution operator.

Fourier transformation yields

$$I(\vec{q}) = O(\vec{q})H(\vec{q}), \quad (2.2)$$

where $I(\vec{q})$, $O(\vec{q})$, and $H(\vec{q})$ are the Fourier transformed complex quantities of Equation (1), and \vec{q} is a two-dimensional, normalized spatial frequency. $H(\vec{q})$ is the optical transfer function (OTF).

According to Fried (1966), the mean OTF is nearly zero for high spatial frequencies for $D \gg r_0$, where D is the aperture of the telescope and r_0 is the Fried seeing parameter. Thus high spatial frequency information of the object cannot pass through the atmosphere-telescope system to the imaging devices. This severely limits the resolution of conventional imaging through atmospheric turbulence.

Labeyrie (1970) noticed that the speckle pattern presented in short exposure images might contain more information on smaller features than long exposure images. He proposed speckle interferometry to recover the object power spectra from a series of short exposure images. Korff (1973) shows that the second moment of the short-exposure modulus of OTF, i.e., $|H(\vec{q})|^2$, the so called modulation transfer function (MTF), is finite out to the diffraction limited cutoff frequency of the telescope. Therefore, if $|O(\vec{q})|^2$ is greater than zero for frequencies approaching the cutoff frequency of the telescope, the power spectra of the image will contain diffraction-limited information about the object. Although the instantaneous MTF is unknown, the ensemble average of the MTF can be determined either by using a reference star or by theoretical study with the knowledge of the optical system

$$\begin{aligned} \langle |I(\vec{q})|^2 \rangle &= \langle |O(\vec{q})H(\vec{q})|^2 \rangle \\ &= |O(\vec{q})|^2 \langle |H(\vec{q})|^2 \rangle, \end{aligned} \quad (2.3)$$

where $\langle \rangle$ denotes an ensemble average. $\langle |H(\vec{q})|^2 \rangle$ is called speckle transfer function (STF). If the STF is known, the modulus of the Fourier transformed reconstruction $O(\vec{q})$ can be calculated:

$$|O(\vec{q})|^2 = \frac{\langle |I(\vec{q})|^2 \rangle}{\langle |H(\vec{q})|^2 \rangle}. \quad (2.4)$$

Spectral Ratio Technique

In stellar observations, the STF can be estimated by observing an unresolved reference star. But solar observations are more complex because the particular shape of certain structures is inherently unknown when observed through turbulence (von der Luehe 1984). There are no reference stars on the Sun to recalibrate the power spectra. In order to apply speckle interferometry to solar observations, one has to derive the transfer function indirectly. This can be done by using theoretical models of the statistical properties of the combined atmospheric and telescope's STF. Exhaustive and widely accepted research indicates that the STF is entirely determined by a single parameter r_0 , the Fried Parameter (Fried 1966). Thus, if r_0 is known, it can be inserted into an appropriate model and the STF can be calculated.

In this study, the spectral ratio technique is used to derive the Fried-parameter r_0 (von der Luehe 1984). The spectral ratio is given by

$$\varepsilon(\vec{q}) = \frac{|\langle I(\vec{q}) \rangle|^2}{\langle |I(\vec{q})| \rangle^2} = \frac{|\langle O(\vec{q}) \rangle|^2 |\langle H(\vec{q}) \rangle|^2}{\langle |O(\vec{q})| \rangle^2 \langle |H(\vec{q})| \rangle^2} = \frac{|\langle H(\vec{q}) \rangle|^2}{\langle |H(\vec{q})| \rangle^2}, \quad (2.5)$$

$\langle H(\vec{q}) \rangle$ tends quickly toward zero for q larger than the atmospheric cutoff, whereas $\langle |H(\vec{q})|^2 \rangle$ is finite up to the telescope's diffraction limited cutoff frequency. The atmospheric cutoff frequency is related to the seeing conditions, hence the Fried parameter can be derived from the spectral ratio.

Noise Treatment

Noise has to be removed in order to obtain a reliable and accurate estimate of the object's mean power spectrum. The main source of noise is photon noise. The physical origin of photon noise is the quantized, random nature of photon-matter interactions. Photon-matter interactions which occur in light detectors are fundamentally random and obey Poisson statistics. Thus it is different from the dark current that is mentioned before and cannot be

removed by simply subtracting a dark frame.

Following Goodman (1985), the photon noise contribution to the Fourier transform of an image can be modeled as an additive, circularly Gaussian random process with zero mean. The Fourier transform of the image can be written as

$$I(\vec{q}) = O(\vec{q})H(\vec{q}) + N(\vec{q}), \quad (2.6)$$

where $I(\vec{q})$, $O(\vec{q})$, and $H(\vec{q})$ have the same meaning as before, $N(\vec{q})$ denotes Fourier transform of the photon noise. Following von der Luehe (1993), two conditions are assumed for the statistics of $N(\vec{q})$:

$$\langle N(\vec{q}) \rangle = 0 \quad (2.7)$$

$$\langle H(\vec{q})N(\vec{q}) \rangle = 0. \quad (2.8)$$

Under these assumptions, the ensemble average power spectrum of the images can then be expressed with

$$\langle |I(\vec{q})|^2 \rangle = |O(\vec{q})|^2 \langle |H(\vec{q})|^2 \rangle + \langle |N(\vec{q})|^2 \rangle. \quad (2.9)$$

This means that the ensemble average power spectrum of the image sequence contains a deterministic component whose expected value is equal to the variance of the noise. The ensemble average of the photon noise can be determined by taking defocused images of the same region of the Sun and using the same setup as for speckle imaging. The average power spectra of the defocused images is an accurate estimate of the photon noise which contaminate the mean power spectra of the speckle interferometric data.

2.3.2 Speckle Masking Bi-spectrum

To derive the phases of the object's Fourier transform, the speckle masking method was used. The bi-spectrum of an image is defined (Lohmann et al. 1983) as

$$I^3(\vec{q}, \vec{p}) = I(\vec{q})I(\vec{p})I^*(-\vec{q} - \vec{p}), \quad (2.10)$$

where $I(\vec{q})$, $I(\vec{p})$ and $I(\vec{q} + \vec{p})$ are identical Fourier transform of $i(\vec{x})$, expressed in different variables and the * denotes a conjugate complex quantity. In the speckle masking method, the ensemble average of the bi-spectrum $\langle I^3(\vec{q}, \vec{p}) \rangle$ is determined

$$\langle I^3(\vec{q}, \vec{p}) \rangle = B(\vec{q}, \vec{p}) = O^3(\vec{q}, \vec{p})\langle H^3(\vec{q}, \vec{p}) \rangle, \quad (2.11)$$

where $\langle H^3(\vec{q}, \vec{p}) \rangle$ is the averaged speckle masking transfer function (SMTF). The SMTF is real and nonzero up to the telescope cutoff frequency. This means that the phase of the complex bi-spectrum of the object is identical to the phase of the average bi-spectrum of the speckle interferograms.

For images that are digitized with $N \times N$ discrete, equally spaced pixels, the bi-spectrum can be expressed as

$$B(i, j, k, l) = \langle I(i, j)I(k, l)I(-i - k, -j - l) \rangle, \quad (2.12)$$

where i, j, k, l denote integer spatial frequency indices. For the principal spectrum, the indices i, j, k , should range between $-N/2$ and $+N/2 - 1$. The bi-spectrum is a four-dimensional array which contains all the information about the phase of the Fourier transformed reconstruction. The size of the bi-spectrum is very large. For an image of 64×64 pixels, the corresponding bi-spectrum will occupy about 128 Mbyte of random access memory (RAM). The size of bi-spectrum can be reduced by exploring its symmetric properties. However, most of the symmetric properties are very difficult to handle. Pehlemann

& von der Luehe (1989) proposed another method which relies on the truncation parameter to reduce the size of bi-spectrum. The truncation parameter M is used such that

$$|k|, |l| \leq M. \quad (2.13)$$

$M = 5$ was recommended by Pehlemann & von der Luehe for optimal choice, but larger value may yield better (but much slower) reconstructions.

The phase can be recovered by recursively using the phase closure relation (Lohmann et al. 1983)

$$e^{i\phi(i+k, j+l)} = e^{i\phi(i, j)} e^{i\phi(k, l)} e^{-i\Phi(i, j, k, l)}, \quad (2.14)$$

where ϕ is the phase of the finally reconstructed image, and Φ the bi-spectrum phase. Using a complex phasor can avoid the $\pm\pi$ ambiguities when phase values are averaged directly. Although $\phi(0, 0) = 0$ is known, it's not sufficient to start a recursive reconstruction. Additional starting points can be chosen

$$\begin{aligned} \phi(\pm 1, 0) &= 0 \\ \phi(0, \pm 1) &= 0. \end{aligned} \quad (2.15)$$

Nonzero value for these values can only add a shift of the image in the space and no information is lost by making the choice in the above equation. With these values and the bi-spectrum all remaining phasors of the object can be calculated using Equation 2.14.

During the reconstruction process, there are many possible combinations of i, j, k, l that will contribute to a given point in the Fourier space. Considering the spatial frequency index (m, n) with $m = i + k, n = j + l$, there are several possible combinations of i, j, k , and l that fulfill the truncation conditions and yield the same phasor value. These phasors are averaged directly without application of any weighting criteria. A phase consistency (PC) function (Pehlemann & von der Luehe 1989) can be defined using the number of these

multiple phasors

$$PC(m, n) = \left| \frac{1}{PN(m, n)} \sum_{\beta=1}^{PN(m, n)} e^{i\phi_{\beta}(m, n)} \right|, \quad (2.16)$$

where $PN(m, n)$ is the phase number function, which defines the number of phasors at spatial frequency (m, n) . As can be seen, PC will be 1 if all of the complex phases contributing to a specific combination of indices (m, n) are equal. It will be much smaller than 1 if the phases are so affected by noise as to be randomly distributed. So the phase consistency function can be regarded as a measure of the reliability at each individual phasor. Based on these observations, a sensitive noise filter is proposed by de Boer (1996). This noise filter is applied to the phase reconstruction process to improve the final result.

2.3.3 Reassembly of the Reconstructed Isoplanatic Patches

Once both the amplitude and the phase information of one isoplanatic patch are recovered, an inverse transform applied to them yields the final amplitude-corrected, reconstructed isoplanatic patch. This procedure is repeated until all the patches are recovered. Once all the isoplanatic patches are reconstructed, they are aligned carefully with the corresponding isoplanatic patches of the reference image by locating the maximum of their cross-correlation and shifting the restored isoplanatic patch. Before all the recovered and aligned isoplanatic patches are connected to form a final reconstructed image, edges of the patches are multiplied with \sin^2 square and \cos^2 functions of space points to reduce the edge effects.

2.4 Rigid Alignment and Destretching of Reconstructed Time Series

The motion of consecutive images caused by seeing and telescope pointing errors are computed and removed by rigid alignment, i.e., by locating the maximum of the cross correlation between each image and a reference image (usually the image in the time series with highest contrast) as described in Section 2.2. Although this process uses the same method as Section 2.2, it is applied to the consecutive images, while the process described

in Section 2.2 is applied to the interferograms which one image are reconstructed.

The residual distortion in the images caused by the effects of seeing is further removed by a method called destretching (Shine et al. 1994). This method is similar to the local correlation tracking method that will be described later in more detail in this chapter. A grid of points is chosen that will cover all images in a time series and divide each image into overlapping sub-images. A local correlation is calculated between each sub-image and the corresponding sub-image in the following image. The maximum locations of local correlation are derived for all the grid points and these yield offsets from the original grid points. These offsets have contributions from “seeing”, flows on the Sun, possible horizontal oscillations on the Sun, and probably some small systematic (accumulative) errors. The “seeing” component in these offsets is isolated by applying a temporal unsharp mask (i.e., subtracting a boxcar smoothed version of the signal from the original signal) with a mask width of ≈ 10 -15 minutes in time. What remains are all the high-frequency jitters from seeing induced distortions and any horizontal oscillations on the Sun. This jitter signal at each grid point is then linearly interpolated over each image to obtain a spatial offset for every pixel. They are collected into a table of control (tile) points and a B-spline surface is fitted to these tile points. Then each of the images in the time series is resampled on the non-uniform grid. Note that this technique does not use a specific reference image and that any systematic flows in the movies are preserved. Because it depends on correlating structures from image to image, it cannot reliably remove distortions on scales smaller than a few granules in size. Also, the images must be close enough together in time for the patterns to remain similar. For photospheric lines and continuum, images can be separated by a minute or two (Shine et al. 1994).

2.5 Subsonic Filter

The acoustic waves (p-modes) in the photosphere can cause intensity variations in a time series of images. This effect can be removed by means of a subsonic filter as proposed by

Title et al. (1989). In this method, a raw image sequence, which can be considered to be a single three-dimensional function of intensity (I_x, I_y) and time (t) , is Fourier transformed into a function of k_x, k_y , and ω . The subsonic filter is defined by a cone,

$$v_p = \frac{\omega}{k},$$

in (\vec{k}, ω) -space, where \vec{k} and ω are spatial and temporal frequencies, v_p is the maximum phase velocity and k is the modulus of \vec{k} and is equal to $\sqrt{k_x^2 + k_y^2}$. All Fourier components inside the cone (i.e., with phase velocities less than v_p) are retained, while all those outside are set to zero. Then a new sequence of images is calculated by an inverse Fourier transform. In order to remove the acoustic waves effect, values of v_p should be lower than the sound speed of 7 km s^{-1} . The value should be selected to filter out the fast oscillations caused by p-modes as well as fast image distortion due to differential seeing effects but conserve the real evolutionary components in the images (November & Simon 1988).

2.6 Local Correlation Tracking

Horizontal flow fields on the solar surface near pores and sunspots are measured using the local correlation tracking (LCT) method (November & Simon 1988). In this method, a coarse rectangular grid of points is chosen covering the time series of images. Following November & Simon (1988), a four-dimensional localized cross correlation $C(\vec{\delta}, \vec{x})$ is defined and computed in the neighborhood of each grid point

$$C(\vec{\delta}, \vec{x}) = \int i_t \left(\vec{\xi} - \frac{\vec{\delta}}{2} \right) i_{t+\tau} \left(\vec{\xi} + \frac{\vec{\delta}}{2} \right) W(\vec{x} - \vec{\xi}) \partial \vec{\xi}, \quad (2.17)$$

where $W(\vec{x})$ is a Gaussian apodizing window function, $\vec{\delta}$ is a two-dimensional displacement between images, \vec{x} is the two-dimensional central location of the grid point, $i_t(\vec{x})$ and $i_{t+\tau}(\vec{x})$ are the intensity of images at the times of t and $t + \tau$. Any large-scale intensity vari-

ations in the images must be removed before the local cross correlation is formed because a displacement bias will result from any such intensity gradient over the apodizing window. This can be achieved either by applying Fourier spatial filtering in the frequency domain or by convolution of the image with, e.g., the Laplacian of a Gaussian function, in the space domain. In order to reduce the residual seeing effect from the speckle masking reconstruction, the cross correlation is averaged in time before its maximum is located. At last the time averaged cross correlation, $\langle C(\vec{\delta}, \vec{x}) \rangle_t$ is interpolated in $\vec{\delta}$ to define the displacement vector, $\Delta(\vec{x})$, that locally maximizes the cross correlation at each grid point

$$\left. \frac{\partial \langle C(\vec{\delta}, \vec{x}) \rangle_t}{\partial \vec{\delta}} \right|_{\vec{\delta}=\Delta(\vec{x})} = 0. \quad (2.18)$$

These displacements can be interpreted as the horizontal velocities at the grid points. The full width at half-maximum (FWHM) of the Gaussian apodizing window defines the resolution of the velocity measurement.

CHAPTER 3

IMPLEMENTING THE REAL-TIME IMAGE RECONSTRUCTION SYSTEM

3.1 Introduction

Solar physicists have to deal with huge amounts of data. In order to study the evolution of solar surface fine structures, to monitor active regions on the Sun, and to predict the effects of solar activity on the space environment, high spatial, temporal, and spectral resolution data is ultimately required in solar physics. Consider a two-dimensional spectropolarimetric observation, where the image size is 1024×1024 pixel. For example, if the data sets are recorded by an imaging magnetograph, one would get a multi-dimensional data sets, including two spatial dimensions, wavelength, polarization state and time. A scan across the spectral line profile takes about 5 s for 20 wavelength points. The procedure is repeated six times to obtain the full Stokes vector, which results in about 960 Mbytes data for one line profile every 30 s assuming the data to be 16-bit. A two hour observation period will result in about 225 Gbytes data only for spectroscopic observation, not to mention data sets in other wavelengths, including $H\alpha$, white-light speckle masking data, etc., which are necessary for the aforementioned studies. Compare this with the Hubble Deep Field (HDF) observation (Williams et al. 1996), where exposure times vary from 900 to 3100 seconds. It yielded 3 Gbytes of data in its 10 days observation with 4 passbands. Even though HDF is an extreme example, the huge amount of data involved in solar physics presents a challenge for solar physicists.

As said in Chapter 1, Ground based large astronomical telescopes are always limited in spatial resolution by the Earth's atmospheric turbulence. For the special case of ground-base solar observations, the spatial resolution is typically limited to $1''$, whereas the scales of many basic processes on the Sun are well below $1''$. For example, magnetic elements outside of sunspots have typical diameters smaller than $0.2''$. However these small

structures are believed to play very a important role in solar large-scale phenomena such as heating the corona and as tracers of the solar magnetic dynamo. Therefore, it is ultimately important for solar observations to overcome the seeing limitations and reach the diffraction limit of large ground-based telescopes.

In the past few decades, a number of sophisticated post-detection image processing methods were invented to remove deleterious effects of atmospheric turbulence and restore the original astronomical objects. Speckle masking imaging is one of the methods that is commonly used in solar observations to obtain high quality, near diffraction-limited images of fine structures on the solar surface. In speckle masking imaging, each reconstructed image requires a sequence of short-exposure (less than 10 ms) images, i.e., interferograms, to ‘freeze’ the wavefront aberrations which makes it possible to separate the object information from information about atmospheric turbulence. The object should not change while the interferograms are taken. Since the upper limit of solar photospheric proper motion is about 2 km/s and the typical pixel size is about 0.1'' or 70 km on the surface of the Sun, the interferograms should be taken within 35 seconds. This renders the number of interferograms that are available for each reconstruction to a couple of hundred considering the read-out speed of today’s large format CCD camera.

Despite the maturity of the speckle masking method and the excellent images that have been obtained over the years, the application is not used on a daily basis because of the huge volume of data and the very computation-intensive data processing. For a moderate observing day of 6 hours, the amount of data will be about 70 Gbytes, assuming a 12 bit, 1024×1024 pixels CCD camera is used. The digitization depth is 12-bits corresponding to 2 Bytes in memory. 150 interferograms are obtained each minute for every reconstructed image. Usually, the data has to be transferred from the camera control computer to other computers for processing, or stored on tapes for post processing. The whole process involves extensive time overhead. The processing time for reconstructing one image varies from 20 minutes to about 4 hours depending on different program parameter settings and

image formats. Time lag between observations and data analysis makes it impossible for rapid response, such as needed for flare forecasting and space weather prediction. Furthermore, considering today's computer technologies, the time lag renders the whole scientific enterprise less efficient than it needs to be. In order to monitor the evolution of fine structures on the solar surface and study the link to solar atmosphere, transition region, corona and the effects on space weather, a system that can use the full power of speckle masking imaging to obtain high-spatial resolution images of solar surface in near real-time has to be developed.

“Moore's Law” states that the number of transistors per integrated circuit, hence the computing power at a given cost, doubles every 18 months. Indeed in the past several decades, Moore's Law has been maintained. The invention and rapid development of microprocessors and personal computers (PC) have changed the concept of computation. Despite the improvement of computational speed of processors, it is still impossible to use speckle masking imaging method to obtain relatively large-field of view (FOV) solar images, e.g., 1024×1024 , which is necessary to cover a entire solar active region, in real-time with a single CPU. The only solution to this problem is to use parallel computers to speed up the processing. So far the power of parallel computing has not yet been exploited in experimental solar physics. Parallel computers in super computing centers have been used for numerical calculations in astrophysics, but they cannot be used for real-time data processing because the observational data cannot be transferred to a super computing center in real-time. As the networking infrastructure evolves, the vision of using a Network Of Workstations (NOW) or dedicated computer clusters as one large parallel/distributed computing environment has begun taking shape. This technology makes it possible to build powerful parallel computing environments out of commercial PCs at a relatively low price. The speckle masking algorithms fit perfectly in such a computing paradigm. This enables solar physicists to apply parallel computing techniques to process solar data in near real-time to obtain high quality, near diffraction-limited images of solar surface fine structures.

Parallel processing of solar data will provide a new window through which solar physicists can observe the Sun in exquisite detail to study the evolution of granulation, filigree, pores, sunspots, prominences, filaments and flares. The development of multi-threaded and parallel numerical algorithms for high-spatial resolution imaging and multi-dimensional spectroscopy becomes even more important in the context of proposed, next generation, 1- to 4-m class solar telescopes, such as the New Solar Telescope (NST) at BBSO, ATST (Keil et al. 2003), GREGOR (Volkmer et al. 2003) and NSST (Scharmer et al. 1999).

In this section, an implementation of a near Real-Time Imaging Reconstruction (RTIR) system using the speckle masking method via parallel computing is introduced. The goal of this system is to obtain large-FOV, high-spatial resolution, near-diffraction-limited images of solar surface at a 1-minute cadence. As of now a system has been built that can reconstruct 1024×1024 pixel interferograms at 1 minute cadence. In the future, a system with 2048×2048 pixel images will be built. The scientific studies that will be carried out using these data and the questions to be answered include:

1. The evolution of pores and sunspots, and the formation of penumbra.
2. Localized changes of magneto-convection during penumbra formation, the coupling between the turbulent convective motion and the magnetic field from the photosphere and chromosphere, to be correlated with features embedded throughout the transition region, and finally the corona.
3. The importance of the local environment, such as nearby filigree and magnetic knots, emerging flux in the form of elongated dark channels, or pre-existing photospheric flow fields, in the context of penumbra formation;
4. What is the role of light-bridges and umbral cores in penumbra formation?
5. Are Ellerman Bombs near the tips of penumbral filaments stationary and are they predominantly located near magnetic neutral lines? Do the chromospheric Ellerman Bombs have counterparts in UV and EUV from TRACE and SoHO.

6. What is the response of the transition region and corona to the sudden appearance of the penumbra? Are there distinct features, which are related to coronal loop heating and emission that can be attributed to the abrupt change of the photospheric magnetic field topology?
7. Cross-calibrate the various existing two-dimensional spectro-polarimeters, e.g., IRIM, VIM (Denker et al. 2003), TESOS (Kentischer et al. 1998), and TIP (Schlichenmaier & Collados 2002), to yield a consistent reference frame for the theoretical interpretation of penumbra formation.

The data will also be used in monitoring and tracking active regions on the Sun and helping space weather predictions.

In the following sections, a detailed description of the RTIR system is given. In section 3.2, the hardware and software environment of the RTIR system is introduced starting with a small test system that was built before the final RTIR system. The hardware environment of the RTIR system is introduced in section 3.3. Section 3.4 is a detailed account of the implementation of whole system. The testing results, summary of the system and discussion is described in Section 3.5.

3.2 Hardware and Software Environment of RTIR System

3.2.1 Hardware Environment of RTIR System

The RTIR system hardware was implemented using a commercially built and ready-to-use computer cluster. This reduced the development time and enabled developers to focus on the implementation of the software system to fulfil the scientific goals of the project. A Beowulf class cluster computer is a variant of NOW. The network of the Beowulf cluster is configured in such a way that only one node, i.e., the master node, can be seen by the outside network. All nodes are dedicated to the cluster. This helps to ease load balancing problems, because the performance of individual nodes are not subject to external factors.

In addition, since the internal network is isolated from the external network, the network load is determined only by the application running on the cluster.

Figure 3.1 shows a schematic view of the final RTIR system. The RTIR system consists of the camera control computer and a 16-node Beowulf cluster. Each node of the cluster contains dual AMD 1800+ Athlon MP processors, 512 MByte memory and 60 GByte hard disk. The cluster is a hybrid of a distributed and shared memory parallel computer, which is a trend that is fast gaining momentum in modern message-passing parallel computers. All nodes are connected to a 100 Mbit ethernet switch and form a private network. The cluster can be monitored and administered via the master node, which has two network interfaces. The camera control computer is an ordinary PC with the Linux operating system. It has two network interfaces: One is connected to the switch of the cluster and configured as an extra node of the cluster and the other one is connected to the LAN for the camera and telescope control computers.

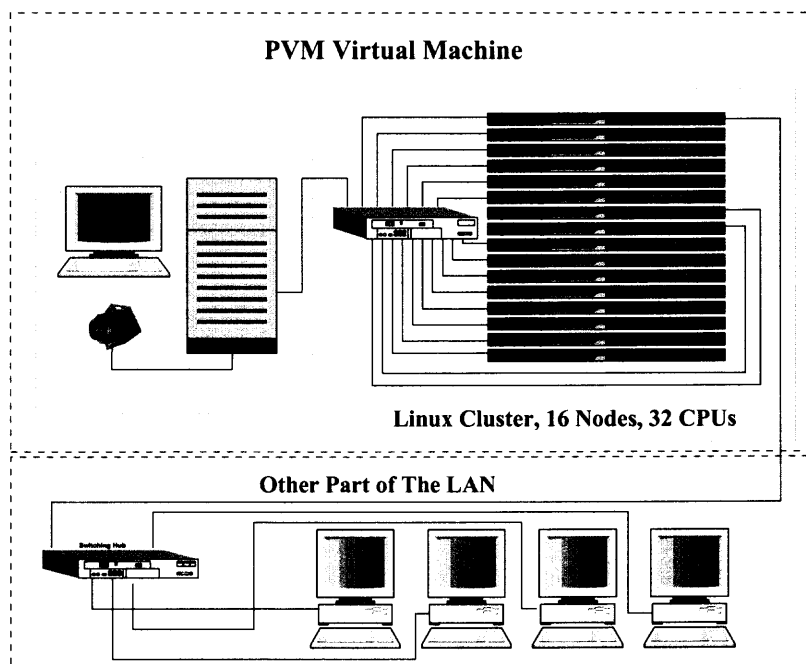


Figure 3.1 A schematic view of the Near Real-Time Imaging Reconstruction system at BBSO.

The camera control computer uses an EDT PDV imaging board as interface to a

1024 × 1024 pixel, 12-bit, DALSA 1M15 camera. The speckle images are taken at a maximum rate of 15 frame per second. The Dalsa 1M15 camera is a commercially built high quality, high-speed, and low-noise CCD camera.

The main design difference between this final setup and the test system described below is that the camera control computer is part of the Beowulf cluster. The change of network topology not only enhances I/O performance and avoids network conflicts but also simplifies the step to startup processes in the cluster.

3.2.2 Software Environment

In order to enable clusters to be used cooperatively as a general-purpose, flexible, parallel computing framework, a message passing library needs be used. Parallel Virtual Machine (PVM, Geist et al. 1994) is the de facto standard message passing interface that is used very commonly on many clusters. It is a very flexible message passing system that enables the use of any parallel programming paradigm. The PVM library was chosen because of its ability to create fault tolerant applications and its powerful set of dynamic resource manager and process control functions.

The GNU/Linux is used very commonly in Beowulf clusters because of its low price, high performance, and high reliability. GNU/Linux is a UNIX-like operating system. Linux based clusters are becoming so popular and powerful that nearly twenty percent of the top 500 supercomputers are Linux based NOWs or clusters (see <http://www.top500.org/> for more information) and as of June 2003, a Linux cluster by Linux Networx ranks third of the world's most powerful computers. The cluster of the RTIR system uses a modified version 7.2 Redhat (<http://www.redhat.com/>) GNU/Linux with 2.4.14 kernel. The kernel is compiled with MOSIX (<http://www.mosix.org/>) to enhance the distributed computing capability and PVFS (<http://www.parl.clemson.edu/pvfs/>) for enhancing parallel I/O performance. The kernel is specialized for SMP computers so the full ability of the clusters can be exploited by multi-threaded programming in addition to the distributed parallel com-

puting.

The image reconstruction algorithm relies heavily on Fast Fourier Transforms (FFTs). The Fastest Fourier Transform in the West (Frigo & Johnson (FFTW, 1998). See <http://www.fftw.org/> for more information.) was used in the reconstruction program. FFTW is a freely available C library which calculates FFTs very efficiently. FFTW adapts the computation of the FFT automatically to any particular computer hardware. This self-optimizing approach yields not only an excellent performance but also allows for easy scalability.

The non-commercial version of the Intel C/C++ Compiler for Linux is used to improve the efficiency of the generated code. Experiments have shown that the Intel Compiler generated codes are about 30% faster on average than codes generated by the GNU compiler, which is generally available on GNU/Linux systems. The GTK+ graphical interface toolkit and Simple Direct Media Layer (SDL) were used to create the camera control interface.

3.3 Test System

Before the RTIR system was built, a small test system was implemented as a test bed. The development of the RTIR was carried out on this test system. This small system consisted of a two-node Beowulf cluster (Denker et al. 2001). Each node of this cluster was a shared memory Symmetric Multi-Processors (SMP) machine, which had two 500 MHz Pentium III processors, 512 MByte of memory, and 11 GByte of disk space. The two nodes were connected using 100 Mbit Ethernet. Due to the simplicity of this small cluster, four network interface cards and two crossover cables were used instead of a network switch. The parallel computer is connected via a separate Ethernet link to a switch and subsequently to the camera control computers and telescope control computers, as well as other parts of the LAN. Figure 3.2 shows a schematic sketch of the hardware configuration.

The test system used a modified RedHat GNU/Linux with a 2.2.13 kernel for SMP. The PVM 3.4.3 version library was used in this test system as message passing library. A

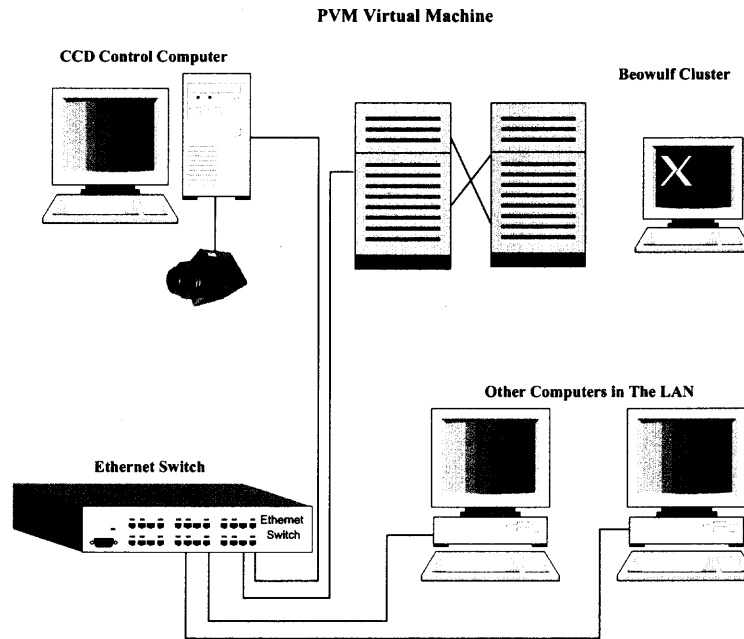


Figure 3.2 A schematic view of the test system that was used to develop the RTIR system.

parallel implementation of the speckle masking method was specially developed for this two-node cluster. Speckle images collected with a 256×256 pixel, 12-bit, 100 frame per second (fps) Dalsa CA-D1-256T CCD camera were used to test the first version of parallel implementation. Although there is not a dedicated camera control computer for this test system, to simulate real observation environment, test data were fed to the cluster from a computer that was connected to the master node of the cluster via LAN. This computer and the cluster formed a virtual machine during the computation. This configuration created a couple of difficulties during the data processing. First, because the cluster used a private network, neither the node could not be accessed from outside network. A special version of PVM was used to start processes on both nodes. Second, the data transfer between the data computer and each node was slow because all the data had to go through the master node.

Test results showed that it took 57 seconds to reconstruct one image from 100 frames of 256×256 pixel interferograms. In order to study the scalability of this still crude parallel version of the speckle masking algorithm, interferograms were taken by a

1024 × 1024, 12-bit depth Dalsa 1M15 camera and transferred to this test system. It took about 1220 s to reconstruct 1024 × 1024 pixel images, 660 s for 768 × 768 pixel images, 270 s for 512 × 512 pixel images. The smaller size speckle images were cropped from the original 1024 × 1024 pixel images. The results proved that the parallel version of the speckle masking reconstruction program scales efficiently on this test system. With this result, the design concept of the system has been validated and the feasibility of processing larger data sets with high cadence has been verified.

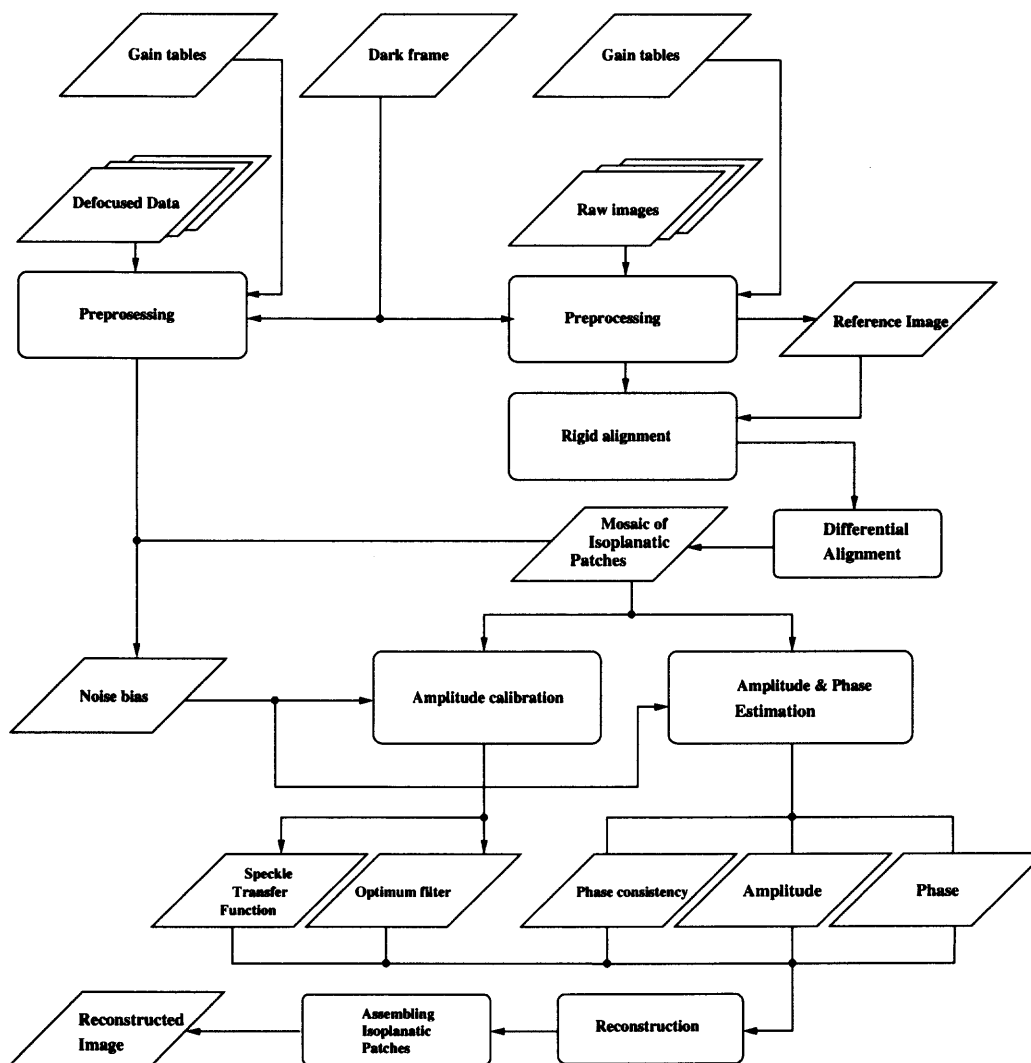


Figure 3.3 The overall procedure of the speckle masking imaging method. The parallelograms denote data sets that are used or produced during the processing. The rectangles denote operations on the data.

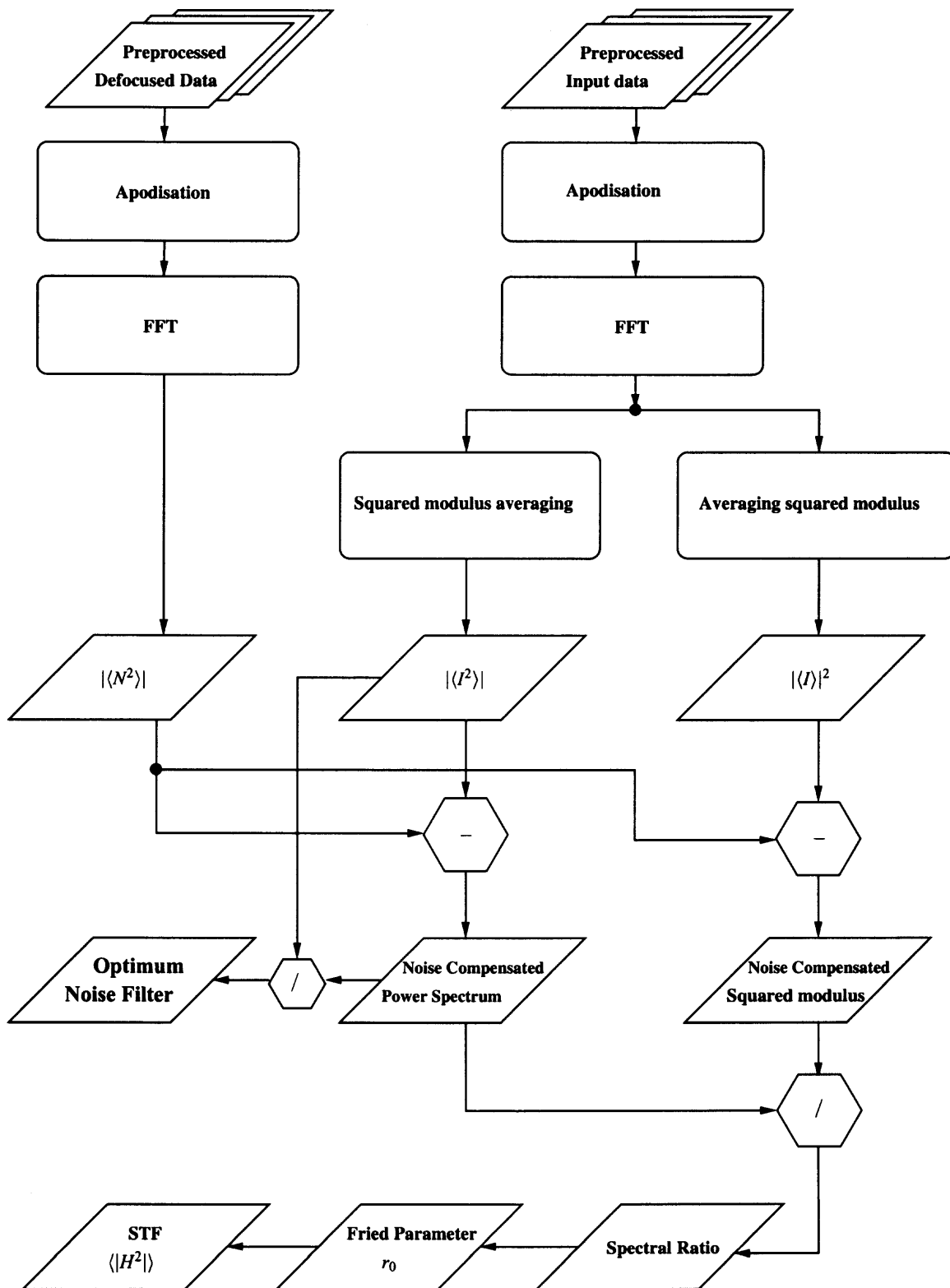


Figure 3.4 The flow diagram for computing the Fried-Parameter, r_0 , generating the amplitude calibration and optimum noise filter.

3.4 Implementation

3.4.1 Speckle Masking Algorithm

Figure 3.3 shows the overall procedure of speckle masking imaging. The physical principles were discussed in Chapter 2. The first steps in preprocessing the data concern the usual corrections utilizing the averaged dark frame and gain table. The image displacements within the sequence are then removed with respect to the image with the highest root mean square (rms) contrast. The noise level of the raw images has to be estimated and removed subsequently. The noise power can be estimated by using a set of defocused images taken with the same optical setup as the short-exposure speckle images. Defocused data are taken at the beginning of the observations using the averaged dark frame and their respective gain table. Care has to be taken to ensure that the average light level is same as for the short-exposure speckle images. Since speckle interferometry is only valid for a small region, i.e., the isoplanatic patch, the interferograms have to be segmented into a mosaic of partially overlapping images with sizes according to the isoplanatic patches. Differential image motion, i.e., image motion on the scale of the isoplanatic patches, are calculated and must be removed for each set of isoplanatic patches. Noise bias estimates for all stacks of isoplanatic patches are calculated using the preprocessed defocused data. The speckle transfer function (STF) is derived from Korff (1973)'s model STF, which is described as a function of only one parameter, the Fried-parameter, r_0 . r_0 is estimated by applying the spectral ratio technique (von der Luehe 1984). Figure 3.4 shows a detailed flow diagram to calculate the noise bias and STF. The amplitudes of the object's Fourier transform are estimated and corrected according to the classical speckle interferometric method of Labeyrie (1970). To derive the phases of the object's Fourier transform, the bispectrum is calculated and the phases are estimated using the phase closure relation recursively. Figure 3.5 shows the corresponding flow diagram to estimate amplitudes and phases. Back-transformation of the modulus and phases of the object's Fourier transform yields a mosaic of partially overlapping isoplanatic patches. These reconstructed isoplanatic patches are aligned accurately

and assembled into the final reconstructed image.

3.4.2 Camera Control Interface

Due to the many specialized operations of speckle masking observations, a dedicated camera control interface had to be developed for the RTIR system. The camera control program grabs images from an EDT PDV imaging board installed on the camera control computer. The camera is controlled by the imaging board using a serial cable through the camera's serial interface and the data are transferred using a custom-made, high-density data cable. The camera control program is a graphical user interface (GUI) program implemented for X Windows systems. The advantages of using a GUI are ease of camera setup, and presentation of a live-display, which will aid in adjusting the telescope focus and target selection. The camera control program is written in C using the GTK+ graphical interface toolkit and the SDL library.

The GUI consists of two windows. One window is used to display images. In this window, the observer can also select with the mouse pointer the ROI for which the contrast of the image is computed. All control functions are grouped in four tabs, which are contained in the main window. The image display window was written using the SDL library in order to get the maximum display speed for the live display. The control window was written with the help of the GTK+ graphical interface toolkit. The functions of the camera control interface include initializing and setting up camera control parameters such as exposure time, gain factor, timeout, etc.; Setting up parameters used in the observations such as the number of images taken in each iteration, the number of raw images used in reconstruction, etc.; Adjusting display settings of the image display window; Setting up a FITS header that contains information about the observation that is necessary for the reconstruction, e.g., wavelength and FOV; Selecting different kind of images, e.g. dark currents, defocused images and raw images etc., to be grabbed; Starting processes in the cluster and distributing all of the data to each processor for reconstruction.

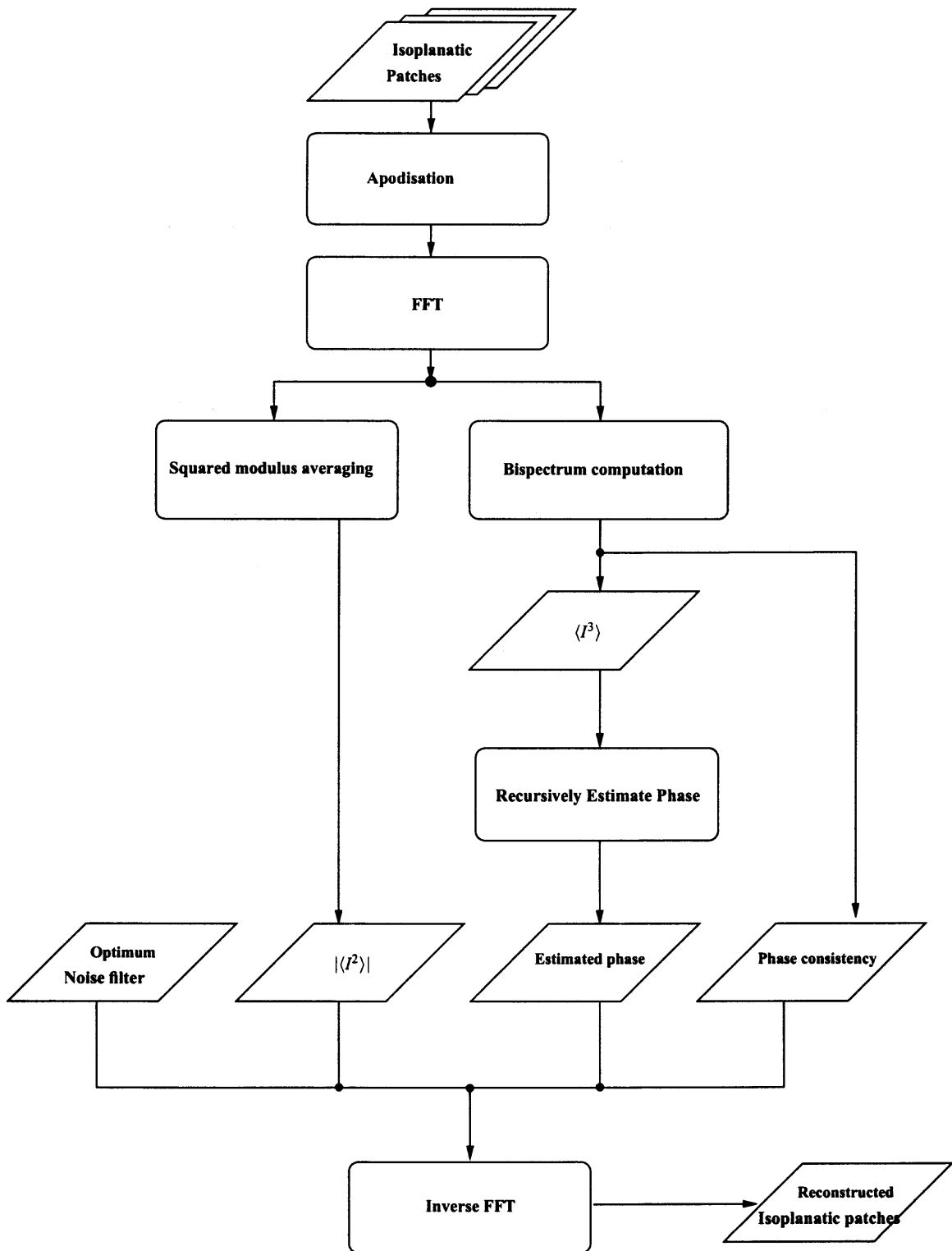


Figure 3.5 The flow diagram showing the estimation of Fourier amplitudes and the phases and getting the reconstructed isoplanatic patch through inverse FFT.

At the beginning of each observation, some calibration data sets, such as dark frame, gain tables, and defocused data, have to be taken. Dark frames are generated by recording images with conditions identical to science observations except the light beam is blocked out of the CCD camera. This sequence of dark frames is averaged to yield the mean dark frame. A gain table is constructed by averaging a sequence of images taken while the telescope is scanning randomly across the Sun near the disk center with identical conditions as for the science observations. Solar surface features will be smeared and effectively eliminated due to the isotropic nature of granulation. The mean dark frame is then subtracted to derive the gain table. Defocused data are taken by shifting the camera from the primary focus of the telescope and adjusting the light level to the same as that of the interferograms. If defocusing is not sufficient, a holographic diffuser may be used to obtain uniformly illuminated images. The gain table for defocused data is taken under the same conditions as the flat field image by scanning the center of solar disk to ensure that no solar signal is present in the subsequent noise analysis.

After all necessary information, such as wavelength and FOV, is gathered and all supporting data are taken, the speckle masking reconstruction process is started on all nodes of the cluster. The calibration data and information necessary for the reconstruction process are distributed to every node of the cluster. Defocused data are divided and distributed to each node for parallel processing. After these steps, raw images are taken and distributed evenly to each node. Finally, the reconstruction process begins.

3.4.3 Parallel Implementation of Speckle Masking Method

The image reconstruction program was originally developed in the Interactive Data Language (IDL). Due to the interpretive nature of IDL, the program executes inefficiently, e.g., on an Intel Pentium III 500 MHz computer, it takes about 30 minutes to reconstruct a 256×256 pixel image out of 50 short-exposure raw images. In order to improve the efficiency and to meet the requirements of a RTIR system, the program was transformed to a

serial C language program and parallelized to adapt to the distributed computing environment.

The speckle masking imaging algorithm is naturally suited for parallel processing: (1) The data have three dimensions (one temporal and two spatial dimensions). (2) The data have to be segmented into stacks of isoplanatic patches. Because almost all operations are carried out on stacks of isoplanatic patches, corresponding to the temporal dimensions, the parallelization of the speckle masking algorithms is based on an explicit message-passing model using the inherent data parallelism. At the beginning of each iteration, the data are first segmented in the time dimension, i.e., each computational node only receives parts of all images. This is because the segmentation scheme of isoplanatic patches can only be obtained after image motion and the differential image motion has been eliminated. After the interferograms are divided into isoplanatic patches, the data are redistributed because the subsequent operations are on the stacks of patches instead of on a whole image.

Figure 3.6 shows the data flow and processing steps of the parallel realization of the speckle masking algorithm. The supporting data sets, including average dark frame and gain tables, etc., are distributed to all computational nodes. This will not impact the network capacity very much because of the small amount of data. Although the defocused data need only be taken once, to reduce network traffic and process it parallel, it is divided evenly to each computational node. Each node owns and processes only part of the data at the same time.

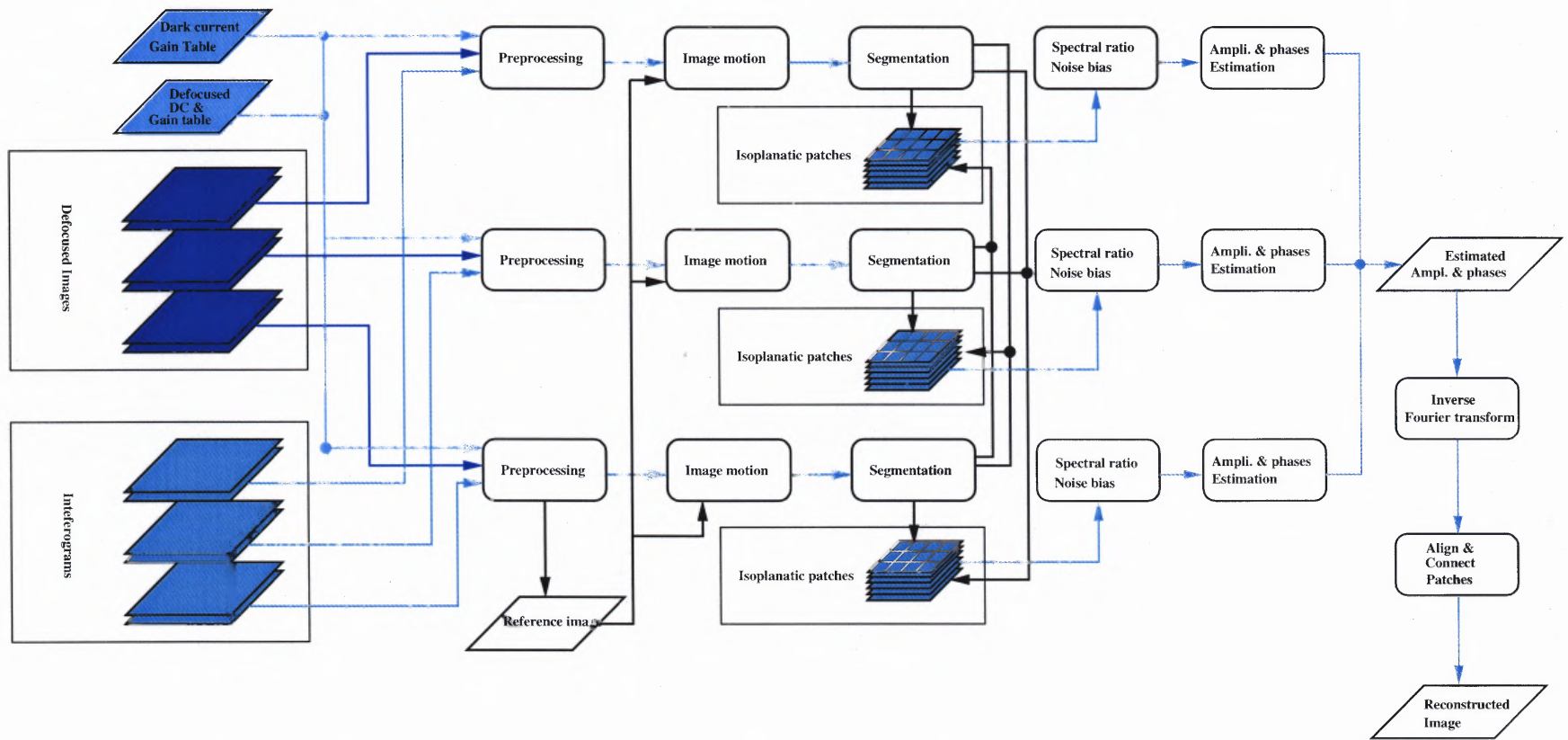


Figure 3.6 The data flow diagram of the RITR system. Note that only part of the data exchange between the nodes during the parallel processing are displayed in the figure. The figure does not represent the real configuration of the cluster used in the RITR system. Three nodes are drawn to illustrate the principal of the system.

After each computational node receives all of the calibrating data, the reconstruction iteration is started. Raw images are distributed and processed in parallel on each node. In order to find the reference image, which has high contrast, the rms-contrast values obtained during preprocessing are sent to all the nodes. On each node the index of the image with the highest rms-contrast value is obtained and the node that has it sends it to all the other nodes. Then the image motion is calculated against the reference image and distributed to all nodes. Based on the image motion information the images are segmented into a mosaic of overlapping isoplanatic patches. The differential image motions of these stacks of patches are also calculated and the patches are shifted to account for the motions accordingly. Because the subsequent calculations are all performed along the temporal axis, each node needs to obtain the remaining portions of the isoplanatic patches that are still on the other nodes.

Load balancing is an important task during these processing steps, otherwise there will be a lot of time wasted in waiting for nodes that fall behind in computation. In the RTIR system, load balance is achieved by distributing an exact, predetermined work load to each node. Each node runs the exact code and works on the same amount of data. Since all of the computational nodes are dedicated to processing and are configured the same way, it takes each node almost the same time to finish each step of the data processing.

During processing, some necessary intermediate data that are vital for the further processing steps are calculated and stored on each node. These data have to be exchanged and distributed to all the nodes. On each node, asynchronous routines are used to send the portion of necessary data it owns or produces to other nodes. This means the node resumes its processing once the message is safely on its way to the destination nodes and does not wait for the confirmation of the arrival of the message. Synchronous receiving procedures are used to receive data sent from other nodes, since it makes no sense for one node to begin before obtaining the necessary data. These receiving procedures also serve as a barrier points to the whole parallel processing task.

Multi-threaded programming allows very fast shared memory communication between concurrent sections of a program on an SMP machine. Therefore, on each node, the reconstruction process is implemented using multi-threads. The portions of data are further divided and handled by individual threads. Because Linux Thread is in kernel mode, multi-threaded programming can exploit the full computational power of the specific CPUs.

3.5 Results and Discussion

The RTIR system was tested on July 10, 2003. The observations were obtained with the 65 cm vacuum reflector at Big Bear Solar Observatory. A continuum window of 520 nm was used. A 1024×1024 pixel, 12-bit, 15fps Dalsa 1M15 camera was used. 300 raw images were taken at 4 ms exposure at 15 fps and among them 150 interferograms with highest rms-contrasts were selected. The FOV of the images was $80'' \times 80''$.

In this observing mode the system worked at 1-minute cadence. Figure 3.7 shows a reconstructed image. The penumbral filaments, penumbral grains, granulation, and filigree in Figure 3.7 show details down to the diffraction limit of the telescope, which is $\lambda/D = 0.165$ seconds of arc at 520 nm, corresponding to 120 km on the solar surface.

The RTIR system is the first system to obtain high spatial, high temporal resolution images of solar surface fine structures by post-facto processing near real time. The system will benefit the whole solar physics community because of BBSO's open data policy. All data will be available openly to whomever requests them. In order to aid the prediction of the effects of solar activity on the space environment, the RTIR system will be integrated into the web data publishing system of BBSO. The diffraction limited images produced by RTIR will be put on the web page of BBSO regularly during observations.

Even though the RTIR system is working now, there are many aspects that can be and should be improved in the future. At the moment PVM is used as the message passing library. The experience with the RTIR system shows that it is a highly reliable system. Message Passing Interface (MPI) is an industrial standard for writing message-

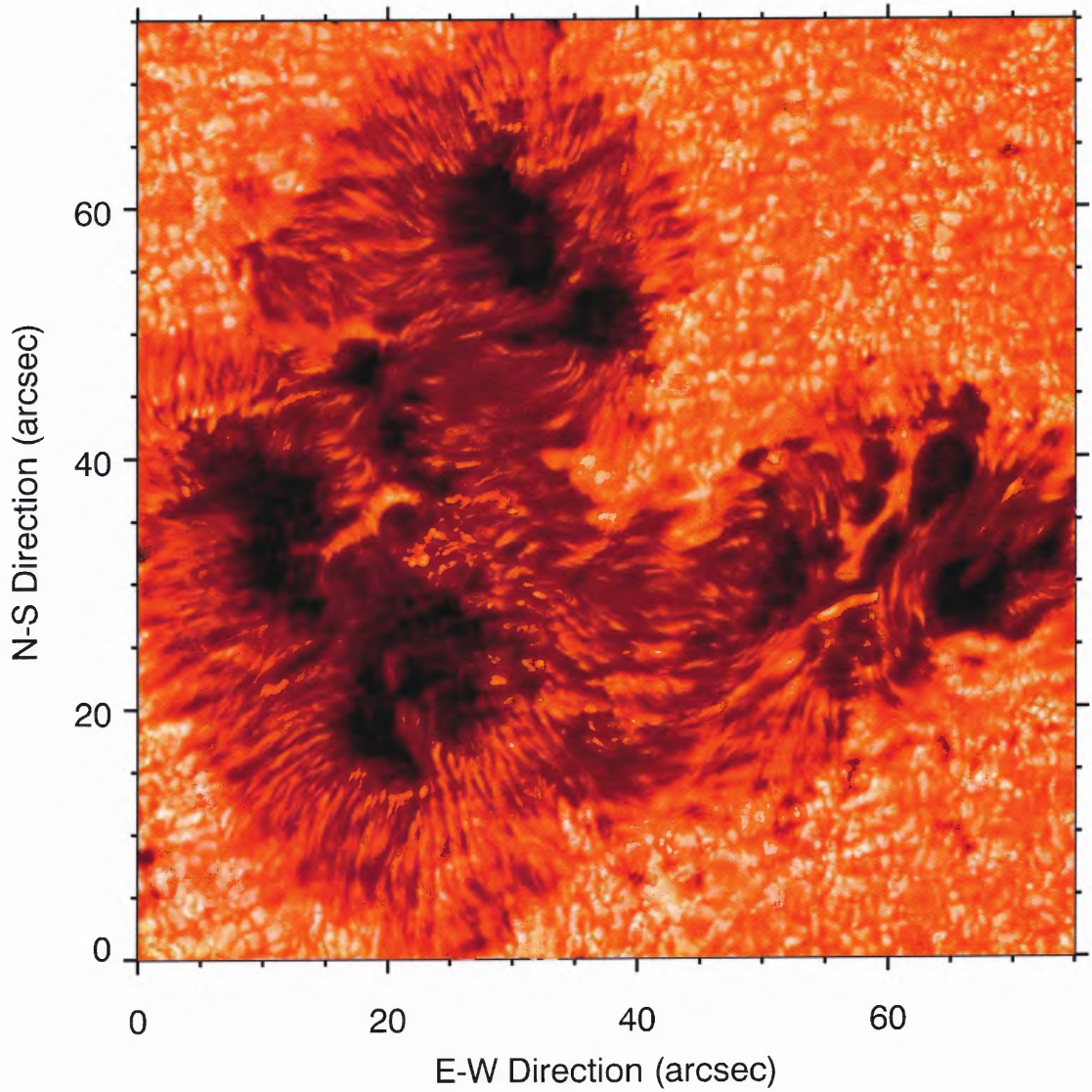


Figure 3.7 Speckle reconstruction of active region NOAA 10375 on 2003 June 10 at 19:58 UT. The Fried-parameter was $r_0 = 13.2$ cm.

passing based parallel programs. Compared with PVM, MPI provides more features, such as more point-to-point and collective communication, parallel I/O, etc. The main strength of PVM is its ability to start processes dynamically in the cluster. With more and more implementations according to the MPI 2.0 standard, MPI is catching up in these areas. In the future, a new RTIR system using MPI will be built. Using the rich set of features of MPI, the development of the system should be greatly simplified.

In order to improve the RTIR system further to reconstruct 2048×2048 pixel images, in addition to improving the computational power of the cluster, network traffic has to be reduced. At the moment, the program has been made so that each node has to send portions of stacks of isoplanatic patches to the respective nodes. Since the amount of data that needs to be transferred is huge, this process takes about 10 seconds. This time can be reduced by letting each node calculate on all the isoplanatic patches it owns and only the intermediate results are collected. This could save most of the time involved in transferring the isoplanatic patches.

The current implementation evaluates the noise power for every iteration of reconstruction. This could be relaxed to performing the computation once, and using it throughout the whole observation sequence. Even though the time saved by removal of the noise power evaluation on every iteration is short, it still deserves a try.

CHAPTER 4

SPECKLE MASKING IMAGING OF SOLAR ACTIVE REGION NOAA 9539

To study flows and pores on the surface of the Sun, a high resolution observation of a solar active region using speckle masking reconstruction technique is presented. The data were recorded with a SMD 1M60 CCD camera using the 65 cm vacuum telescope at the Big Bear Solar Observatory (BBSO). The reconstruction procedures have been applied to a $39'' \times 39''$ region. The resolution of the images approaches the diffraction limit of the telescope, which is about $0.165''$ at 520 nm. Vector-magnetograms of the same region were also obtained with the Digital Vector MagnetoGraph (DVMG) system at BBSO's 25 cm vacuum refractor. These high resolution observations were aimed at a better understanding of proper motions of small-scale structures in solar active regions and their relationship to the underlying magnetic field. A new system for near real-time image reconstruction is introduced. Evolution of a pore is discussed. The pore was located underneath an up-flow detected in $H\alpha$ dopplergrams. At the end of the observations the pore fragmented into several magnetic knots.

4.1 Introduction

Solar pores are small sunspots that lack a penumbral structure. Because they are part of the early stage of sunspot evolution, they are important in understanding the mechanism of small-scale flux emergence on the surface of the Sun. The magnetic field lines in pores are almost vertical, however, the lines of force in sunspot penumbrae are highly inclined. Studying the evolution of pores can lead to a better understanding of the interaction between magnetic fields and the surrounding convective motions.

In order to study the fine structures in and around pores and sunspots, high spatial, temporal, and spectral resolution observations are needed. As introduced in Chapter 1,

the turbulence of the Earth's atmosphere limits the best resolution that can be obtained, even when large telescopes are used. Speckle interferometry was invented to eliminate the image degradation due to turbulence in the atmosphere. Speckle masking method (See Chapter 2) was used to get the high quality images that are studied in this chapter. Speckle interferometry provides impressive, reconstructed white-light images. These high-spatial resolution, near-diffraction limited images make it possible to study some of the physical parameters of small-scale magnetic features and their evolution. But the computational complexity of the algorithm restricts the application of this method. The processing of the data could previously be done only after the observations. This time lag renders it impossible to rapidly respond, which is needed for space weather predictions and flare forecasting. A system that overcomes these limitations and performs speckle masking observations in near real-time, i. e., in a time interval which is short (less than one minute) compared to the evolution time-scale of photospheric features has been developed.

The Advanced Technology Solar Telescope (ATST) is a next generation ground-based solar telescope. Because of many advanced technologies it will use, such as the integrated adaptive optics, low scattered light, infrared coverage, etc., ATST will be a most important tool for small scale magnetic flux tube studies and it will help to close the gap between theory and observations in this field. With its 4 m aperture and its state-of-the-art technology, the ATST will achieve a spatial resolution nearly an order of magnitude better than any existing solar telescope. Even though ATST will greatly enhance the capability of obtaining high resolution solar images, image processing techniques such as speckle masking imaging remain an important complement to adaptive optics, since the FOV is in principle not limited to the isoplanatic patch with speckle masking imaging.

4.2 Observations

The observation data were obtained with the 65 cm vacuum reflector at BBSO on July 15, 2001. At a wavelength of 520 nm, the diffraction limited resolution of this telescope is

$\alpha = \lambda/D = 0.08''$. A 12-bit SMD 1M60 CCD camera with 1024×1024 pixel was used in a 2×2 pixel binning mode to improve the signal-to-noise ratio. The camera supports only 8-bit digitization in the full frame mode. The image dimensions are therefore repinned to 512×512 pixel. The field-of-view (FOV) is $39'' \times 39''$ and the image scale is $s = 0.076'' \text{ pixel}^{-1}$.

The spectrograms were recorded at a frame rate of 30 frames s^{-1} and the exposure time was 4 ms. For each reconstructed image, 200 images were recorded. Only the 100 best images with the highest rms-contrast of the granulation were selected for speckle reconstruction. After each set of data was taken and saved to disk, which usually took about 20 s, a computer controlled mirror was used to direct the light beam to another optical bench on which dopplergrams ($H\alpha \pm 0.6\text{\AA}$) were taken at a 20 s cadence. The overall cadence was 1 min. At the same time, vector-magnetograms were recorded with the DVMG system at the 25 cm vacuum refractor at BBSO.

The target under study was active regions NOAA 9439 showing some interesting magnetic field configuration, such as delta-spots, mixed polarity, and flux emergence. The data set presented in this article focusses on a small region inside the active region. Figure 4.1 shows one of the speckle reconstructed images. This image shows a small sunspot with rudimentary penumbra, several pores, magnetic knots, and filigree. In this chapter the pores and its evolution are studied. In Chapter 5, the study of the formation of the rudimentary penumbra is presented.

4.3 Data Reduction

For each set of spectrograms, the dark current and flat field were first corrected. A median filter was used to eliminate the remnants of dust particles that were still presented in the spectrograms. The preprocessed spectrograms were aligned with respect to the spectrogram that had the highest rms-contrast by means of a cross-correlation analysis. Finally, speckle masking method in an implementation described by Denker (1998) was applied.

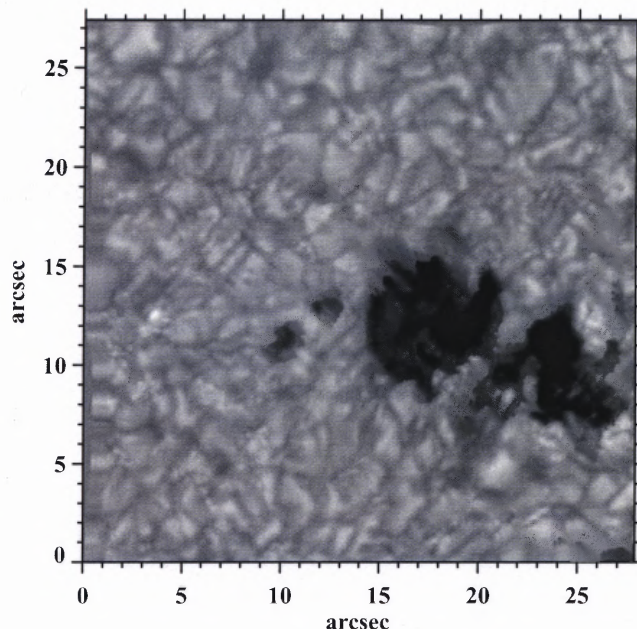


Figure 4.1 A speckle reconstructed image of the central part of active region NOAA 9439 observed at 20:14 UT on July 15, 2001.

In June 15, 2001, a total of 78 reconstructed images at a one minute cadence was obtained. Cross-correlation analysis was applied to these images and the image motions were removed. A destretching algorithm was used to register the images. Kernel sizes of 64×64 pixel and 32×32 pixel were used successively to register the images. Each image was registered with respect to predecessor. This enables us to eliminate the remaining differential image motion induced by seeing or slight misalignments that may have occurred while patching the mosaic together. A three-dimensional subsonic Fourier filter to remove brightness variations due to acoustic oscillations on the surface of the Sun. The cut-off velocity of the filter was set to 4 km s^{-1} according to the discussion of Hirzberger et al. (1997).

Local Correlation Tracking (November & Simon 1988) was used to measure the proper motion of the photospheric features. A Gaussian sampling window with a FWHM of $2''$ was used, which sets an upper limit for features that can be tracked. The time interval

between the correlated frames is 60 s. The flow maps were averaged to reduce noise. The duration of the averaging was about 75 min. The maximum velocity is about 0.6 km s^{-1} . Figure 4.2 shows the horizontal velocity field for the time series. Note the diverging flows around the two pores on the right hand side of the small sunspot.

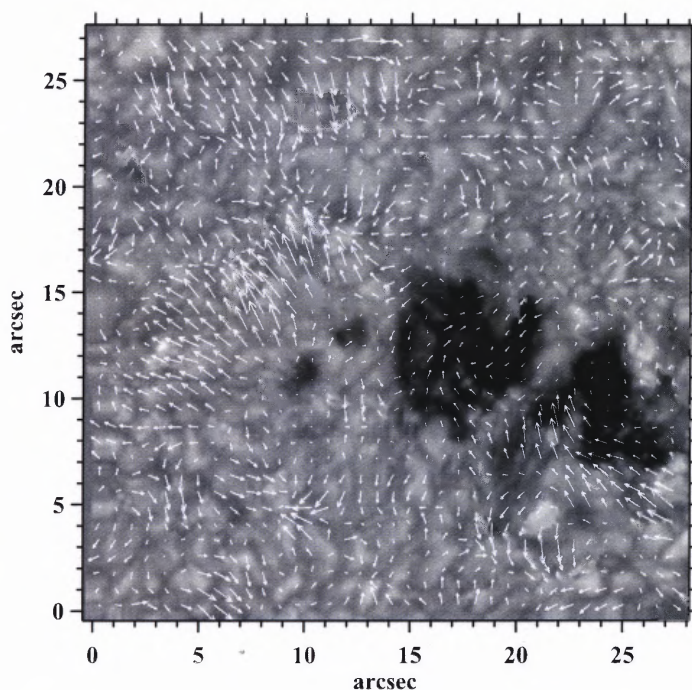


Figure 4.2 Flow map of the horizontal proper motions derived from a 75-minute time series of speckle reconstructed images.

dopplergrams were also obtained by subtracting images taken at $H\alpha - 0.6\text{\AA}$ from the images taken at $H\alpha + 0.6\text{\AA}$. Figure 4.3 shows a dopplergram taken at almost the same time with the image in Figure 4.1. The box in the image indicates the same region as in Figure 4.1. Vector-magnetograms were also obtained with the DVMG system at BBSO (Spirock & et al. 2001). Figure 4.4 shows a line-of-sight magnetogram taken at 20:12 UT.

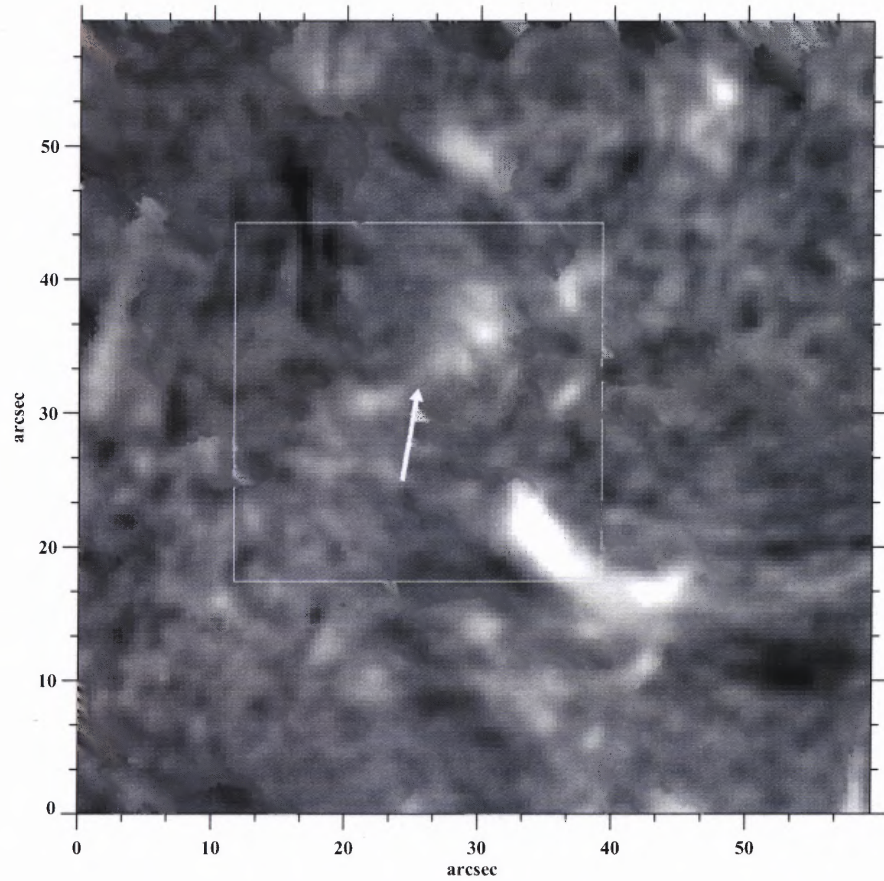


Figure 4.3 Dopplergram taken at 20:14 UT on July 15, 2001. The white box corresponds to the region of the speckle observations. The arrow indicates the down-flow area.

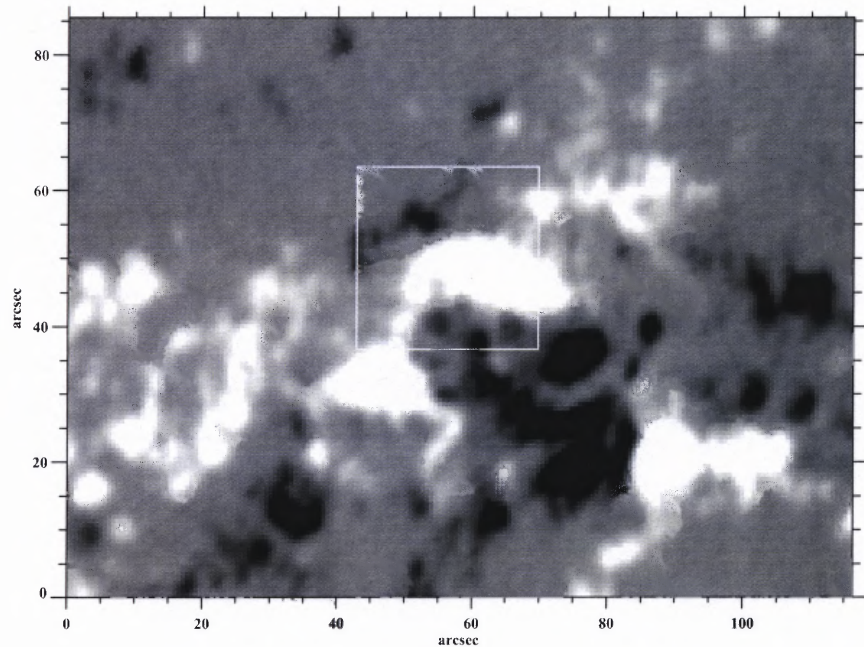


Figure 4.4 The line-of-sight magnetic field observed at 20:12 UT on July 15, 2001. The white box corresponds to the region of the speckle observations.

4.4 Results

The motions of one of the two small pores near the sunspot were followed. This pore eventually broke apart at the end of the observation. The observed lifetime of the pore was about 65 minutes. Another interesting phenomenon is a transient penumbra-like structure forming on the border of the pore before it breaks apart. Figure 4.5 shows the evolution of the pore and the penumbra-like structure.

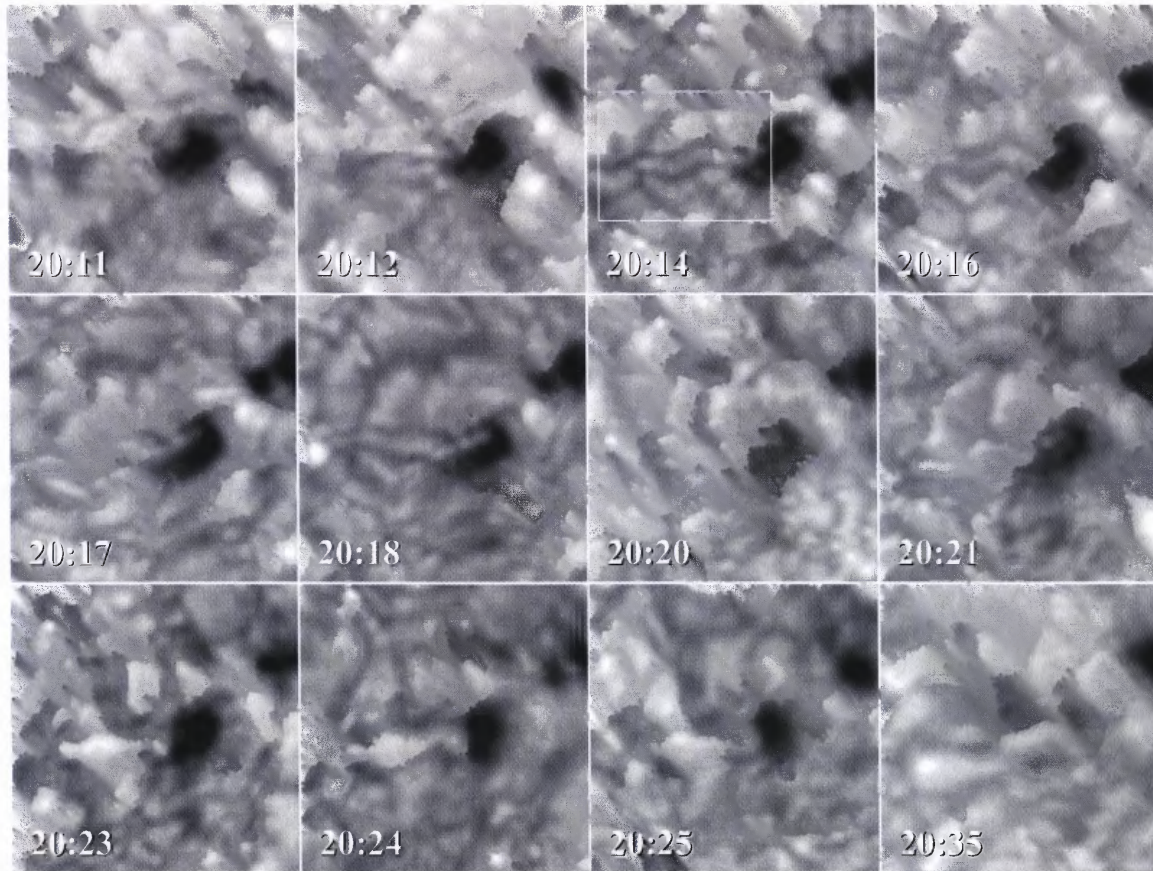


Figure 4.5 The evolution of the penumbra-like structure before the defragmentation of the pore. The FOV of the individual panels is $7.62'' \times 7.62''$. The last frame shows the fragments of the pores which dissolved into magnetic knots. The white box indicates a region that contains a peculiar filamentary structure. The times are given in UT.

The penumbra-like structure occurred twice, at the beginning of and at the end of the time series. During its first appearance, as the time went on, the structure grew longer and thinner. But suddenly at 19:41 UT, the two long dark filaments disappeared. Then at 20:11 UT a penumbra-like structure started to form again. It is very similar to the structure before. Again, two dark filament-like structures were attached at the border of the pore. The two dark filament-like structures also grew longer and thinner. At 20:27 UT the structure disappeared again. The pore broke apart soon after that. Sobotka et al. (1999b) reported similar observations. But in their observations, the pore with the filamentary structure did not decay after the filaments vanished.

It is also interesting to note that the observations do not show the horizontal flows of the surrounding granulation towards the pore as described in Wang & Zirin (1992). As Figure 4.2 shows, around the pore, on the other side of the sunspot, the granules moved dominantly away from the pore. The direction of the motions of the granules favor the same direction as the expansion of the filamentary structure.

From the $H\alpha$ dopplergram (Figure 4.3), it can be seen that there is an elongated down-flow region near the small pores. A magnetic neutral line aligned with the up-flow region also can be seen on the magnetogram (see Figure 4.4). The flow map (Figure 4.2) also indicates proper motions moving towards the down-flow area. The speed of the proper motions on the side of pores is much higher than the speed of the other side. The light bridge in the sunspot did not change very much during the observations. The proper motions along the light bridge region are negligible. The rudimentary penumbra of the sunspot also show a very dynamic behavior (See Chapter 5).

4.5 Discussion

A possible explanation of the fragmentation is as follows: In reaction to the up-flow and the opposite polarity of magnetic field near the pore, some of the flux tubes of which the pore consists began to incline more and more until they became nearly horizontal. The fila-

mentary structures can be interpreted as a signature of horizontal field lines. At some point the convection flow tore the flux tubes in the pore apart. These bundles of magnetic flux tubes drift away and form the magnetic knots that were formed after the defragmentation of the pore. The up-flow near the pore further supports the idea of a rising flux tube. Which might also be the reason why the inward proper motions that were observed by Wang & Zirin (1992) was not seen.

As shown before, the speckle masking method is a powerful instrument to obtain high spatial resolution images, which are necessary to study the dynamics of solar small-scale structures. But the computational complexity and the huge amount of data greatly restrict its application. The time lag between the observation and the reconstruction of the images made it previously impossible to monitor the changes in solar active regions, which is very important for space weather prediction and flare forecast. In order to overcome these problems, a system for real-time image reconstruction (See Chapter 3 for details.) has been developed.

CHAPTER 5

FORMATION OF A RUDIMENTARY PENUMBRA

In this chapter, high-spatial resolution observations of small-scale magnetic activity in solar active region NOAA 9539 are presented. The observations were obtained on 2001 July 15 using the 65 cm vacuum reflector and 25 cm refractor of the BBSO. The data sets include time-series of speckle reconstructed continuum images at 5200 Å, H α filtergrams (blue line wing, line center, and red line wing), and line-of-sight magnetograms. Two pores, which were separated by a light-bridge, were located in the central part of NOAA 9539. The formation of penumbral filaments near the light-bridge indicated a sudden change of the local magnetic field topology from almost vertical to strongly inclined magnetic fields, which allowed cool material previously suspended in a filament to stream downwards. During the downward motion of the cool material, H α dopplergrams revealed twisted streamlines along the filament. Finally, there are several well defined H α brightenings, Ellerman Bombs (EBs), occurring near the region where the down-flow of materials fell. The EBs reside near a magnetic inversion line and are stationary as opposed to EBs associated with moving magnetic features. It was also found that the horizontal flow field of the white light images derived from Local Correlation Tracking is different from the previous observations. The horizontal movements in the superpenumbrae of the leading sunspot and the following sunspots are opposite.

5.1 Introduction

A sunspot is a complex magnetic concentration on the surface of the Sun with distinct fine structures both inside the penumbra and the umbra. Solar pores are small sunspots that lack a penumbral structure. Because they are part of the early stages of sunspot evolution, they are important in understanding the mechanism of small-scale flux emergence on the sur-

face of the Sun. The magnetic field lines in pores are almost vertical, however, the lines of force in sunspot penumbrae are highly inclined. Studying the evolution of pores can lead to a better understanding of the interaction between magnetic fields and the surrounding convective motions. Two sunspot models are compatible with the observations. The cluster model (e. g., Parker 1979) and the monolithic flux-tube model (e. g., Choudhuri 1986). The interpretation of fine-structures such as umbral dots and light-bridges are very different in these two models. In the cluster model, the umbral dots are columns of field-free gas penetrating the vertical field lines inside the sunspot umbra, thus, the appearance and decay of umbral dots can be interpreted as the opening and closing of a 'magnetic valve'. In the monolithic flux tube model, umbral dots are tiny islands of gas near normal photospheric temperatures and manifestations of over-stable convection in a magnetic plasma. The simulations of magneto-convection by Weiss et al. (1996) and Blanchflower et al. (1998) show that when the intrinsic magnetic field strength becomes as strong as in a sunspot umbra, the flow structure will be completely controlled by the magnetic field. In such a situation some small and roundish convective cells (umbral dots) are ordered in some grid- or chain-like structure. When the magnetic field strength is not very strong, the convective flows field will become chaotic and the convective cells might escape from the magnetic field into the narrow lanes surrounding them.

Generation and dissipation of small-scale quiet solar magnetic features are responsible for the dynamics above the photosphere. Observations of small-scale magnetic fields, with the highest resolution possible, are crucial to understand mass and energy transport throughout chromosphere, transition region, and corona. The morphology and physics of sunspots and associated phenomena is carefully illustrated in the classical text by Bray & Loughhead (1964) and the hierarchy of solar magnetic fields has been reviewed by Zwaan (1987). The size spectrum of solar magnetic fields ranges from sunspots, pores, and magnetic knots to faculae and network clusters and finally to the theoretically predicted flux fibers with dimensions of just a few tens of kilometers. A collection of research papers

relating sunspot observations and theory were assembled in the monograph by Thomas & Weiss (1992). and Schlichenmaier et al. (1998).

This study focuses on the development of penumbrae as part of the intricate time-dependent structure of sunspots. The observations are aimed at a better understanding of magnetic field generation, i. e., the emergence and removal of flux. Advanced image reconstruction techniques allow us to shed some light onto the small-scale magnetic structure and dynamics of sunspots with an emphasis on the interaction of magnetic field and convective turbulence at the smallest observable scales. Many still-open questions are related to the abrupt transition from nearly vertical fields in pores to the strongly inclined fields in sunspot penumbrae: How does the sudden topology change of the magnetic flux fibers affect the magnetic field in the transition region and corona? What effect has the clustering tendency of emerging small-scale flux elements in active regions on the formation of (rudimentary) penumbrae? Is sea-serpent-like structure attributed to penumbral filaments responsible for small-scale chromospheric heating as observed in Ellerman Bombs (EBs)? These questions are drivers for observations with increased magnetic sensitivity, improved spectral resolving power, and appropriate temporal resolution at sub-arcsecond spatial scales.

The investigation of small-scale magnetic fields focuses on the question: What are the essential features that distinguish a sunspot from a pore? Pores can have diameters of up to $10''$, whereas the smallest sunspots have diameters down to $5''$. Rucklidge et al. (1995) developed a simplified model of the energy transport in sunspots and pores, which describes the transition from pores to sunspots as a function of the magnetic flux Φ and the radius R

Table 5.1 Observing Characteristics on 2001 July 15

Wavelength	Telescope	Start	End	Cadence	Images	Image Scale	Field-of-View
H α 6562.8 Å	25 cm Refractor	16:29 UT	23:35 UT	105 s	98	0.57'' pixel ⁻¹	300'' × 300''
Ca I 6103 Å	25 cm Refractor	16:24 UT	23:36 UT	105 s	95	0.62'' pixel ⁻¹	315'' × 315''
Continuum 5200 Å	65 cm Reflector	19:28 UT	20:44 UT	60 s	64	0.08'' pixel ⁻¹	39'' × 39''
H α 6562.8 + 0.6 Å	65 cm Reflector	19:10 UT	23:14 UT	35 s	265	0.39'' pixel ⁻¹	200'' × 200''
H α 6562.8 - 0.6 Å	65 cm Reflector	19:10 UT	23:14 UT	35 s	265	0.39'' pixel ⁻¹	200'' × 200''

of the sunspot/pore. Sunspots and pores are located on a hysteresis curve in the Φ, R -plane, and sunspots emerge from the pore branch at a sub-critical (with respect to both Φ and R) bifurcation point. At this point, lateral heat transport increases sharply and penumbral structures appear abruptly and rapidly, and become a robust feature in the evolution of the sunspot. The generation of a filamentary penumbra, the onset of the Evershed flow, and the change of the magnetic field topology takes place in less than 20 min to 30 min (see Leka & Skumanich 1998), which makes penumbra formation a challenging observational task and explains why many processes of non-linear convection involved in sunspot formation are still elusive.

The abrupt formation of a penumbra, the on-set of the Evershed flow, and the sudden change of the magnetic field topology should certainly affect the upper atmospheric layers. However, the exact mechanisms coupling photospheric flux tube dynamics with chromospheric activity and coronal heating are still elusive. EBs have been known to appear preferentially near young sunspots, where they are often concentrated at the outer boundary of the penumbra (Denker et al. 1995), especially when the penumbral filaments penetrate deeply into the granular pattern. EB observations, i. e., the intensity enhancement in the inner wings of strong chromospheric absorption lines, are not restricted to $H\alpha$ (Stellmacher & Wiehr 1991). Denker (1997) and Denker (1998) compare the appearance of EBs near sunspot penumbrae in speckle interferometric continuum and Na D_2 filtergrams. Even though EBs share many properties with facular points, filigree, or Calcium bright points, a proper classification according to their underlying mechanisms is still difficult (Nindos & Zirin 1998; Qiu et al. 2000). Qiu et al. (2000) compared the emission of EBs in $H\alpha$ and the ultra-violet (UV) at 1600 Å. They find that more than half of the EBs have well correlated emission profiles in the UV and $H\alpha$ and are preferentially located at the boundaries of unipolar magnetic regions, whereas the remainder of the EBs show only weak correlations and are located close to magnetic inversion lines.

Condensation of coronal material due to cooling and the injection of photospheric

material into the chromosphere are two competing models for the source of cool plasma in filaments and prominences. Chae et al. (2000) studied a reoccurring transient flow field in a system of small $H\alpha$ loops, which were associated with a cancelling magnetic feature. They concluded from these observations that filament mass injection by chromospheric reconnection is a possible mechanism to supply mass to filaments. Transient $H\alpha$ flows in the present observations are the result of a sudden change of the magnetic field topology caused by the formation of penumbral structure, which leads to advection of cool neutral plasma along field lines. The plasma in the $H\alpha$ loop is red-shifted and, hence, flowing downward. In many respects, this can be interpreted as the reverse process filament mass injection as described by Chae et al. (2000).

5.2 Observations

The observations were carried out on 2001 July 15 during good seeing conditions using the 65 cm vacuum reflector and the 25 cm vacuum refractor at Big Bear Solar Observatory (BBSO). The observing characteristics are summarized in Table 5.1.

The 65 cm reflector is a light-weight Gregorian telescope, which was originally built as a prototype for a space-based telescope. It is placed in an over-sized vacuum tank on an equatorial mount. A computer-controlled mirror system directs the light to three optical benches in a T -shaped configuration, which are mounted directly underneath the vacuum tank. The $H\alpha$ data were recorded with a 1024×1024 pixel, 12-bit CCD camera manufactured for the Orbiting Solar Laboratory (OSL), which was used in the 2×2 pixel banning mode in combination with a computer-controlled Zeiss filter. Filtergrams were recorded in the blue and red line wing of $H\alpha$ to measure chromospheric up- and down-flows in $H\alpha$ dopplergrams. The exposure time for the $H\alpha$ filtergrams was 48 ms.

The continuum spectrograms were obtained with a 1024×1024 pixel SMD 1M60 CCD camera manufactured by Silicon Mountain Design/DALSA using the 65 cm reflector. Due to the inability of the imaging board, a 512×512 pixel, 12-bit images in the 2×2

pixel banning mode of camera was used in order to improve the signal-to-noise ratio. Every minute, sequences of 200 short-exposure (4 ms) images were captured at a frame rate of 60 frames s^{-1} and saved to hard-disk for subsequent image reconstruction by means of the speckle masking technique. The field-of-view (FOV) was $39'' \times 39''$. The spectrograms were observed in the green continuum at $\lambda = 5200 \text{ \AA}$ and the bandpass of the interference filter was $\Delta\lambda = 60 \text{ \AA}$. The implementation and optical set-up of speckle masking technique were described in Denker (1998) and Denker & Wang (1998). The image reconstruction algorithm were originally developed at the Universitäts-Sternwarte Göttingen (de Boer 1993) and have been heavily modified for parallel-processing and real-time image reconstruction applications (Denker et al. 2001).

As a by-product of the image reconstruction process, the Fried-parameter r_0 was calculated with the spectral ratio technique (von der Luehe 1984), which basically determines the atmospheric cutoff $\alpha = r_0/D$, where D is the telescope diameter, by evaluating the ratio of the observed squared modulus of the average Fourier transform and the observed average power spectrum. The results of the spectral ratio technique are shown in Figure 5.1. The average Fried-parameter was $r_0 = 11.9 \pm 0.4 \text{ cm}$ at 5200 \AA , where the standard deviations reflects the temporal evolution of the seeing during the 76-minute long observing period. The highest value of the Fried-parameter was 13.1 cm. Since the Fried-parameter was computed from time-sequences of speckle images, each individual data point in Figure 5.1 is already an average over about 4 s and not an instantaneous measurement. Fried-parameters above 6 cm are generally considered good for solar observations and Fried-parameters above 10 cm indicate the excellent seeing conditions that can be encountered at a lake-site observatory. Some general aspects of the daytime seeing characteristics at BBSO and results from different seeing monitors are discussed in Goode et al. (2000) and Denker & et al. (2002).

The 25 cm vacuum refractor is mounted underneath the vacuum tank of the 65 cm telescope and shares the same equatorial mount. However, it has its own guiding system

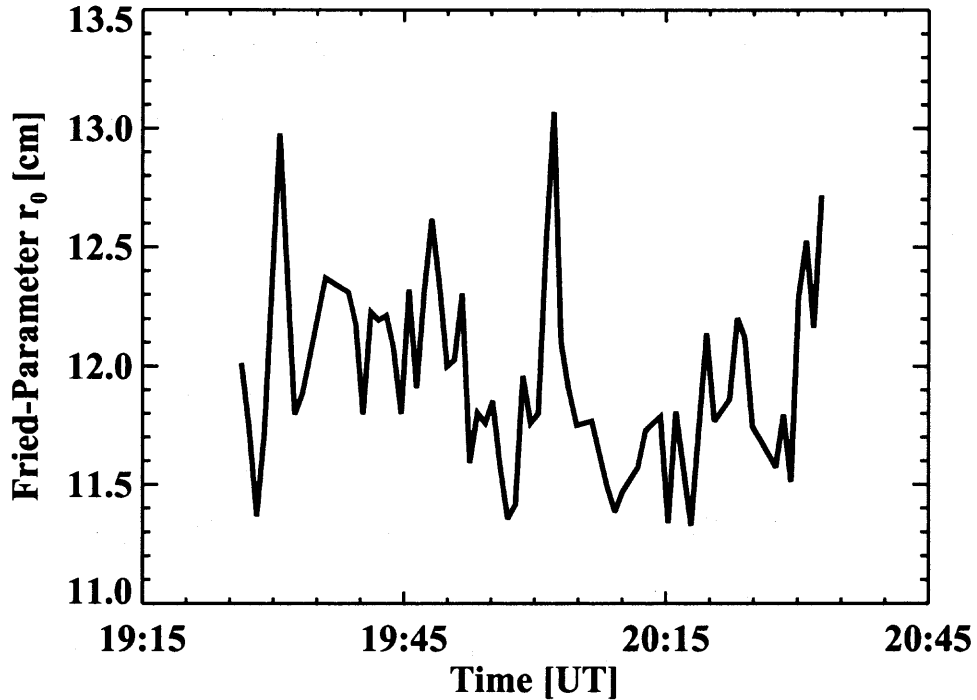


Figure 5.1 Temporal evolution of the Fried-parameter r_0 of BBSO on 2001 July 15.

so that both telescopes can be operated independently. The light can be directed to three parallel optical benches with a computer controlled mirror system. The typical FOV of the 25 cm telescope is about $300'' \times 300''$. The two side benches have usually a similar optical set-up, i. e., a Lyot-filter ($H\alpha$ and $Ca II K$ or $He D_3$) and a 512×512 pixels KX260 CCD camera manufactured by Apogee (Denker & et al. 2001). In the present study, only a Zeiss filter for observations in the $H\alpha$ line center was used. The bandpass of the birefringent filter was $\Delta\lambda = 0.25 \text{ \AA}$ and the exposure time was 40 ms. Since the flip mirror system directs the light to the side benches only for brief moments of time, they are removed from the straight-through light pass for the largest fraction of an observing cycle, which is dedicated to polarimetric measurements with the DVMG mounted on the center bench.

The basic principle of the DVMG system is similar to the supplanted BBSO video-magnetograph system (Varsik 1995). However, the polarization optics is now based on a combination of two nematic liquid crystals and a ferro-electric crystal. The ferro-electric

crystal is used for fast modulation at a rate of 30 Hz, whereas the nematic liquid crystals determine the polarization state for the Stokes-I, -V, -Q, and -U observations. The magnetograms were recorded by a 1M15 CCD camera manufactured by Silicon Mountain Design (SMD). The 1024×1024 pixel camera is used in the 2 pixel binning mode and individual frames have a dynamic range of 12 bit. The magnetograms were obtained in the line wing of the Ca I line at 6103 Å. The bandpass of the Zeiss filter was $\Delta\lambda = 0.25$ Å. A detailed description of the DVMG system and its observing modes is given by Wang et al. (1998) and Spirock & et al. (2001). The DVMG data consists of frame selected Stokes-I images (best out of 64 images) and filtergram pairs of left- and right-hand circular polarized light, which are summed as long integers in two memory buffers of the data acquisition computer. The Stokes-I/V image is the average of 256 individual observations.

5.3 Data Reduction

The details of data processing have been discussed in Chapter 2. Only a simple review of imaging processing methods involved is given here.

5.3.1 Data Preprocessing

All data has been corrected for dark and flat-field frames. The instruments on the 25 cm telescope use a modified version of the Kuhn-Lin algorithm (Kuhn et al. 1991), which uses a set of nine original data frames to compute the flat-field frame. The data were taken at or near disk center with displacements of $5''$ and $50''$ in all four hemispheric directions. The Kuhn-Lin flat-field algorithm has been fully integrated in the data acquisition and is part of the daily observing routines at BBSO. The 65 cm telescope has not been integrated into the data acquisition system, yet. Therefore, the flat-field frames for the $H\alpha$ filtergrams and continuum speckle images are averages of 20 and 100 images, respectively, obtained near disk center while moving the telescope fast in both the declination and azimuthal axes.

5.3.2 Image Reconstruction

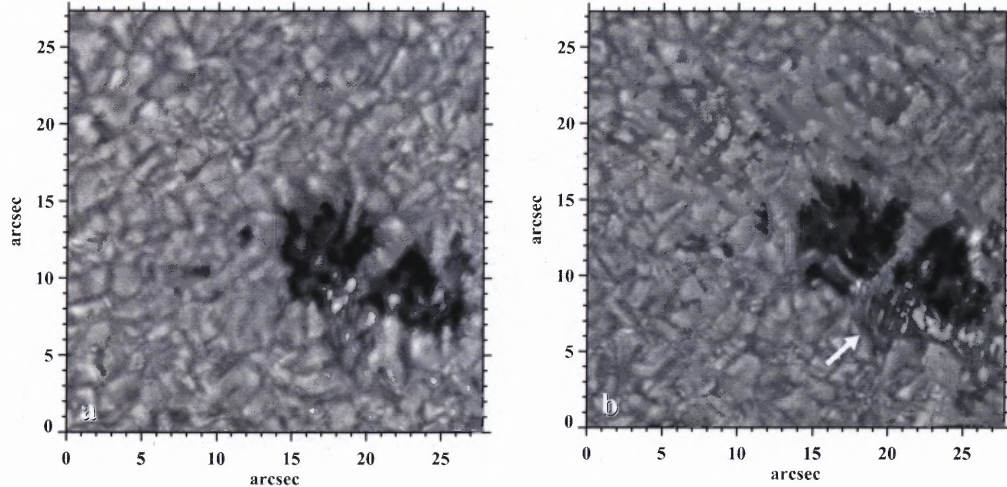


Figure 5.2 Speckle reconstructed continuum images at 5200 \AA showing two pores at the central part of active region NOAA 9539 on 2001 July 15 at (a) 19:58 UT and (b) 20:32 UT, respectively. At 20:32 UT, an approximately $5'' \times 5''$ penumbral region, which is indicated with an arrow in (b), has formed at the edge of the light-bridge separating the two pores. The arrow indicates the forming penumbra region. The FOV is about $28'' \times 28''$.

In order to obtain high-spatial resolution images, speckle-masking reconstruction technique was used to process the 5200 \AA continuum images. For each set of spectrograms, the dark current and flat-field correction were applied first. Then a median filter was used to eliminate the remnants of dust particles that were still present in the spectrograms. Since the speckle imaging technique is strictly valid only for the isoplanatic patch, the speckle image sequence was divided into stacks of 64×64 pixel images. The image with the highest rms-contrast was selected in order to correct the image stacks for image motion which is caused primarily by solar rotation and differential image motion, which is mainly caused by the atmospheric disturbances, by means of a cross-correlation analysis. The FOV of the stacked images was $4.9'' \times 4.9''$ and the total number of partially overlapping stacks was $13 \times 13 = 169$. The Fried-parameter r_0 was derived from a power spectrum analysis of the $169 \times 100 \approx 17000$ stacked images using the spectral ratio technique von der Luehe (1984). Once the Fried-parameter is at hand, the amplitude of the objects Fourier

transform was obtained by the classical method of Labeyrie (1970) and the phases of the object's Fourier transform is derived from the speckle masking bi-spectrum (Weigelt 1977; Weigelt & Wirtzner 1983; Lohmann et al. 1983). A further enhancement of the image quality originates from the application of a sensitive noise filter (de Boer 1996). Finally, back-transform of the modulus and phases of the object's Fourier transform yields a mosaic of the 169 partially overlapping, reconstructed images, which are carefully aligned before putting them together. Figure 5.2 depicts two speckle reconstructed continuum images obtained on 2001 July 15 at 19:58 UT and 20:32 UT, which show the formation of penumbral structures at the southern end of a light-bridge separating two pores. The FOV of the final reconstructed images is $27.9'' \times 27.4''$.

5.3.3 Calibration of the Line-of-Sight Magnetograms

Various calibration methods of the BBSO magnetograph system were described in Varsik (1995). Even though the optical setup of the magnetograph has significantly changed (Spirock & et al. 2001), the general principles still apply. A full disk magnetogram obtained with the spectro-magnetograph at the vacuum telescope at the Kitt Peak National Observatory (KPNO) (Jones et al. 1992) was used to calibrate the degree of polarization ρ of the BBSO magnetograms in terms of the magnetic flux density B . A discussion of the different Zeeman sensitive lines, Ca I 6103 Å at BBSO and Fe I 8688 Å at KPNO, is also given by Varsik (1995). Since no KPNO observations were available on 2001 July 15, the full disk magnetogram of the following day recorded between 16:05 UT and 17:00 UT was

Table 5.2 Local Correlation Tracking

Wavelength	Grid Spacing	Window Size	FWHM	Velocity Cut-Off	Average Velocity	Maximum Velocity
Continuum 5200 Å	0.91''	2.5''	2''	4.0 kms ⁻¹	0.19 kms ⁻¹	0.68 kms ⁻¹
H α 6562.8 Å	4.0''	10''	8''	10.0 kms ⁻¹	0.26 kms ⁻¹	1.23 kms ⁻¹
H α 6562.8 + 0.6 Å	3.0''	10''	8''	10.0 kms ⁻¹	0.29 kms ⁻¹	0.80 kms ⁻¹
H α 6562.8 - 0.6 Å	3.0''	10''	8''	10.0 kms ⁻¹	0.41 kms ⁻¹	1.53 kms ⁻¹

used. A BBSO magnetogram obtained at 16:36 UT of 2001 July 16 was selected because it had the highest contrast signal from 18 magnetograms of NOAA 9539 taken during the aforementioned time period. Note, that even though the calibration data was taken a day after the observations, the calibration is still reliable, since the optical set-up had not been changed and the bandpass of the Lyot-filter had been adapted in order to compensate for the velocity component of the solar differential rotation. The BBSO magnetogram was re-sampled to match the image scale of $1.14'' \text{ pixel}^{-1}$ of the full disk magnetogram and both images were carefully aligned with sub-pixel accuracy. Figure 5.3 shows the scatter plot of the KPNO magnetic flux density B as a function of the BBSO degree of polarization ρ measured in percent. The straight line was obtained by minimizing the χ^2 error statistic of the linear model $B = c_0 + c_1\rho$. The model coefficients are $c_0 = -12.25 \pm 0.0014$ and $c_1 = 200.39 \pm 0.31$, which are given with the respective 1σ uncertainty estimates, i. e., one percent of polarization measured with the BBSO magnetograph system corresponds to about 200 G. Magnetograph saturation becomes apparent in Figure 5.3 for the BBSO measurements when ρ exceeds 5.0, which corresponds to $B \approx 1000$ G. Note that both instruments measure the magnetic flux or the mean magnetic flux density, i. e., they do not consider the filling factor of magnetic elements. The magnetic sensitivity of both the KPNO and BBSO magnetograms is about 5 G.

5.3.4 Local Correlation Tracking

Four data sets listed in Table 5.2 were used to study the photospheric and chromospheric horizontal proper motions. All images of the time sequences were registered. In order to remove atmospheric distortions present in all images, including the speckle reconstructed continuum images, a destretching algorithm was applied to the time sequences. A sliding average over five images, including the image being processed and the two images before and after the current respectively, was used, to up-date the current reference image. Finally, a sub-sonic filter was applied to the time sequences with cut-off velocities given in

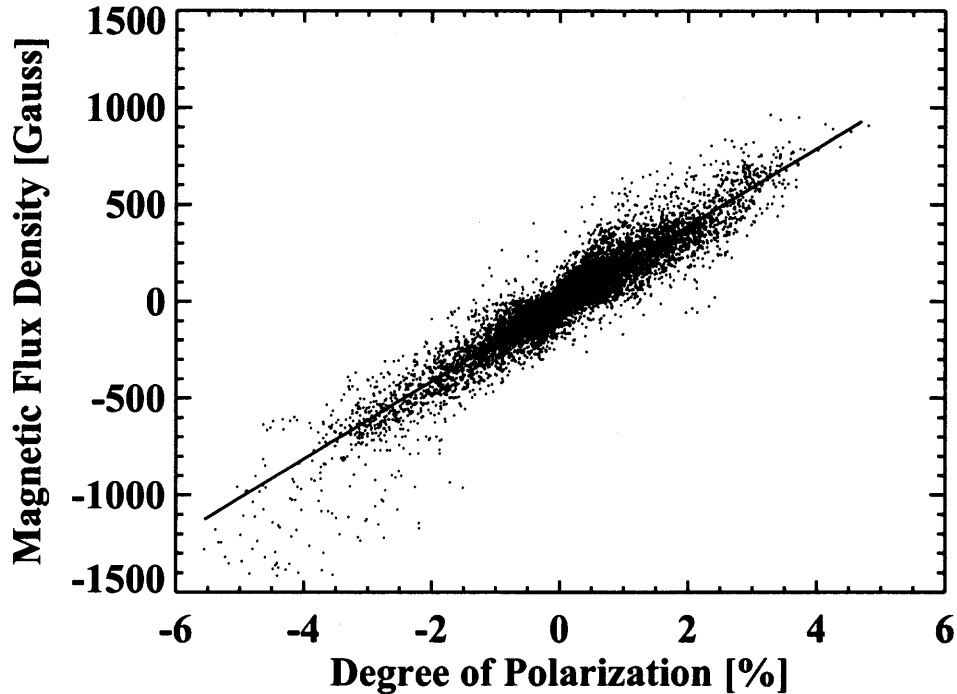


Figure 5.3 Scatter plot of magnetic flux density B of the KPNO magnetogram as function of the degree of polarization ρ of the BBSO magnetogram.

Table 5.2. Various time-lapse movies, which include contour plots of the magnetic field evolution, were then used to study the proper motions of photospheric and chromospheric fine-structures and the associated flow fields of the photosphere and chromosphere.

In order to obtain a more quantitative measure of these flow fields, the Local Correlation Tracking (LCT) technique was applied to the time sequences. The input parameters for LCT such as the grid size, the sampling window size, and the FWHM of the Gaussian sampling window are given in Table 5.2. The most important parameter is the FWHM of the Gaussian sampling window, which sets an upper limit for features that can be tracked. The standard deviation and the maximum of the velocity are also presented in Table 5.2. Note that the values are average values, i. e., the time variable effects from features with life times much less than the overall duration of the time sequences are considerably suppressed.

Originally, LCT was developed to study photospheric flow fields (November & Simon 1988). It can also be applied to chromospheric proper motions (e. g., Chae et al. 2000). However, interpreting chromospheric flow fields derived with LCT is not straightforward, since the intensity structure of $H\alpha$ line wing images is strongly influenced by Doppler shifts (Yi & Molowny-Horas 1995). The Doppler shifts in the $H\alpha$ line wing images gives rise to fluctuations of the contrast and the LCT algorithm will then interpret these fluctuations as moving features in the $H\alpha$ line wing images. One should bear this cross-talk effect in mind in interpreting the flow maps of $H\alpha$ line images. In this study, an LCT implementation based on the algorithms by November & Simon (1988) was used. The implementation was originally written as ANA/C code and has been ported to C-programs, which can be compiled as Dynamically Linked Modules (DLMs) and interfaced with the Interactive Data Language (IDL).

5.4 Results

Active region NOAA 9539 first appeared on 2001 July 12 as a β -region. Once emerged, it showed some minor activity. On July 14, the area and number of spots of this region grew significantly and it produced several C-class events. The magnetic configuration changed from β to $\beta\gamma$. From July 14 to July 17, NOAA 9539 showed moderate activity and produced several M-class and C-class events. On July 18, it decayed quickly to an α -region and remained quiet until it disappeared. At the time it rotated behind the solar limb on July 20, it had decayed to a simple α -region. It reappeared on July 31 as an α -region and finally disappeared on August 3. On 2001 July 15, NOAA 9539 was located $241''$ east and $328''$ south of the solar disk center, which corresponds to a position angle of 25 degree. Time sequence of magnetograms revealed that this region in that day possessed many small-scale magnetic fields with complex configurations such as mixed polarity, flux emergence, and flux cancellation regions. In Figure 5.4 a schematic sketch of the region studied in this chapter, which is the central part of NOAA 9539, is presented. All the features mentioned

in the subsequent part are named accordingly. The light-colored region in Figure 5.4 is corresponding to the region of the speckle reconstructed white-light images. The following discussion is focused on the evolution of the two pores, F_1 and F_2 , and associated photospheric chromospheric dynamics.

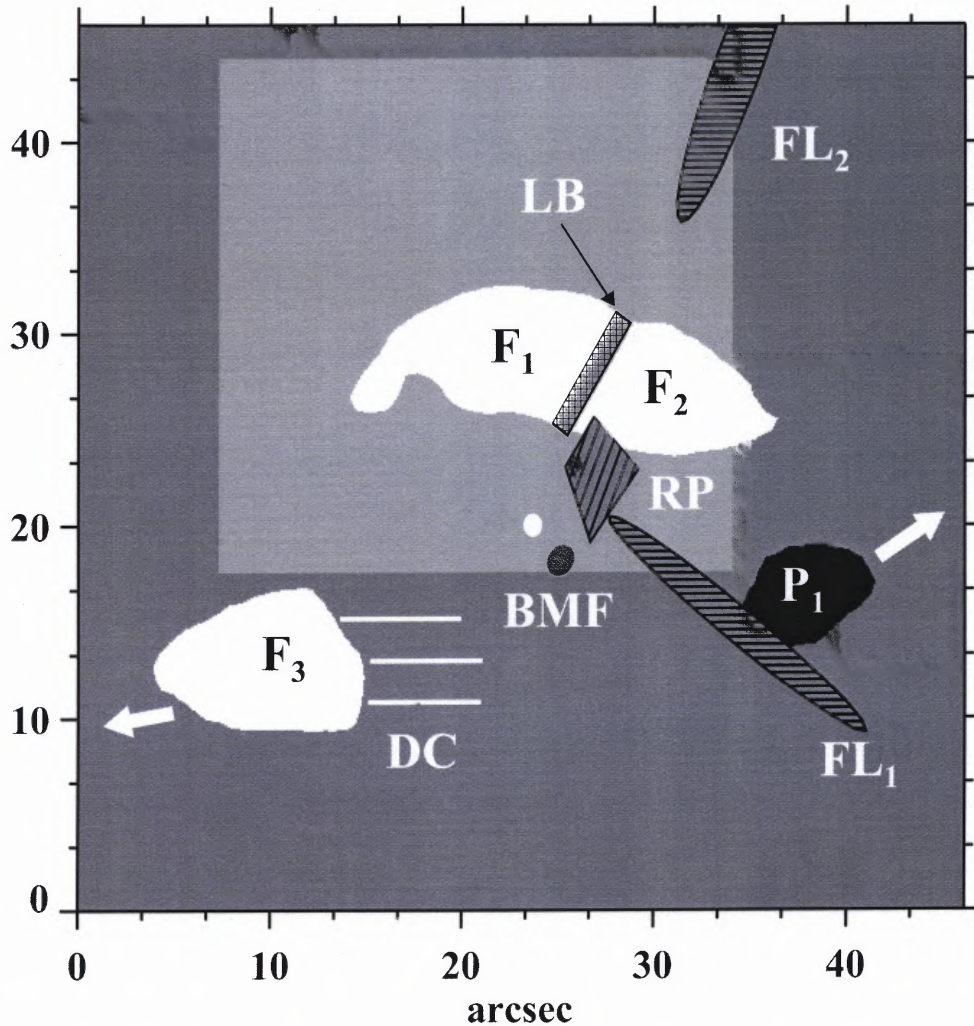


Figure 5.4 Schematic sketch of the emerging flux region within active region NOAA 9539 (LB: light-bridge, FL: filament, RP: rudimentary penumbra, DC: dark channel, BMF: bipolar magnetic feature). The light grey area corresponds to the region of interest.

5.4.1 Magnetic Field Evolution

NOAA 9539 was a sizable active region spanning about $250''$ in east-west direction and about $100''$ in north-south direction. The magnetic configuration of NOAA 9539 followed Hale's law. It was located in the southern hemisphere and comprised of a single large leading sunspot of negative polarity and several smaller trailing sunspots and pores of positive polarity. On 2001 July 15, flux emergence was still continuing in the central part of NOAA 9536, where an emerging bipolar region produced a complex magnetic field configuration. The region of interest are two pores separated by a light-bridge. The region of interest, i. e., the region corresponding to the area covered by the speckle reconstructed images, is indicated by a box in the magnetogram depicted in Figure 5.5. In this figure the relative position of the active region on the solar disk to the disk center is also shown.

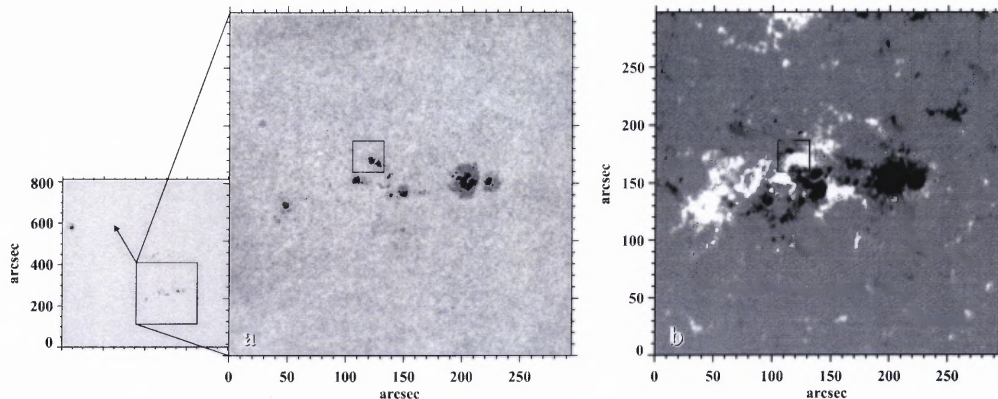


Figure 5.5 (a) Ca I 6103 Å line wing filtergram and (b) Line-of-sight magnetogram of NOAA 9539 observed with the Digital Vector Magnetograph at BBSO on 2001 July 15 at 21:03 UT. In the small leading image the relative position of the region shown in (a) and (b) to the disk center are displayed by the black box. The end of the arrow indicates the center of the solar disk. The black boxes in (a) and (b) indicates the region of interest, which corresponds to the location of the speckle reconstructed continuum images.

Even though the granular pattern and fine-structure inside the light-bridge (LB) is changing constantly—some of the smallest bright points are part of the light-bridge—the overall appearance of the light-bridge is very stable. The east-most pore F_1 is of almost circular shape in the speckle reconstructed images with a diameter of about $5''$. The other

pore F_2 exhibits an irregular shape and is slightly smaller than pore F_1 , however, the largest linear extension is again about $5''$. Both pores (F_1 and F_2) are filled with many umbral dots, some of which formed chains outlining well defined segments (umbral cores) within the pores. This indicates that some of the coalescing flux tubes retain their individual identities even after forming a sunspot or pore. As can be seen in the speckle reconstructed continuum images in Figure 5.2, the umbral dots are well resolved with the speckle reconstruction method. The size of the umbral dots are close to the diffraction limit of the 65 cm telescope, which is about $0.17''$ at 5200 \AA or about 120 km on the solar surface. Even though the convective energy transport is strongly inhibited by the predominantly vertical magnetic field lines in pores, the dynamics of the umbral dots provide some evidence of residual convective activity inside the pores.

The borders of the pores were not well defined, instead they showed cloud-like or diffuse borders, which were reported by Denker (1998) and which are indications of the onset of penumbra formation. Indeed, a penumbral segment (RP) is forming near the southern end of the light-bridge around 20:30 UT. Figure 5.2 shows speckle reconstructed images of the region of interest before and after the penumbra had been formed at 19:58 UT and 20:32 UT, respectively. In the later continuum image (Figure 5.2(b)), the penumbral segment is clearly discernible. However, it should be noted that a clear distinction of the point in time when the rudimentary penumbra was formed is difficult, since elongated, filament-like structures could be seen in most images of the observing sequence. Nonetheless, the time interval to form a well distinguished penumbral segment was about 20 min to 30 min, which is in agreement with other observations (e. g., Leka & Skumanich 1998). The rudimentary penumbra is an indication of convective interchange, which carries energy from the external plasma across the magnetopause. This happens at a location where the radiative blocking by the magnetic field is already weakened and plasma carried by convection penetrates the vertical fields of the pores as a plasma sheet, namely the light-bridge separating the two pores F_1 and F_2 . This rapid evolution is not surprising, since the two pores

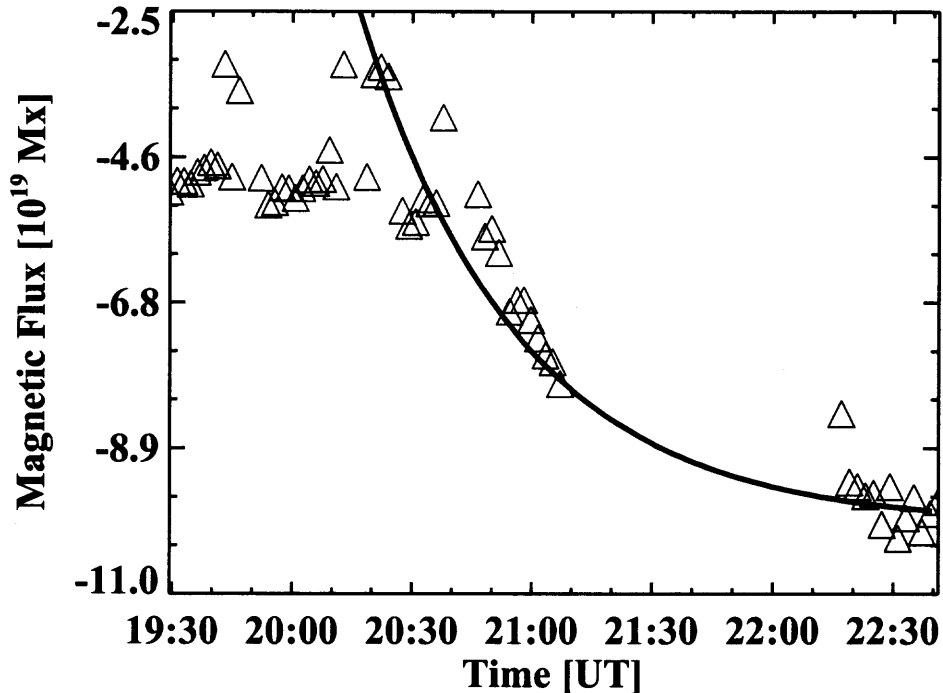


Figure 5.6 Temporal evolution of the magnetic flux of the dominant flux in the emerging bipolar magnetic feature. The solid line represents an exponential fit of a rise-time of 40 minutes approximately. The position angle of the active region was considered in the calculation.

are sufficiently large and carry enough magnetic flux to expect penumbra formation (Bray & Loughhead 1964). When the magnetic flux Φ in a pore increases, the magnetic field lines fan out and their inclination angle θ with respect to the normal to the solar surface also increases at the edges. Once the angle of inclination reaches a critical angle $\theta > \theta_c$, the penumbra formation sets in (see Rucklidge et al. 1995).

However, Rucklidge et al. (1995)'s simplified model assumes the flux tube is isolated. In the present study, the environment in which the rudimentary penumbra is formed plays a critical role. The penumbra forms in a region of continuously emerging flux (this can be seen in the magnetogram movie). The feature most closely related to the penumbra formation is an emerging bipolar magnetic feature (Shown in Figure 5.4 as BMF), which originates in a C-shaped region of positive magnetic polarity. Figure 5.6 shows the tem-

poral evolution of the magnetic flux of this emerging bipolar feature from 19:30 UT to 23:40 UT. The magnetic flux shown in this figure has been corrected for the effect of the position angle of 25 degree. Since the area of this feature is only about $5'' \times 5''$, the variation of the position angle within this area can be omitted. The gap in the figure is the time period in which observation data were missing. Assuming an exponential growth for the negative magnetic flux, a rise-time of 40 minutes was obtained approximately for the exponential fit represented by the solid line in Figure 5.6. It should be pointed out that the exponential fit is not the only choice. Other fit curves were also tried but the rise-time of the magnetic flux did not change significantly. Because the maximum magnetic field of this emerging bipolar feature is only about 400 Gauss, the saturation of the magnetograms of the DVMG at 1000 Gauss will not affect the accuracy of this figure. In the course of the flux emergence, the opposite polarity features move apart and the positive magnetic feature undergoes ceaseless cancelation with surrounding small-scale magnetic elements. The dominant feature for the penumbra formation is the negative polarity element and the penumbral filaments point directly towards this magnetic element.

Typically, penumbral fields prefer to form on the side of the pore away from the active flux emergence area or near neutral lines (Bray & Loughhead 1964). However, the presence of sunspots, or in this case an emerging bipolar feature, might be responsible for the observed asymmetry. In any case, the tips of the penumbral filaments point towards a magnetic inversion line. The emerging bipolar feature is not the only sign of active flux emergence. Several magnetic knots of negative polarity are evolving north-east of the pores. They are present throughout the whole reconstructed observing sequence (≈ 75 min) but dissolve for short time periods (≈ 5 min) into conglomerates of filigree and crinkles. At a distance of $20''$ south-east of the region of interest is another active flux emergence region. Two pores of positive polarity still visible at 16:30 UT merge into a single sunspot F₃ by 18:00 UT. The leading portion of this activity complex exhibits several dark and elongated ($\approx 10''$) features (DC) embedded in the surrounding granular fields. These dark

elongated features have been interpreted as emerging flux loops on the verge of penetrating the photosphere (Strous et al. 1996; Denker & Wang 1998). Both the magnetic knots north-east and the dark elongated features south-east of the region of interest seem not to be involved in the process of penumbra formation. South-west of the region of interest is another patch of negative flux emergence P_1 , which basically consists of a chain of magnetic knots and small pores with strong proper motions in north-west direction. All three major flux emergence regions (F_1/F_2 , F_3 , and P_1) move away from each other, with the strongest divergence 1 km/s in east-west direction parallel to the solar rotation. The important flow patterns with respect to F_1/F_2 are indicated by arrows in Figure 5.4.

5.4.2 Ellerman Bombs

The formation of a rudimentary penumbra was associated with the sudden appearance of several Ellerman Bombs (EBs) in the neighborhood of the tips of the penumbral filaments. The EBs were first discernible at 20:14 UT in the red line wing $H\alpha$ filtergrams. Figure 5.7 shows four panels illustrating the rapid appearance of the bombs and a small filament (FL_1), which are both associated with the penumbra formation. Two EBs were clearly visible during the time period from 20:14 UT to 20:37 UT. At 20:24 UT, a filament began to form with one of its foot-points rooted near the southern end of the light-bridge, in the vicinity of the penumbral filaments and the bombs. The evolution of the EBs took place in a very localized area of about $5'' \times 5''$. This region coincided with the magnetic inversion line separating a C-shaped area of positive flux from a newly emerging magnetic bipole. In many cases, the EBs had bright abnormal granules or filigree as their photospheric counterpart. Since the EBs in the observation were located at the very edge of the region of interest, an identification with distinct bright abnormal granules or filigree is impossible but several potential candidates near or within the site of the penumbra formation were found. Many EBs move along intergranular lanes with relative velocities of 1 km/s to 2 km/s (e. g., Denker et al. 1995), whereas in this case, the EBs remained extremely stationary despite the frag-

mentation of one of them. Nindos & Zirin (1998) find that about one third of Ellerman Bombs correspond well to moving magnetic features and the remaining two thirds are not related to enhanced magnetic features. The conglomerate of EBs in the present observations developed in the neighborhood of the rudimentary penumbra and in the vicinity of an emerging magnetic flux element.

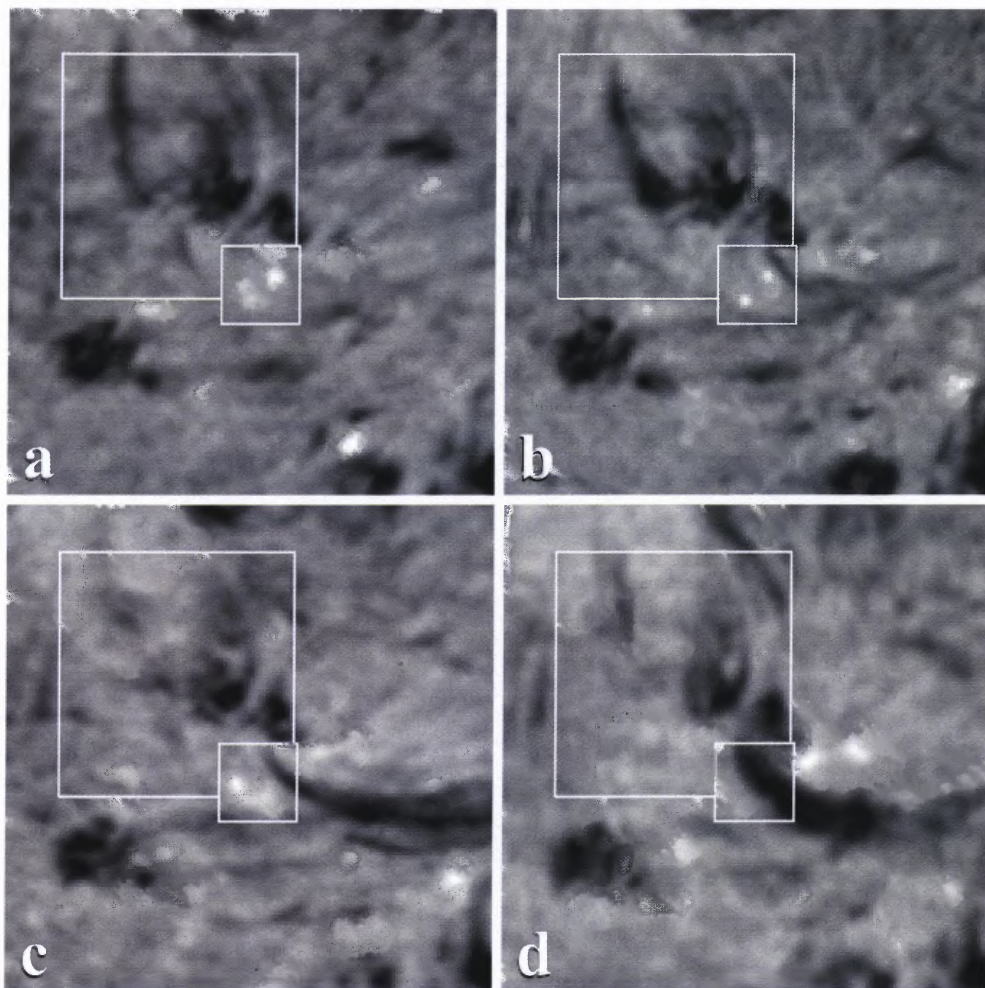


Figure 5.7 Time sequence of $H\alpha$ red line wing ($6562.8 + 0.6 \text{ \AA}$) filtergrams depicting the temporal evolution of Ellerman Bombs, which were located near the tips of the newly formed penumbral filaments. Detailed view of Ellerman Bombs and filament activation at (a) 20:14 UT, (b) 20:25 UT, (c) 20:35 UT, and (d) 20:45 UT, respectively. The FOV is about $55'' \times 55''$. The big box in (a) indicates the region observed in white-light. The evolution of three Ellerman Bombs are shown in the region indicated by the small boxes in all the sub-images.

During the rapid activation of the filament, some of the cool filament material

blocked the view towards the emission from the EBs, so it is difficult to judge the evolution of the bombs after 20:37 UT. Some residual $H\alpha$ brightenings were still visible after 20:45 UT, when the filament was already in the decaying phase. Since one of the EBs split into several smaller brightenings, it becomes even more difficult to derive proper light curves for the individual Ellerman Bomb. Figure 5.8 is an attempt to visualize the rapid appearance of the Ellerman Bombs. Figure 5.8 (a) shows two obvious EBs at the beginning, which seemed to have gone at around 20:29 UT, while the background level of the region was still fairly high. After several minutes in the same region another one appeared again. Due to this lack of a persistent structure of the EBs, the surface brightness curve of the region containing the EBs in Figure 5.8 was also depicted (b). The curve is basically an intensity flux related to the temporal evolution of the conglomerate of Ellerman Bombs. Since the $H\alpha$ data was not corrected for the atmospheric point spread function, the intensity values depicted in the light curves in Figure 5.8 should be considered as lower boundaries. The corrected values can be much higher. The life-time of the Ellerman Bombs is about 20 min to 30 min, which is well in the range of other reported values (e. g., Nindos & Zirin 1998; Qiu et al. 2000).

5.4.3 $H\alpha$ Filaments

The formation of the rudimentary penumbra is closely related to chromospheric activity in form of two short-lived filaments (FL_1 and FL_2). At 20:10 UT, a filament (FL_2) appears north of the light-bridge. The axes of the light-bridge and filament are co-aligned in north-south direction. One of the filament foot points is located just north of the pores. The filament fades away at 21:30 UT, and reappears shortly after for another 10 min to 15 min. The rapid evolution of this filament triggers the activation of the second filament on the southern side of the two pore. The length of this filament (FL_1) is about $50''$ and one of the foot-points is located in the vicinity of the newly formed penumbral segment. This filament is oriented in east-west direction. The Ellerman Bombs discussed in the previous section are precursors of the filament activation and first indications of the filament formation can

be seen at 20:24 UT. The filament reaches its maximum evolution in the red wing at 20:39 and shortly thereafter at 20:42 UT in the blue wing. Once the filament reaches its maximum, it breaks apart into two distinct parts seen in the $H\alpha$ red line wing images, which now connect to different small-scale magnetic features. In Figure 5.9 the $H\alpha$ line wing images superimposed with magnetic field contour lines and the corresponding dopplergram were shown when the filament reaches its maximum. The separation is accompanied with a twisting motion along the filament axis, which can be seen as a distinct velocity pattern in the time-series movie of the $H\alpha$ dopplergrams provided with this chapter. Figure 5.10 shows four images from the movie. The $H\alpha$ dopplergrams are encoded according to the astronomical convention, where positive line-of-sight velocities correspond to red-shifted spectral line profiles and negative velocities to blue-shifted line profiles. One should notice the severe limitations of the dopplergrams derived in such a way: First the $H\alpha$ line wing images were not taken at the exactly same time; Second the $H\alpha$ data was not corrected for the atmospheric point spread function. Nonetheless, it provides us some basic understanding of the line-of-sight speed field. Finally, the filament has faded away by 21:20 UT.

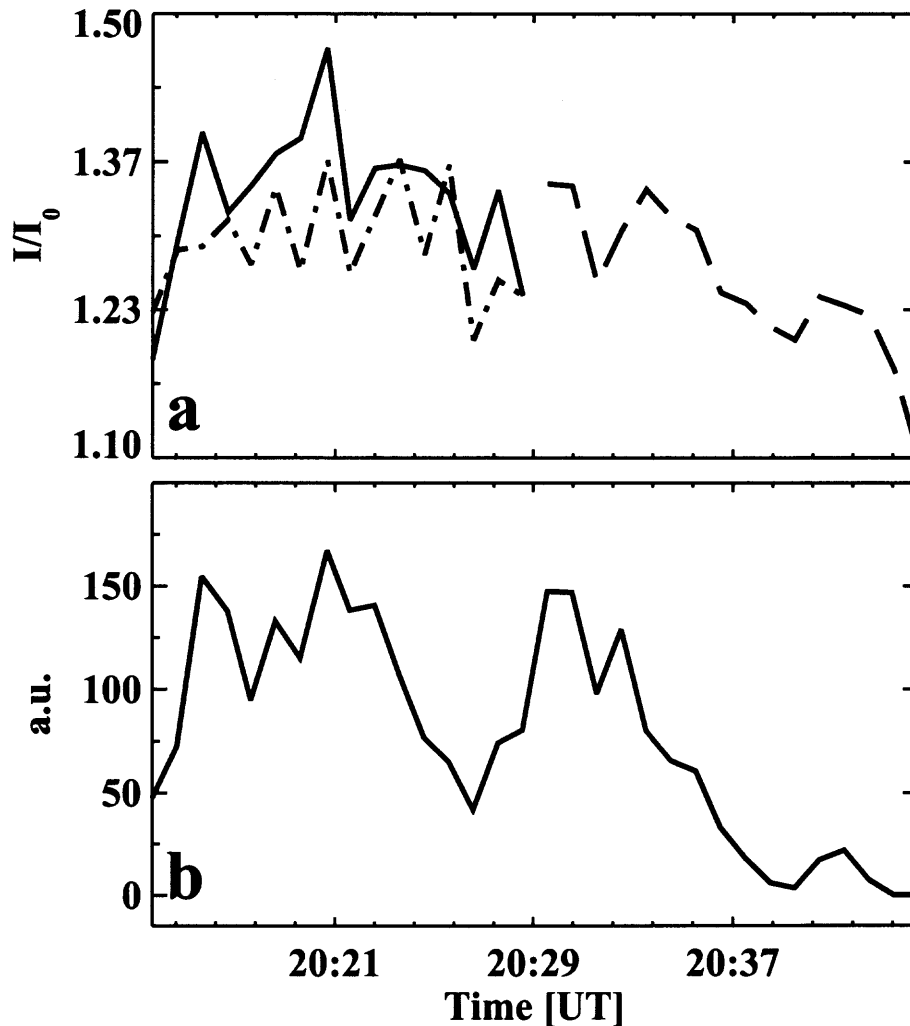


Figure 5.8 Temporal evolution of (a) the peak intensity of three EBs (See Figure 5.7 for selected time sequence images), and (b) the curve of total surface brightness of the region that contains the EBs. At the beginning there were two EBs which are corresponding to the two leading curves in (a). They disappeared during the evolution. Later another one emerged at the same region which is described by the following curve in (a). It is hard to tell if it was recurrence of the older ones. The dip in (b) is caused by the disappearance of the EBs.

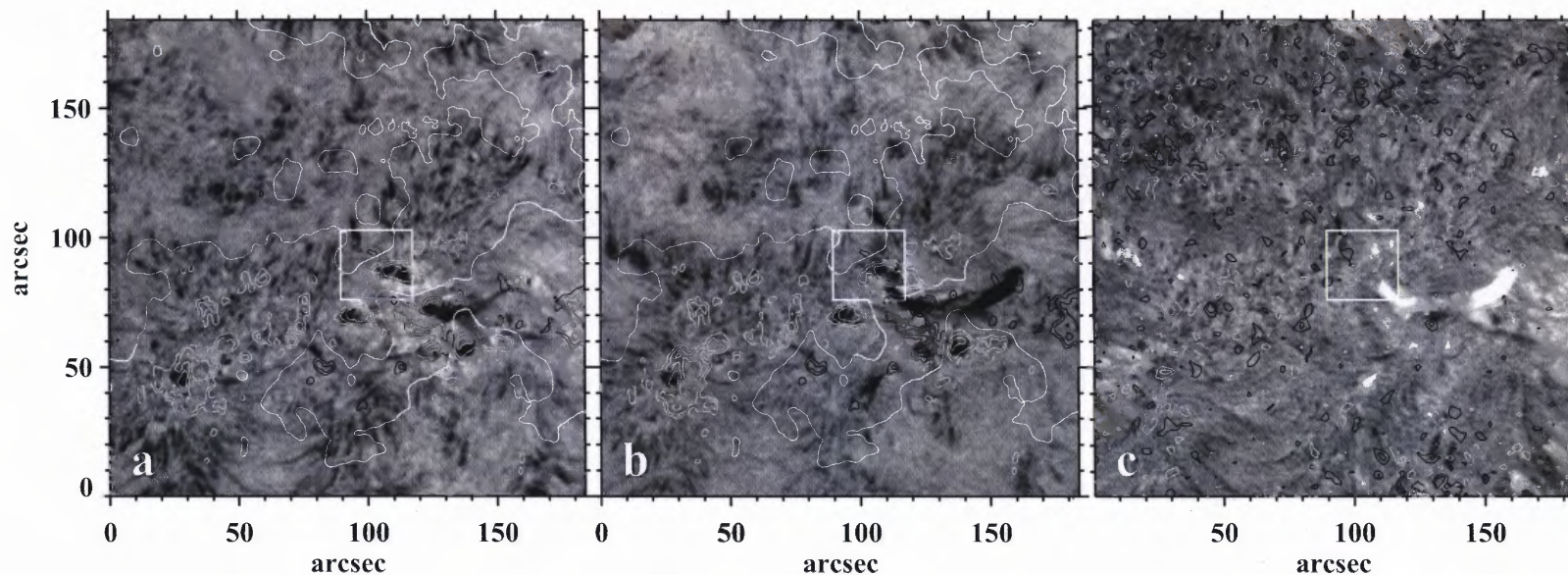


Figure 5.9 $H\alpha$ off-band images taken on 2001 July 15 at 20:43 UT. (a) Blue line wing filtergram at $H\alpha - 0.6 \text{ \AA}$, (b) red line wing filtergram at $H\alpha + 0.6 \text{ \AA}$, and (c) the corresponding $H\alpha$ dopplergram. The $H\alpha$ off-band filtergrams are shown with superimposed contour lines of a co-temporal magnetogram (Light gray: positive magnetic fields; Dark gray: negative fields; White: neutral line). The contour lines are drawn at the $\pm 300 \text{ G}$, $\pm 500 \text{ G}$ and $\pm 800 \text{ G}$ levels, respectively. The contour lines superimposed on top of the $H\alpha$ dopplergrams correspond to a divergence map derived from the average horizontal proper motions that are present in the time sequence of $H\alpha$ dopplergrams. The white box in each panel indicates the region of interest.

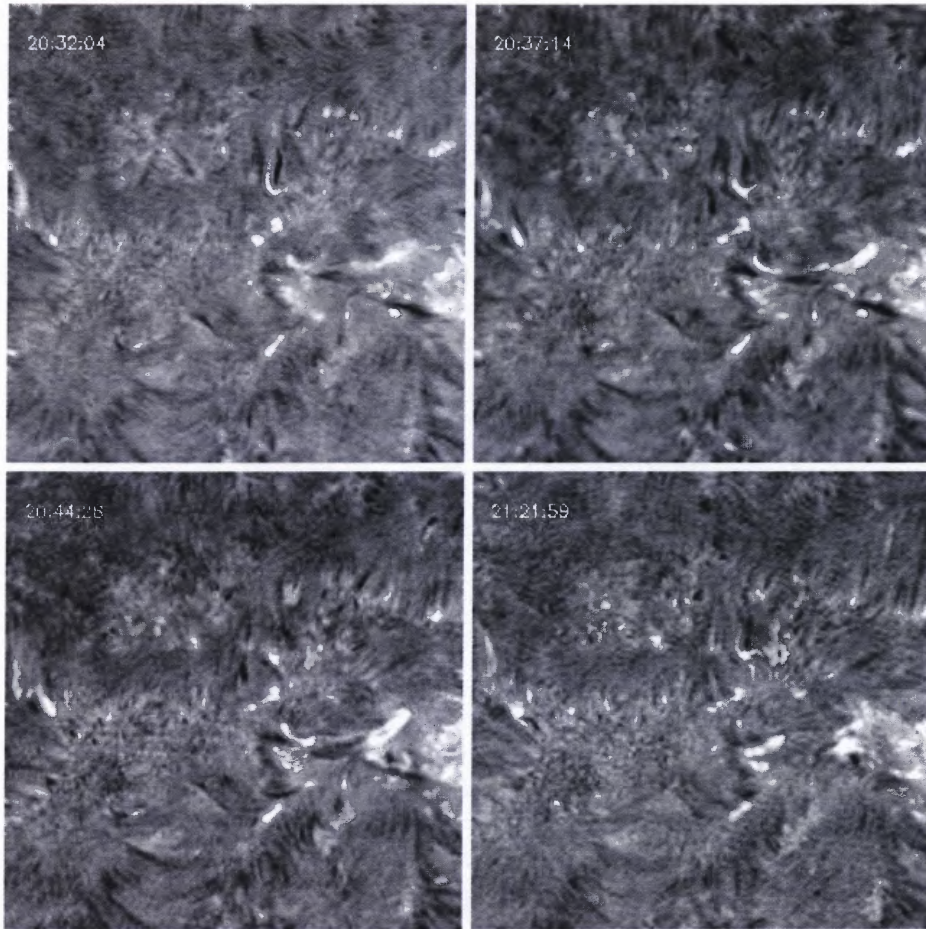


Figure 5.10 The twisting motion of the filament (F1) when it was falling down to the surface of the Sun is shown in these images. Notice the variation of the intensity of the Doppler signal from the filament.

5.4.4 Photospheric and Chromospheric Flow Fields

In Figure 5.11 the flow map and the divergence map of the horizontal proper motion of the white light images were shown. In the previous studies (e. g., Wang & Zirin 1992; Sobotka et al. 1995) inward flows near sunspots and pores were found. But in the observation the granular flows around the two pores are generally moving outward (Figure 5.11). This might be an indication of the start of the inclination of the magnetic fields around the pores.

In the rudimentary penumbral formation region (RP in Figure 5.4), the flows conform to the result of Wang & Zirin (1992). In the newly formed penumbrae, the flow near

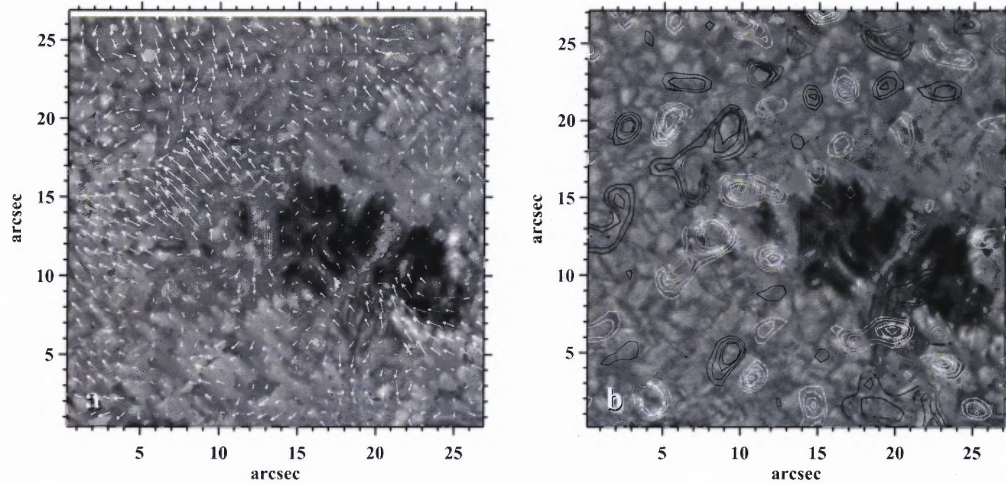


Figure 5.11 Average horizontal velocity derived from a time sequence of speckle reconstructed continuum images. (a) Velocity field and (b) corresponding divergence map. The background image was taken at 20:32 UT.

the pores was moving towards the lower pore at a speed of 0.30 km/s; while in outer (with regard to the pores) part of penumbrae the direction of the flow is away from the pore at a speed of about 0.33 km/s. There are no noticeable flows inside the light-bridge.

The horizontal flow maps and divergence maps of the $H\alpha$ line center images in Figure 5.12 were shown. Although the cross-talk effect due to the line shifts still exists in $H\alpha$ center line images, it has been indicated that it can be neglected in $H\alpha$ center line observations as long as the line shifts are $\leq 0.1 \text{ \AA}$ or equivalently $\leq 4.6 \text{ km s}^{-1}$ (e. g., Yi & Molowny-Horas 1995; Chae et al. 2000). Therefore the horizontal velocities measured from images of $H\alpha$ line center in Table 5.2 are reliable. It was found that around the leading spot the flows in the superpenumbrae are inward while in the following spot the flows move outward.

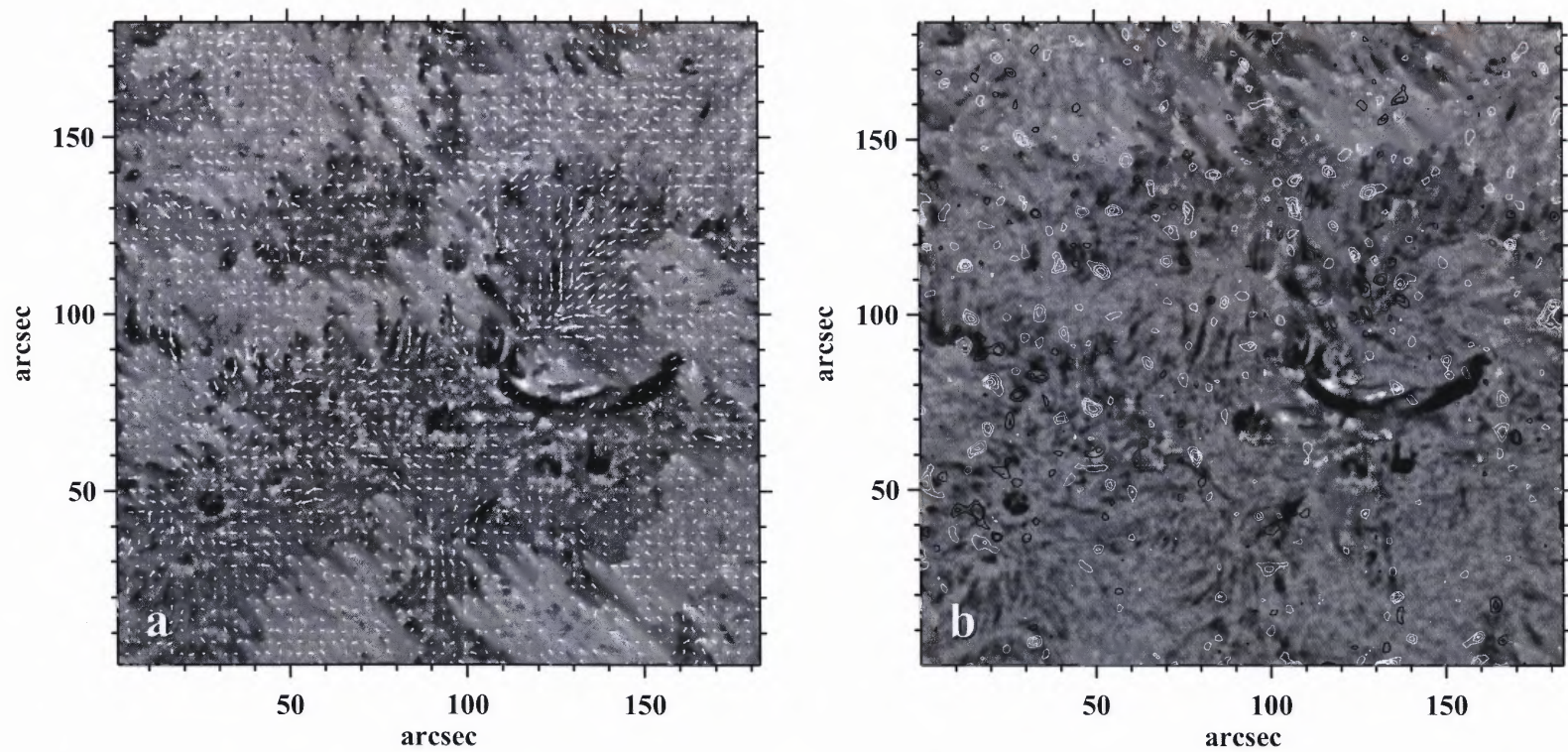


Figure 5.12 Average horizontal velocity derived from a time sequence of $H\alpha + 0.6 \text{ \AA}$ line wing filtergrams. (a) Velocity field and (b) corresponding divergence map. The background filtergram was taken at 20:43 UT.

Flow maps and divergence maps for the H α red and blue line wing images were not shown. The correlation coefficients between the two vector fields in the whole region are rather small ($< \pm 0.2$). But this does not mean that there is no cross-talk effect between intensity and line shifts. After the two flow maps are examined carefully, it is found that there are regions in which the velocities are almost opposite to each other. This clearly shows that the variation of the contrast caused by the line shifts is interpreted by LCT algorithm as a moving feature.

5.5 Summary

With multi-wavelength observations at BBSO of emerging flux in active region NOAA 9539, the formation of a rudimentary penumbra were studied and following results were found:

1. The rudimentary penumbra develops abruptly within 20 min to 30 min at a location where convective cells associated with a light-bridge already weakened the radiative blocking by the nearly vertical fields of two pores.
2. The on-set of the penumbra formation is triggered by an emerging bipolar magnetic flux element.
3. The rapid change of the magnetic field topology, from almost vertical filed lines inside the pore to inclined field lines after formation of the rudimentary penumbra, allows the condensation of cool chromospheric material and the activation of a short-lived filament.
4. A conglomerate of Ellerman Bombs appears in the vicinity of the tips of the penumbral filaments and the foot-points of the activated filament.
5. Once a penumbra appears, it will directly influence the dynamics of the photosphere and chromosphere, and possibly affect the transition region and corona as well.

The observations support the following scenario: Newly emerging flux leads to a critical point in the evolution of the two pores. Starting with the simplified model of energy transport in sunspots/pores provided by Rucklidge et al. (1995), the transition of pores to sunspots, which have a distinct filamentary penumbra, can be explained. Once magnetic flux Φ and the radii R have reached a critical value, the inclination of the magnetic field lines near the boundary of pores and granulation becomes more and more horizontal, which initiates lateral heat transport in form of filamentary convection. Interestingly enough, this happens at the exact location, where the radiative blocking by the almost vertical fields inside the pores is already weakened by a convective plasma sheet along a light-bridge separating the pores. The response of the chromosphere to a transition from almost vertical to more inclined fields is coronal condensation of cool material from above that forms the two filaments. Since the filaments are more prominent in the red wing of the $H\alpha$ line, it was concluded that downward moving material interacts with the newly emerging penumbral fields near the foot-points of the filament and maybe associated with the intensity enhancement in the inner line wings of $H\alpha$ in form of several Ellerman Bombs. The observations are in many respects the exact opposite to the results reported by Chae et al. (2000), where the reconnection process of a cancelling magnetic feature provokes the injection of cool plasma into a filament from below.

Two avenues remain open to extend the present study of penumbra formation. (1) Ground-based high-resolution observations of the photosphere and chromosphere could be combined with observations of the upper solar atmosphere, i. e., the transition region and corona. Data from the Transition Region and Coronal Explorer (TRACE) and the Extreme-Ultraviolet Imager onboard the Solar and Heliospheric Observatory (SoHO) has not yet been explicitly applied to the physics of penumbra formation. (2) At BBSO, a next generation of instruments that will work with the new Adaptive Optics (AO) system (Didkovsky & et al. 2003) at the 65 cm vacuum reflector is being developed. The Visible-light Imaging Magnetograph (VIM) and the Infra-Red Imaging Magnetograph (IRIM) have been

designed for high temporal, spatial, and spectral observations of active region development (Denker & et al. 2003). The expected two-dimensional data is ideally suited to gain a better comprehension in the physics related to the rapid evolution and dynamics involved in the formation of sunspot penumbrae (see e. g., Leka & Steiner 2001), which will enable us to relate these observations to current theoretical models (e. g., Schlichenmaier et al. 1998).

CHAPTER 6

STATISTICAL STUDIES OF FILAMENT DISAPPEARANCES AND CMES

After studying the surface signature of solar activity, large scale structure of solar activity will be investigated. A statistical study of filament and prominence disappearances is described in this chapter. A nearly complete set of Big Bear Solar Observatory $H\alpha$ full disk images observed between January 1997 and June 1999 is searched for filament and prominence disappearances. A list of 431 filament and prominence disappearance events is compiled. Comparison of these data with those from LASCO aboard SOHO is made to obtain the relationship between CMEs and filament disappearances. The results show that most filament disappearances seem to have no corresponding CME events. Even for the limb events, only 30% of filament disappearances are associated with CMEs. The possible explanations are discussed.

6.1 Introduction

Filaments are thin condensed sheets of chromospheric material located in the low corona. They are suspended above neutral lines between two opposite magnetic polarities. Their temperature and density are two orders of magnitudes smaller and greater than that of the ambient corona respectively. When observed in $H\alpha$ they appear as dark ribbons against the chromosphere. When seen above the limb, they appear bright against the dark sky and are called prominences. Some filaments and prominences end their existence by eruption.

Coronal Mass Ejections (CME) are large scale eruptions which carry a lot of mass (up to 10^{16} kg) and energy (up to 10^{25} J) away from the corona (Harrison 1994). Studies have shown that CMEs have close association with magnetic clouds which can cause geomagnetic storms near the Earth (Bothmer & Schwenn 1994).

Studies have shown that flares and filament/prominence eruptions are two principle

solar surface phenomena that may be associated with CMEs. But there is no evidence of an one-to-one correspondence between CMEs and solar surface events. Some studies indicate that filament eruptions have a closer association with CMEs than flares. So an extensive study of filament disappearances is important to clarify the relation between CMEs and filament disappearances.

In this chapter a complete list of major filament disappearances detected by BBSO from 1997 to 1999 is presented first. The list was compared against the data from LASCO. A simple statistical analysis of the relation between the filament disappearances and the CMEs is presented. Finally, the possible explanations for why the rate of correspondence between filament disappearances and CMEs is very low were given.

6.2 Observations and Results

To carry out this study, solar $H\alpha$ full disk data from Big Bear Solar Observatory (BBSO) was used to monitor the filament and prominence disappearances. BBSO started to digitally record solar full disk $H\alpha$ images from 1995. The images were recorded by a 2048×2048 Kodak 8-bit Megaplus camera with a 20-cm refractor (Singer-Link telescope). The pixel resolution of the images is 2". The cadence is 1 image per minute. Data from Feb. 1997 to Jun. 1999 was chosen. Because of the huge amount of data, at the beginning the daily images of consecutive days were compared first to roughly select possible events. Then a movie is generated using one image every 10 minutes. It is very easy to see if there are any filament disappearances during that day from the movie.

Data from LASCO which is aboard SOHO were used to see if there is a correspondent CME for every filament disappearance event found. Sometimes it is difficult to decide from the LASCO C2 and C3 movie if there is any correspondence. The CME list from LASCO site was also used.

After searching the BBSO full disk $H\alpha$ data, 431 filament/prominence disappearances events were found. Table 6.1 lists the events of the filaments longer than 250 arc sec.

Table 6.1 Part of the Filament Disappearance Data

Date	Begin	End	Position	Size	Direction	CME
98/07/15	01:05:47	18:10:46	S41E01	320	63	no
98/07/15	01:05:47	18:10:46	S31E22	508	80	no
98/07/22	14:29:45	15:52:25	N46W90	284		no
98/08/14	15:35:03/14	16:31:31/15	S45E12	264	62	no
98/08/25	14:56:56	22:44:39	S31W36	272	29	no
98/10/06	22:16:43/06	16:00:29/08	N20W26	440	-73	no
98/10/14	22:19:37/14	15:21:19/15	N23E16	308	-64	no c2 data
98/10/27	23:00:36/27	17:01:57/28	S25E12	276	70	no
98/12/23	18:41:37	23:00:27	N54W09	372	-71	no
99/01/17	17:32:14	20:21:34	N38E16	368		no
99/01/21	22:49:51/21	16:29:11/22	N56W04	484		no
99/02/03	15:42:46	23:24:05	N37E11	576		no
99/02/14	00:01:52	15:52:15	S51W12	308		no
99/02/22	17:50:38	16:00:20/23	S14E32	264		may have
99/02/22	17:51:38	16:00:20/23	N00E05	464		may have
99/02/23	16:00:20	23:34:08	N55E23	340		no
99/03/08	20:16:06/08	15:56:33/09	S44W11	424		may have
99/03/22	23:41:46/22	16:00:18/23	S38E29	252		yes
99/03/30	00:02:39	15:52:48	N72W10	488		yes
99/04/04	23:27:32/04	15:21:21/05	N36E13	252	-67	may have
98/04/17	23:48:49/17	14:59:17/18	N29E09	292	-57	yes
98/05/01	17:37:25	23:30:03	N49E54	292		yes
99/05/21	20:13:03/21	16:17:06/22	S17E16	344		no
99/05/30	23:16:18/30	14:11:30/31	S11W46	292		may have
99/06/09	14:37:09	15:03:10	S20W29	336		may have
99/06/25	18:08:22/25	01:04:28/26	N36E02	324		May have

The first column in the table gives the date when the filament first appeared. The second column gives the time when the filament was last seen before its disappearance. The third column gives the time of the first image when the filament is no longer visible. If the filament disappeared over the night gap, this time is the time of the start of the observation on the next day. In column four the center position of the filament is listed. Column five lists the initial size of the filament. The sixth column lists the direction of filament. The direction of a filament is measured as 0 degrees if it is exactly north-south orientated. The filament orientation is recorded as a positive angle if it is rotated counter-clockwise from the zero degree position. The last column lists the judgment if the filament disappearances have an associated CME.

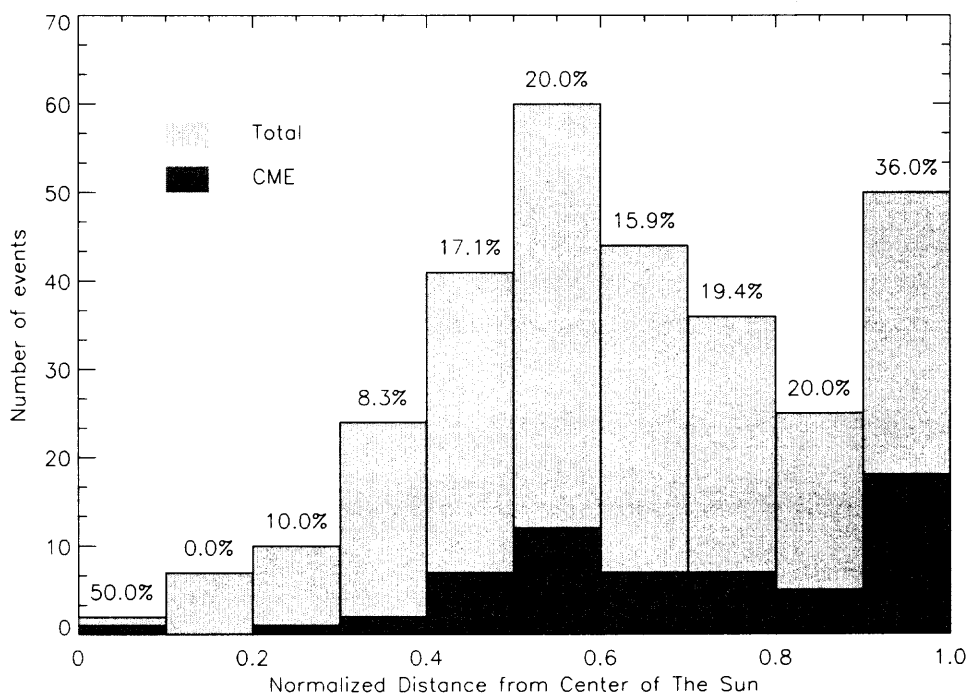


Figure 6.1 Distribution of the filament disappearances as the function of the distance from the center of the Sun.

Based on the filament disappearances in the more extended list (431 events), LASCO data was searched and see if there are CMEs associated with the filament disappearances.

The sample result is denoted in the last column of the filament disappearances list. Figure 6.1 shows the distribution of the filament disappearances as a function of distance to solar disk center. In this figure, the lighter curve shows the total number of filaments disappearances in each position bin, while darker curve shows the number of events having CME association. The percentage of the filament disappearance events which have CMEs associated is also annotated on the figure. Please note that the association of filament disappearances and CMEs is very low, ranging between 10 to 30%.

6.3 Discussion

From the Table 6.1 and Figure 6.1, it can be seen that the percentage of the filament disappearances associated with CMEs is fairly low. While some other study have indicated that the association rates between CMEs and prominence eruption are fairly high (e.g. Gopalswamy et al. 2003). There are three possible reasons. (1) A distinction between the thermal filament disappearance and the filament eruptions was not made. Even for filament eruptions, only the dynamic filament eruptions might cause CMEs (Mouradian et al. 1995). (2) It is possible that some filament disappearances on the disk might be associated with very weak halo CMEs which are difficult to detect. (3) It was noticed that some erupting filaments come back to the Sun, if they have no continuous acceleration and their speeds are lower than the escape speed of the Sun.

An example of prominence eruption without CME association is shown in Figure 6.2. This event happened on April 15, 2001. This is one of the largest eruptions ever recorded at BBSO. It is a limb event. However, there is only a very weak outflow appearing in the streamer in C2, 3 hours after the eruption, that could be barely to be classified as a CME. And the filament erupted, but most of the material fell back to the Sun.

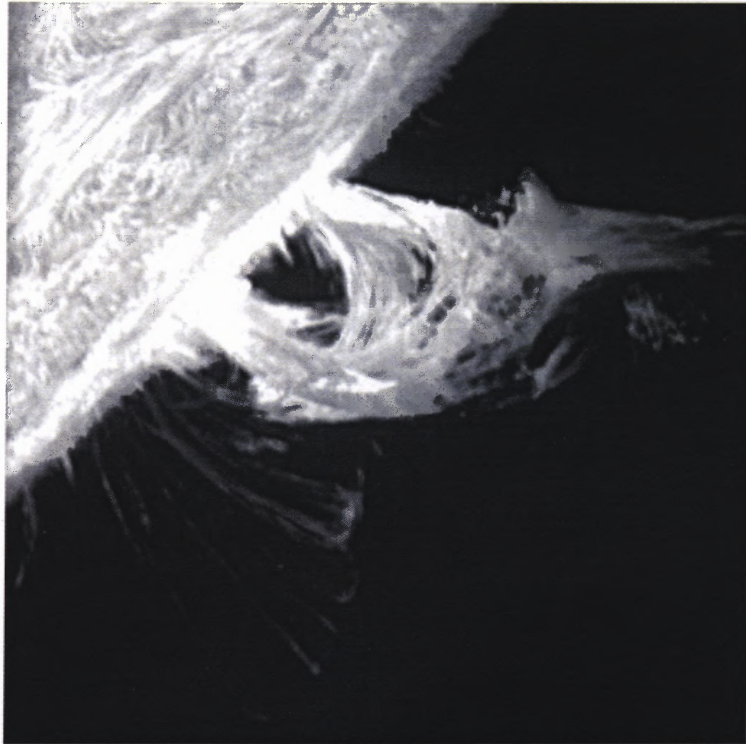


Figure 6.2 A prominence eruption observed at BBSO at 22:10UT, on April 15, 2001. The field of view is 300'' by 300'' This eruption did not have an obviously related CME.

CHAPTER 7

A HIGHLY HELICAL CME OBSERVED BY LASCO AND EIT

In this chapter, a case study of a coronal mass ejection (CME) event observed by the LASCO and EIT instruments on board the SOLar and Heliospheric Observatory (SOHO) on March 20, 2000 is presented. It was accompanied with a spectacular filament eruption and a flare. The morphological structure of this event is different from usual CMEs: it did not show the three-parts structure that typical CMEs show. The rich structure observed in this event may give us a hint of the underlying magnetic structure of the CME. The kinematic and morphological properties of this event are presented in this chapter.

7.1 Introduction

Coronal mass Ejections (CMEs) were first observed in the early 1970s and since then have been studied intensively (Gosling et al. 1974, 1991; Howard et al. 1985; Illing & Hundhausen 1983; Hundhausen 1999). With the observations of coronagraphs, a CME is identified by a discrete electron density enhancement expanding outward from the Sun. In each individual CME, a significant amount of plasma ($\sim 10^{15} - 10^{16}$ g) and magnetic energy ($\sim 10^{31} - 10^{33}$ erg) are injected into the solar wind (Gosling et al. 1974).

The CMEs play a very important role in the plasma coupling of the Sun and the Earth. It has been confirmed that there is a strong statistical correlation between CMEs and large geomagnetic storms (Gosling et al. 1991; Kahler 1992). There is also a strong statistical correlation between CMEs and interplanetary magnetic clouds (Wilson & Hildner 1984). Burlaga et al. (1981) first identified magnetic clouds and interpreted them as magnetic flux ropes (Burlaga 1988). Several recent halo CMEs (CMEs that occur near the center of the solar disk) observed by Large Angle and Spectrometric Coronagraph (LASCO) on board the SOHO satellite were followed by magnetic clouds impinging on the Earth's

magnetosphere observed by the *WIND* spacecraft at 1 AU, causing geomagnetic storms (Brueckner et al. 1998).

Observations have revealed that many CMEs have a three-part structure consisting of a bright leading edge, a dark cavity following the leading edge, and a compact bright region within the cavity. The bright region in the cavity is often interpreted to be the remnant of an erupted prominence that is associated with the CME (Illing & Hundhausen 1983). As discussed in Chapter 6, the relationship between filament eruptions and CMEs is still unknown. It is still not clear if a CME is caused by a filament eruption or vice versa.

Three-dimensional magnetic geometry of the CMEs still remains unknown. The evolutionary relationship between CMEs and interplanetary magnetic flux ropes has not been determined by direct observation. In some theoretical models the initial magnetic field underlying a CME is a helical magnetic flux rope with its legs connected to the Sun (Chen & Garren 1993; Chen 1996; Kumar & Rust 1996; Wu et al. 1997; Low 1996). As Chen (1996) indicates, the cavity magnetic field and plasma evolve into a flux rope closely resembling interplanetary magnetic clouds observed at various heliocentric distances. Results from some recent numerical simulations also show that the underlying magnetic structure of CMEs is flux ropes (Wu et al. 1999; Amari et al. 2000). But where the flux ropes come from still remains unresolved. Different explanations exist. Chen (1996) claims that the flux rope preexists and erupts either by flux emergence or other mechanism. Amari et al. (2000) proposed that the flux rope is formed by photospheric differential rotation.

Chen et al. (2000) and Chen et al. (1997) analyzed two CMEs observed on September 9, 1997 and April 13, 1997 respectively. They compared the data with the expanding flux rope model of Chen (1996) and found the model is consistent with the observations. Wood et al. (1999) discussed two CMEs observed with LASCO and EIT and also confirmed that the expanding flux rope model is consistent with the observations. Dere et al. (1999) discussed three CMEs and indicated the importance of studying the more complex three-dimensional topology of CMEs, such as the helical structure showed in many CMEs.

In this chapter, a CME of March 20, 2000 has been studied. This CME does not show an obvious three-part structure. It has a complicated structure. In Section 7.2, observation data from LASCO and EIT for this event is presented. The LASCO C2 and C3 coronagraphs have fields of view (FOV) of $2 - 6 R_{\odot}$ and $4 - 32 R_{\odot}$ (Brueckner et al. 1995). The EIT instrument observes the solar disk and its fields of view extends to $1.4 R_{\odot}$ (Delaboudiniere et al. 1995). The EIT Fe XII 195 Å ($\sim 1.5 \times 10^6$) data is used. In Section 7.3, summary and discussion are presented and the expanding flux rope model (Chen 1996) is compared with observations.

7.2 Coronal Mass Ejection of 2000 March 20

7.2.1 LASCO Data

This CME occurred on the east solar limb. In LASCO C2 images, it spanned a large region from the solar equator to far south of the limb. Running difference images from LASCO C2 coronagraph of this event are shown in Figures 7.1. The CME was first seen coming out of the occulting disk of C2 coronagraph at around 07:31 UT. At the moment the height of it was about two solar radii, R_{\odot} . At the beginning, the CME appeared as some streamers moving mainly toward the southeast at a speed of about 60 km s^{-1} .

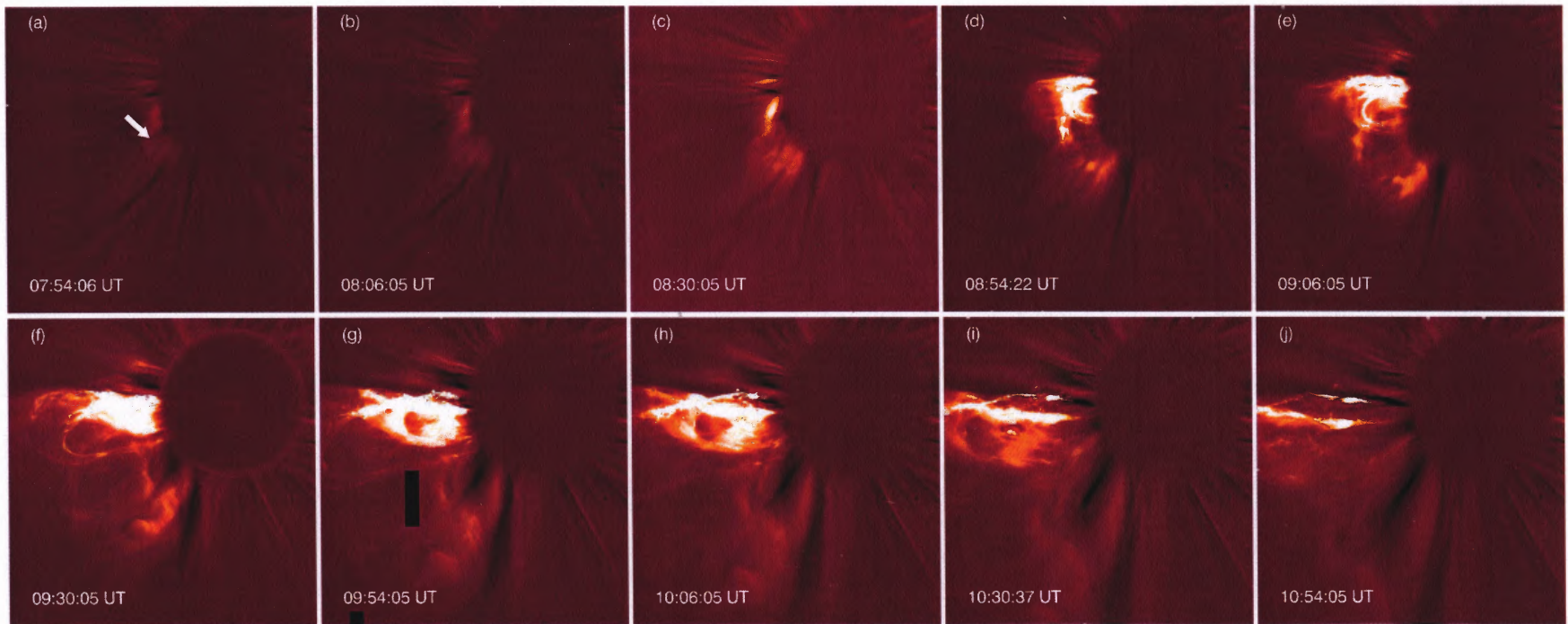


Figure 7.1 Running difference images of the March 20 CME. It shows that the CME was coming out the occult disk of C2 coronagraph at around 07:54 UT. At the beginning its speed was very low. The arrow in panel (a) indicates the arcade of loops of the CME. It is very clear from these images that this CME did not have the three-part structure that typical CMEs have. Also the images clear show that the CME consisted of three groups of loops that move in different directions.

Between 08:30:05 UT and 08:54:22 UT, the CME was accelerated abruptly. As Figure 7.1 shows, the speed of the CME increased from several tens kilometer per second to several hundred kilometer per second. The filament eruption observed by EIT also happened during this period of time. At the same time, a very bright structure that did not show in the early stage of the CME appeared in LASCO C2 images. The position of this structure corresponded to the filament eruption very well. It moved towards the east from the limb near the equator. The original streamers were accelerated as well and continued to move to the southeast at almost the same speed as the bright structure.

The particular interesting aspect of this CME is that it did not show the usual three-part structure of typical CMEs: there is no obvious bright rim, dark cavity and bright core. It seems that this CME consisted of two parts that moved to different directions: the bright structure appeared after the filament eruption which was moving to the east and the streamers appeared in the early stage of CME which was moving to the southeast. Although these two parts appeared at different time, they expanded outward as a whole at almost the same speed. As the CME expanded, it was clearly observed that both parts of the CME were loop-like structures and the loops were highly twisted. The structures of CMEs evolved rapidly. It provides some hints about the three dimensional structure of the CME.

In order to check the structure of the very bright region closely, an image enhancement technique has been applied to that region. The enhancement is achieved by using a frequency domain high-pass filter. Figure 7.2 shows the enhanced images. As this figure shows, there are very complex and delicate structures inside the bright region of the CME. It consisted of many highly twisted loops. Some loops showed complex structure too: they were made of many even thinner loops.

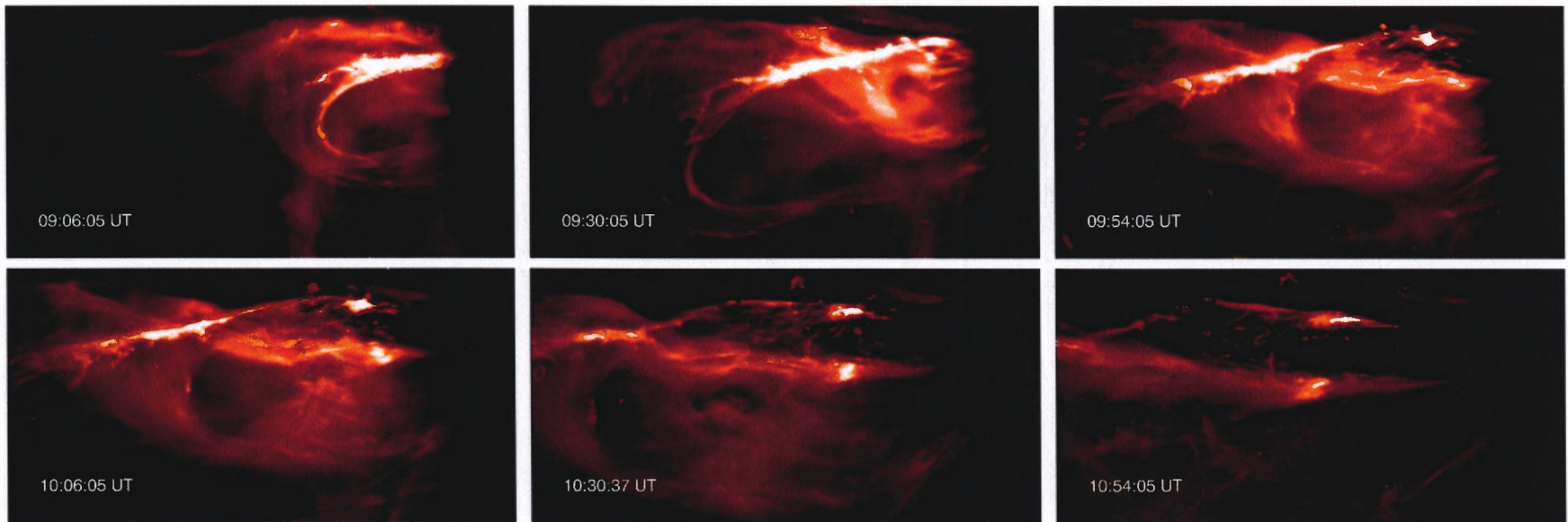


Figure 7.2 Enhanced LASC0 C2 images of the very bright region of the March 20, 2000 CME. The image enhancement was done by application of a high-pass filter. The detailed delicate structures of the CME are revealed. In the image of 08:30:05 UT, the helical lines are clearly demonstrated.

The height versus time of the CME are shown in Figure 7.3, 7.4 and 7.5. Figure 7.3 shows the height versus time measurement of the bright region that moved to the east. Because it appeared after the acceleration process, its speed reached about 800 km s^{-1} from the beginning of the plot. In Figure 7.4, the measurement is given for one of the loops that appeared in the C2 Coronagraph in the early stage of the CME. This loop was blocked in C3 Coronagraph. In Figure 7.5, height versus time measurement for another loop in the part which moved to the southeast is shown. It is very clear from these figures that beyond $6 R_{\odot}$ the speed of CME became almost constant. There is no obvious acceleration or de-acceleration up to $30 R_{\odot}$.

The CME appeared in the C3 Coronagraph at 09:18:05 UT. The entire structure described above maintained its shape until going out of the field view of C3 Coronagraph.

7.2.2 EIT Data

The EIT observation on March 20, 2000 showed that this CME was associated with a filament eruption and a 2B class flare (in active region NOAA #8921). The movie of EIT images revealed the change of the corona before the filament eruption, the flare and the CME very well. Figure 7.6 shows the time sequence of images of EIT observation of the filament eruption. Figure 7.7 shows the running difference images of the corresponding images in Figure 7.6.

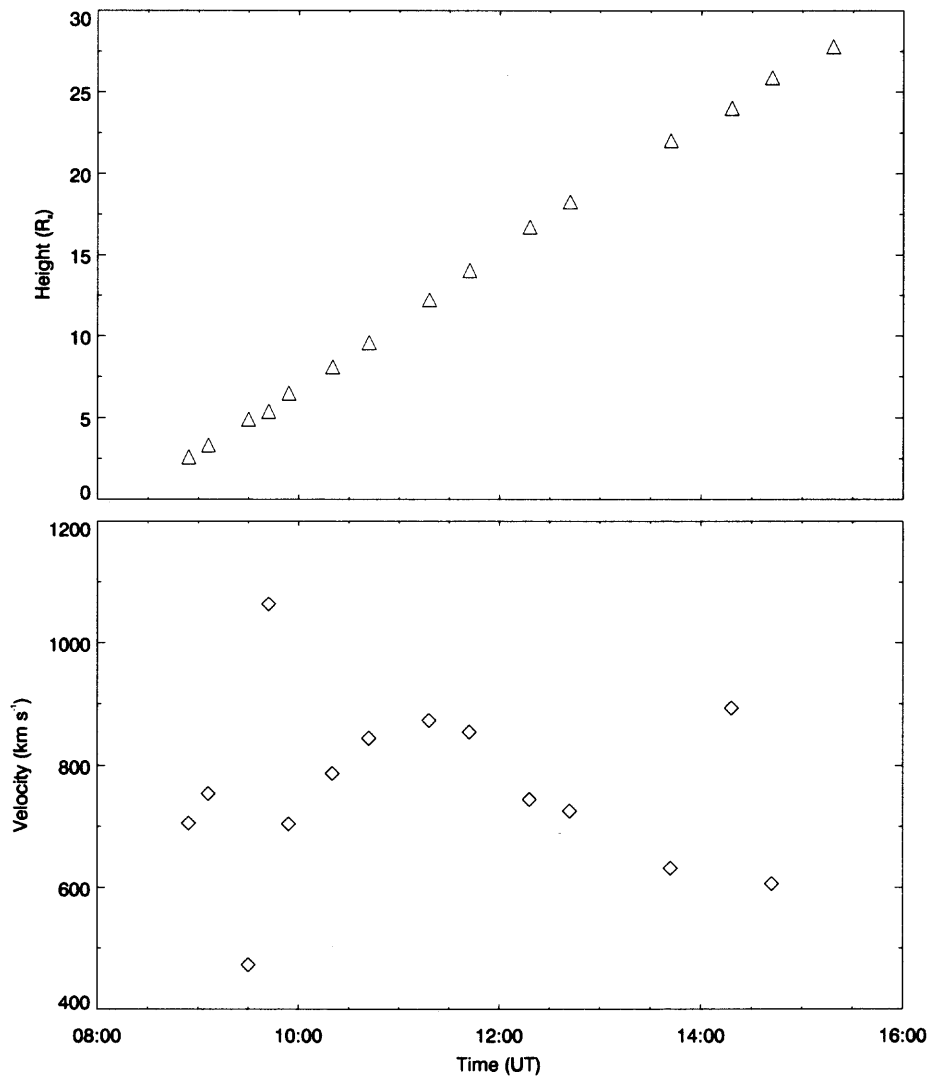


Figure 7.3 The upper panel shows the height vs. time plot of the upper group of loops near the equator of the Sun. R_{\odot} denotes the radius of the Sun. A loop that is easily tracked was chosen to derive the height-time plot. The lower panel shows the speed of the loop which is calculated using relation $v[i] = (h[i+1] - h[i]) / (t[i+1] - t[i])$. This group of loops came out of the occulting disk of the C2 coronagraph after the filament eruption and the flare. Their speed achieved several hundreds kilometer per second right after they appeared in the C2 images. Most of the measured speeds are below 1000 km s^{-1} and there is no obvious acceleration with the rising of the loops.

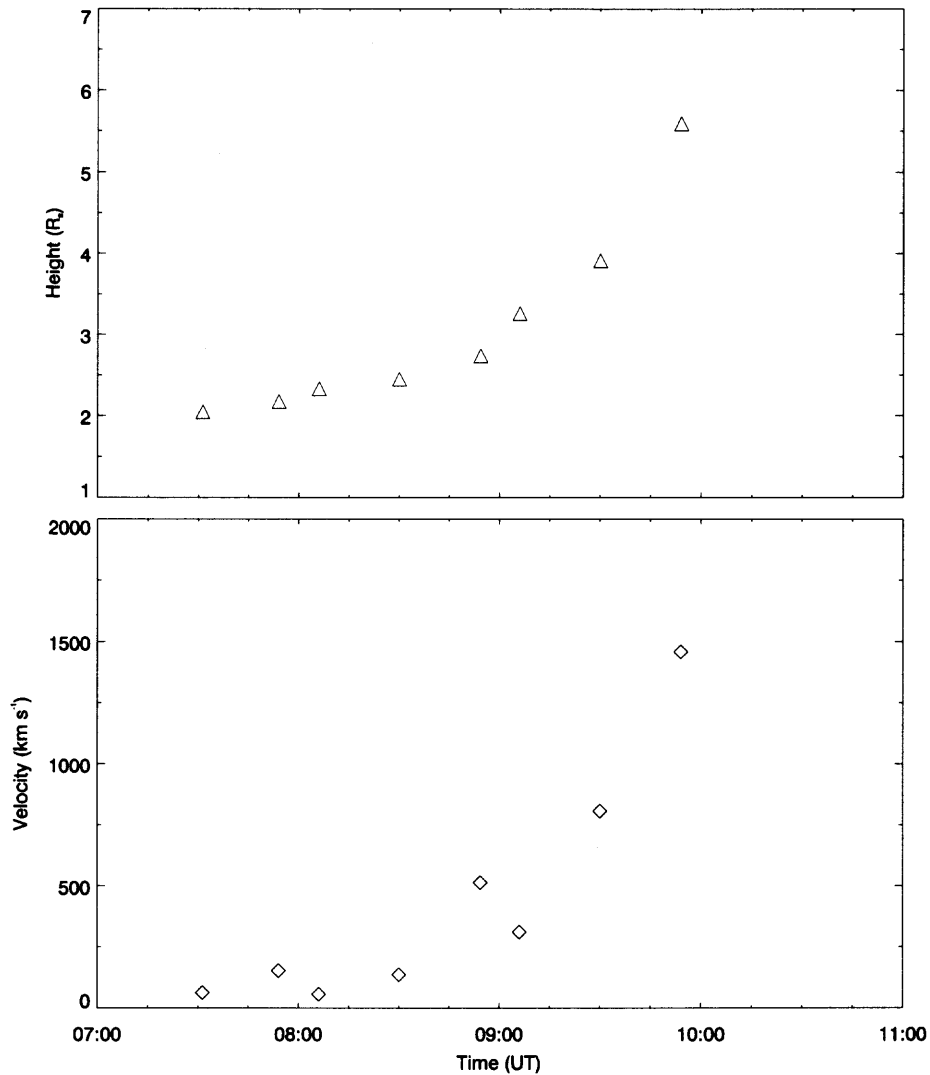


Figure 7.4 The upper panel shows the height vs. time plot of the middle group of loops. The lower panel shows the corresponding speed of the loops. This group of loops were the earliest coming out of the C2 occult disk. They were blocked in C3 images. From this figure, it can be seen that the CME expanded very slowly before the filament eruption. It got accelerated greatly after the filament eruption and the flare. The method to calculate the speed is described in Figure 7.3.

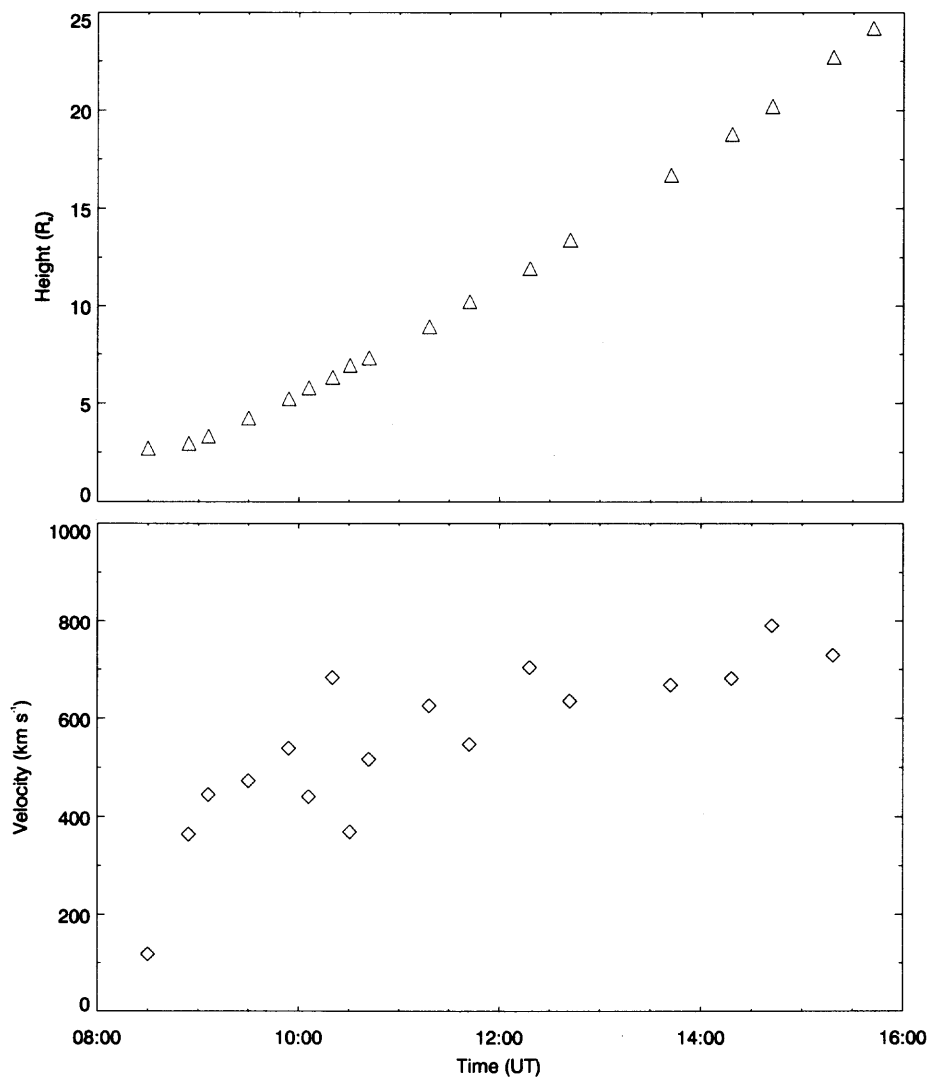


Figure 7.5 The upper panel shows the height vs. time plot of the group of loops in the far south of east limb.. The lower panel shows the corresponding speed of the loops. This group of loops appeared in the C2 images after the filament eruption and the flare.

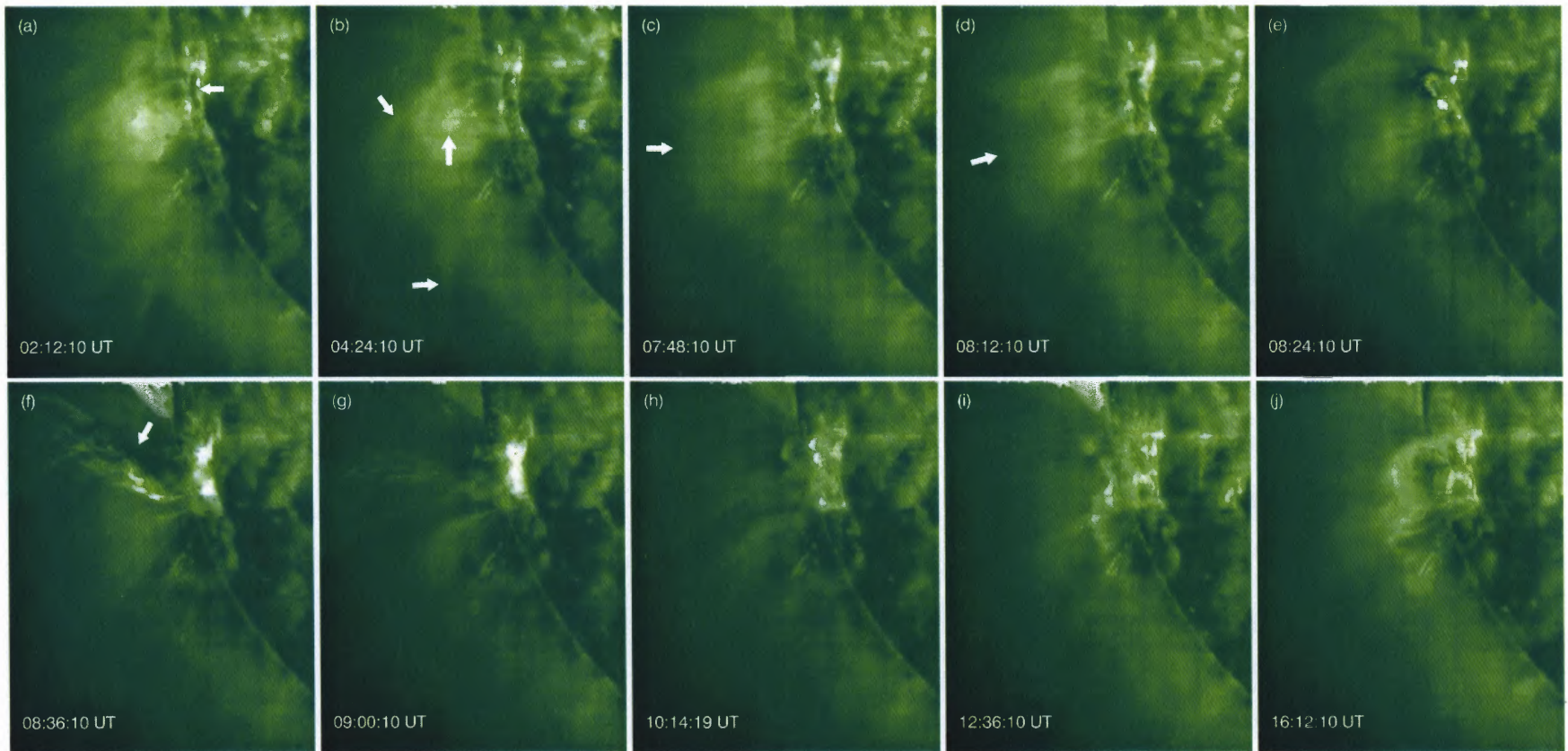


Figure 7.6 Sequences of EIT 195 Å images observed on March 20, 2000. In Frame (b), the upper and the lower arrows indicate two loops that expand afterwards. The arrow in the middle indicates the bright region prior to the CME. In Frame (c) and (d), the arrows indicate the location where the loops expand and open. The arrow In Frame (f) indicates the materials that probably came from the filament.

In EIT data, the filament appeared to be a dark feature that resided in active region NOAA #8921. The Figure 7.6 shows an EIT image of the filament and the active region. The filament is indicated by an arrow in Frame (a). In order to observe the magnetic structure underlying the filament, in Figure 7.8, the contour of MDI data at the nearest time available is overlaid on top of it. Time difference of the two data sets is about 3 mins. The solar rotation was corrected accordingly in the MDI data. The contour lines show the line-of-sight magnetic fields. Different polarities are denoted by the line colors. It is apparent that the filament lay over the neutral line of the magnetic fields.

Frame (e) of Figure 7.6 shows that the filament erupted at around 08:24:10 UT. However the active region was quite active even earlier than this. As early as 02:00:10 UT, some big, twisted loops showed very obvious outward motions. It can be seen very clearly that the loops rotated around an axis directed toward the Southeast from an EIT movie made the images. Due to the restriction of the FOV of EIT, it is impossible to determine whether the loops were open or closed. The rotation continued to at least 05:12:10 UT. Right over the filament and the active region, there were many smaller loops. These loops interacted with each other and were changing with time. From 05:48:10 UT, the whole system, including the bigger loops, and the smaller loops over the active region, seemed to start expanding outward. At 06:38:10 UT, the expanding speed of the group of loops accelerated significantly. The filament was also showing obvious changes with all these activity around it. The filament moved up very slowly with its volume increasing gradually. At last the filament erupted at 08:24:10 UT and two ribbons of bright regions formed on its two legs.

Figure 7.7 shows the running difference images of the EIT data for this event. There were some small dimming regions forming during the expansion of the loops (See Frame (a) and (b)). The dimming regions were moving outside, as showed in a movie made by the running difference images. At 08:12:10 UT, as the loops expanded suddenly, a huge dimming region formed above the active region. The filament began to erupt out at about

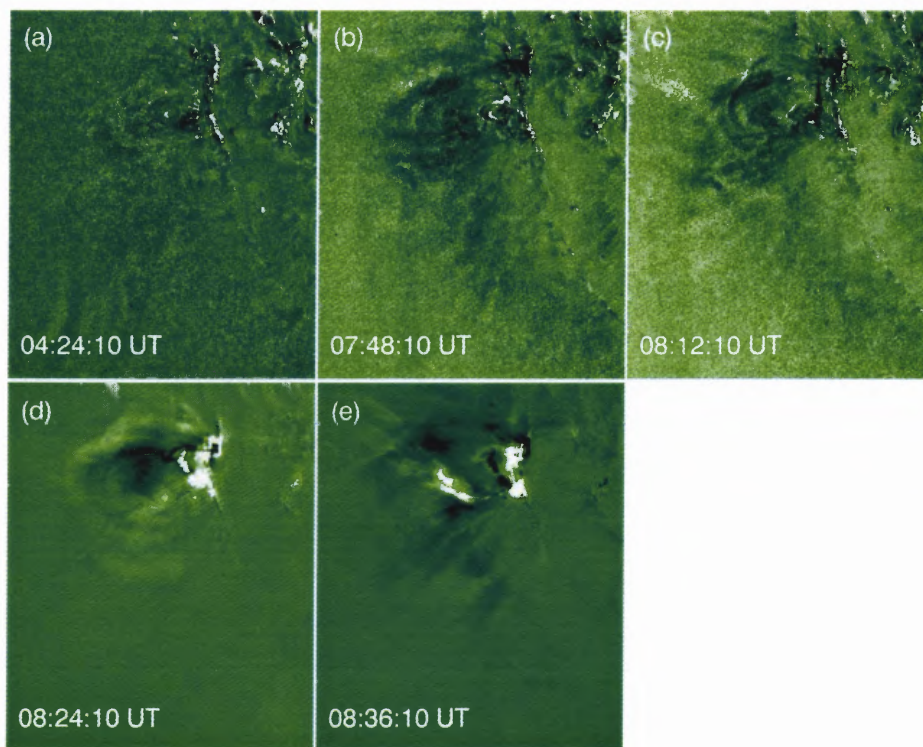


Figure 7.7 Running difference images of EIT. The EIT dimming regions can be seen above or near the filament.

08:24:10 UT. The flare happened at almost the same time when the filament erupted (according to data from the Solar Geophysical Data (SGD) archive, the flare began at 08:25). Frame (f) of Figure 7.6 shows (the arrow indicates the materials that probably coming from the filament) that as the dark materials stretched out there were also very bright materials thrown out at the same time. The ejected materials were moving very fast. However it is impossible to measure the speed accurately due to the low cadence of EIT images.

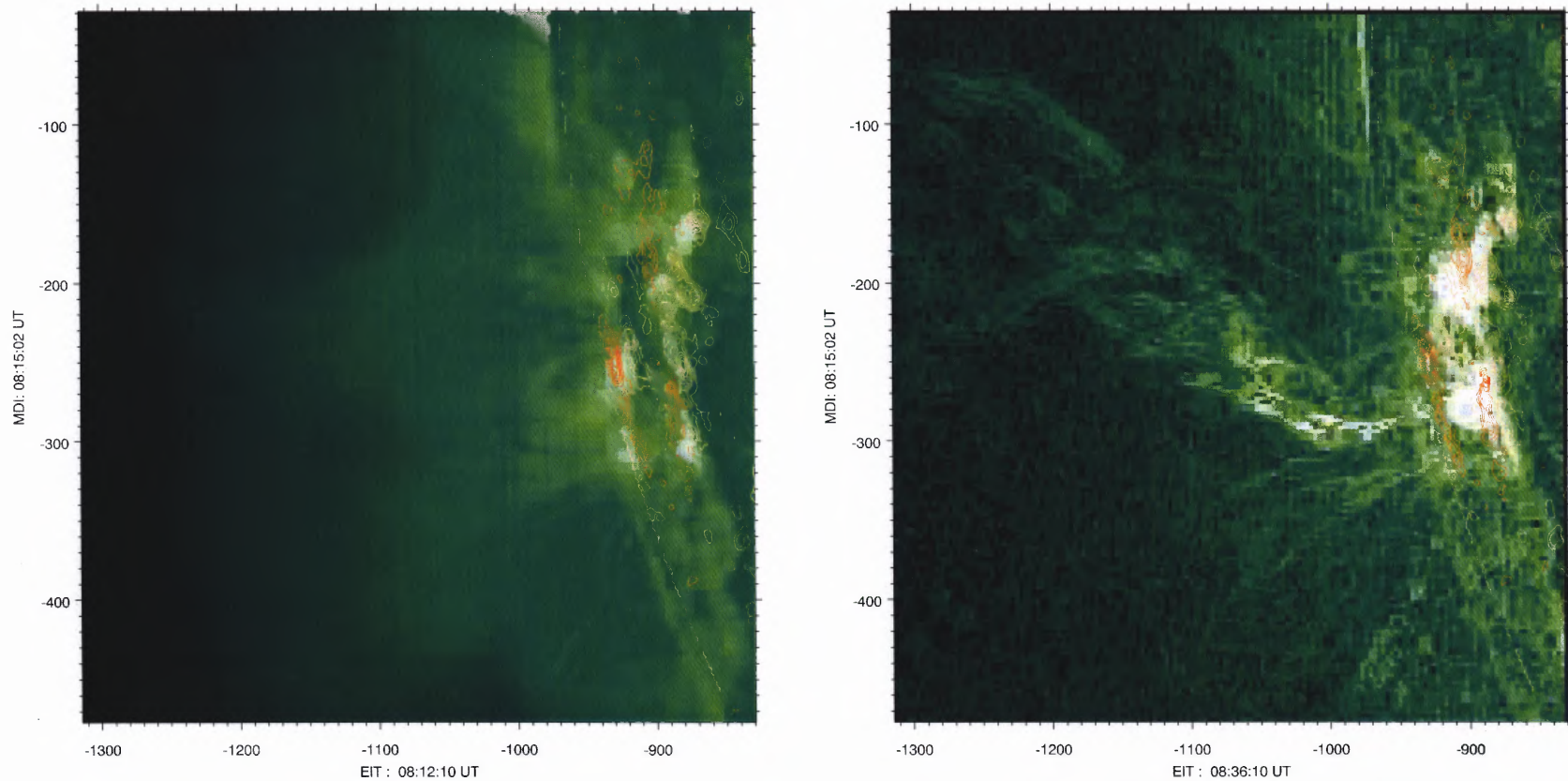


Figure 7.8 EIT 195 Å images are overlaid with MDI magnetogram contour lines. The MDI image was taken at 08:15:02 UT. In the left panel, the EIT image was taken at 08:12:10 UT. This image shows that the filament resided over a neutral line in the active region. The EIT image in the right panel was taken at 08:36:10 UT. An edge enhance filter was applied to this image to make loop structure of the erupted filament visible. In both panels the solar rotation of the MDI image was adjusted accordingly.

In order to study the magnetic field configuration of the active region, an MDI magnetogram is overlaid with EIT images. In Figure 7.8, the left panel shows an EIT image overlaid by a MDI magnetogram before the filament eruption. The rotation of the MDI data has been corrected (the time difference between the MDI magnetogram and the EIT image was about 11 minutes). It can be seen the filament was hanging over a neutral line in the active region. The right panel shows an edge-enhanced image of the EIT image at the moment the filament erupted, overlaid with the same MDI magnetogram in the left panel. The rotation of MDI data was also corrected accordingly. The twisted loops are shown very clearly in this figure. Figure 7.9 shows an effort to verify the correspondence of the filament with the inner part of the very bright region of the CME observed by C2 Coronagraph.

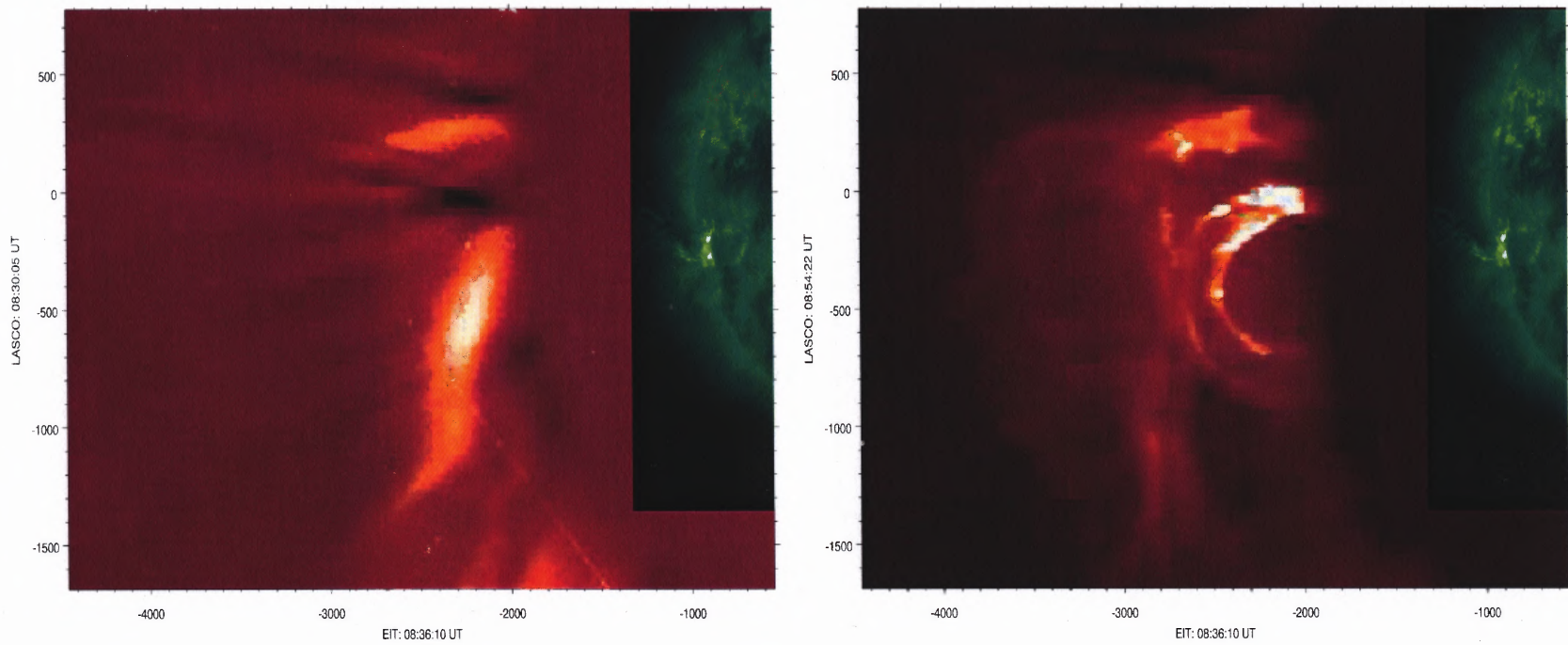


Figure 7.9 LASCO C2 images are overlaid with EIT 195 Å images. In the left panel, the LASCO image was 6 minutes earlier than the EIT image. In the right panel, the LASCO image was 18 minutes later than the EIT image. From this figure, it can be seen that the bright region that appeared in the LASCO C2 image might correspond to the filament.

The flare reached its maximum at 08:28 UT according to GOES X-Ray data. EIT data showed that from 09:36:10 UT post-flare loops were rising from the flare region. There seemed to be two sets of loops (Figure 7.6), one was over the active region where the flare happened, the other one was besides these loops. These loops exist until 12:36:10 UT. After that, they were replaced by one set of bigger loops as Figure 7.6 shows. These bigger loops kept rising until after 20:00 UT.

7.3 Discussion

Usually it is hard to determine the temporal relationship of associated filament eruption events and CMEs due to the low cadence of EIT and LASCO data. But for this event, the available data sets clearly showed that the CME initiated earlier than filament eruption. As Frame (a) of Figure 7.1 shows, there were streamers coming out from the C2 occulting disk even at 07:31 UT, nearly one hour before the filament eruption. The streamers expanded slowly before the filament erupted. Figure 7.4 shows that the speed of the streamers was only about several tens of kilometers per second. The CME accelerated suddenly (the mean acceleration is about 250 m s^{-2}) around the time of the filament eruption and the flare.

Before the filament eruption, EIT data already demonstrated rotation and expansion of loops over the active region. There was a two-ribbon flare that occurred almost at the same time as the filament eruption. This is consistent with Low (1996)'s interpretation in which CME is an ideal MHD expulsion process. When a CME has left the corona, the anchored part of the coronal magnetic field is stretched out into a fully open state. The magnetic reconnection of the opened field to close state results in the resistive heating and causes the two-ribbon flare. This mechanism of the two-ribbon flare was proposed even before the CMEs became well known (Hirayama 1974; Kopp & Pneuman 1976).

MacQueen & Fisher (1983) have concluded that there were two distinct classes of CMEs: one is associated with flares and the other is associated with eruptive events. Their statistical study showed that CMEs associated with flares have highest speeds, and show

little acceleration with height. On the other hand, CMEs which have eruptive-associated events are subjected to appreciable acceleration over radial heights of one or more solar radius above the solar limb. They argued that the CMEs associated with flares result from an impulsive, localized input to the corona. The CME studied in this chapter is a typical one that associated with both flare and filament eruption. It supports the above results. The speed of this CME approached as high as around 1000 km s^{-1} . The acceleration happened right after the filament eruption and the flare. From Figure 7.3, 7.4 and 7.5, it can be seen that the acceleration of this CME happened in very short time and in very small range of height.

Considering these observational facts, it can be proposed that magnetic reconnection plays a very important role in CME impulsive acceleration, although CMEs themselves can be initiated by other mechanisms. The changes of EIT images demonstrated may be an indication of the magnetic reconnection process. This reconnection process resulted in the flare event. The CME was accelerated right after the flare and filament eruption were initiated.

Because of the physical conditions in the corona, the structure of CMEs observed by coronagraph are believed to reflect the underlying magnetic structure of corona. Many of the theoretical models of CMEs show that an expanding flux rope is the underlying magnetic structure. Some simulations successfully derived the three parts structure that many CMEs manifest. But for this event, it does not have the standard three-part structure, i.e., the bright rim, the dark cavity and the compact bright region inside the cavity. This event is distinguished by highly twisted loops that were moving in different directions. The ends of the loops were clearly seen to be connected to the surface of the Sun even after it moved into the edge of field view of C3 Coronagraph.

Although the morphological structure of this CME is so different from the usual CMEs, the possible underlying magnetic structure is still an expanding flux rope. Firstly, this CME maintains its shape across the C2 and C3 coronagraph as most CMEs do. This is clearly showed from the LASCO data. The entire structure of the CME remained self

similar while it was expanding outward until it moved out of the field of view, which is about $30 R_{\odot}$. And the speed of this CME is consistent with other CMEs that have been confirmed to be an expanding flux rope. Second, the helical lines seen in Figure 7.2 give us a hint of the existence of the flux rope. From Figure 7.2, the helical structure of the CME can be seen very clearly. The reason that this CME did not show the usual three-part structure is that it is seen from a direction that is perpendicular to the plane of the flux rope. If it were viewed as usual from the side of the flux ropes, three components might be visible. The MDI data indicates that there is neutral line almost parallel to the limb of the Sun. The flux rope could be above and along this neutral line.

CHAPTER 8

SUMMARY AND DISCUSSION

As of the writing of this thesis, there were a number of X-class flares that erupted on the Sun within a short period of time. The geomagnetic storms caused by the CMEs associated with the flares produced severe hazardous effects on the Earth and spacecraft. A couple of Japanese communication satellites were reported to lose communications with the ground. The storms created some interference with the North American power grid. The eruptions interfered with radio transmissions in certain frequency bands, in particular those used for communication by the polar routed air crafts. And the intense solar activity also shut down a radiation-measuring instrument aboard NASA's 2001 Mars Odyssey orbiter and ground controllers have been unable to put it back in operation. Considering the great influence of the Sun on the space weather and hence on human beings, it is ultimately important to study the physics of various phenomena on the Sun and predict their effects on space weather.

In order to learn the fundamental astrophysical processes in the solar atmosphere, it is necessary to resolve the intrinsic scales of the various phenomena on the surface of the Sun. This drives the need for a large-aperture solar telescope. With the limitation of the Earth's atmosphere, simply increasing the aperture of the telescopes will be no use. Although high-order Adaptive Optics (AO) systems are being designed to mitigate part of the atmospheric turbulence effects, mature post-processing methods are still necessary to improve image quality even further. As demonstrated in Chapters 4 and 5, speckle masking imaging is a mature and powerful method in getting high resolution solar images. With the RTIR system (Chapter 3), the capabilities of monitoring solar active regions continuously are greatly improved. With the high resolution images derived from this system, the solar physicists can not only study the complicated structures and flows in active regions, but also predict space wether.

However, the image size of the current system, 1024×1024 , is still not good

enough. To cover an entire solar active region, larger size CCDs such as 2048×2048 pixels are needed. The current RTIR system cannot handle such a large amount of data. In order to solve this problem, either the computer system can be improved and be made more powerful to handle larger format images, or other more efficient post-processing methods can be used to mitigate the atmospheric effects on solar images. The phase diversity is another post-processing method that has been developed in the past decades. Phase diversity method requires simultaneous collection of two (or more) short-exposure images. Typically one of these images is a conventional focal-plane image that has been degraded by a unknown aberration. A second image of the same object is formed by perturbing the unknown aberrations in some known way, e.g., by defocussing. The estimate of the object and the aberration can be made from these two images. When speckle imaging and phase diversity methods are combined together, the method is called phase-diverse speckle imaging. The primary strengths of the two methods are combined in this new method. Phase-diverse speckle imaging techniques are particularly attractive for solar astronomy because they require relatively simple and inexpensive instrumentation. They perform well with relatively few images in high-signal regimes and lead to a joint estimation of the object and the wavefront.

Based on the success of the RITR system, a new real time system using phase-diverse speckle imaging is being developed by BBSO group. The new system will combine state-of-art parallel computing techniques with phase diverse speckle imaging techniques, to yield near real-time diffraction limited images with a cadence of approximately 10 sec. The parallel computer cluster will include 64 high speed Pentium processors. Observations will be made in the photospheric continuum, as well as in the G-band (around 4300\AA). High resolution magnetograms will be obtained by speckle inversion. This new system will complement and supplement the AO systems currently being developed at BBSO and National Solar Observatory (NSO). The hardware and data processing software of the parallel cluster will have direct application to the 4-meter ATST and the 1.6-m New Solar Telescope

(NST) at BBSO.

Although the exact physics processes involved in CMEs are still unknown, there is no doubt that at least some of CMEs have connections with filament eruptions. Bothmer & Schwenn (1994) and Rust (1994) showed that chirality and orientation of filament magnetic fields correspond to the chirality and orientation of the magnetic fields in magnetic clouds. Yurchyshyn et al. (2001) found that the geoeffectiveness of a CME is defined by the orientation and structure of the erupted filament. This means that a prediction can be made on whether a CME will cause magnetic storm on the Earth or not from observing the filament that is associated with it. While the result indicates that filament eruptions may not necessarily be related to CMEs, it is still important to study the relationship between filament eruptions and CMEs. The further study will be to identify the what kind of filaments are correlated to CMEs. High resolution observation will be likely to reveal magnetic structure of various eruptions. The study of the helical structure of CMEs can only be possible with diffraction limited observations.

REFERENCES

- Amari, T., Luciani, J. F., Mikic, Z., & Linker, J. 2000, *A Twisted Flux Rope Model for Coronal Mass Ejections and Two-Ribbon Flares*, *Astrophys. J. Lett.*, 529, L49.
- Babcock, H. W. 1953, *The Possibility of Compensating Astronomical Seeing*, *PASP*, 65, 229.
- Blanchflower, S. M., Rucklidge, A. M., & Weiss, N. O. 1998, *Modelling photospheric magnetoconvection*, *Mon. Not. R. Astron. Soc.*, 301, 593.
- Bothmer, V. & Schwenn, R. 1994, *Eruptive prominences as sources of magnetic clouds in the solar wind*, *Space Science Reviews*, 70, 215.
- Boyle, W. S. & Smith, G. E. 1993, in *Selected Papers on Instrumentation in Astronomy*, 475-+.
- Bray, R. J. & Loughhead, R. E. 1964, *Sunspots*, The International Astrophysics Series, London: Chapman & Hall, 1964.
- Brueckner, G. E., Delaboudiniere, J.-P., Howard, R. A., Paswaters, S. E., St. Cyr, O. C., Schwenn, R., Lamy, P., Simnett, G. M., Thompson, B., & Wang, D. 1998, *Geomagnetic storms caused by coronal mass ejections (CMEs): March 1996 through June 1997*, *Geophys. Res. Lett.*, 25, 3019.
- Brueckner, G. E., Howard, R. A., Koomen, M. J., Korendyke, C. M., Michels, D. J., Moses, J. D., Socker, D. G., Dere, K. P., Lamy, P. L., Llebaria, A., Bout, M. V., Schwenn, R., Simnett, G. M., Bedford, D. K., & Eyles, C. J. 1995, *The Large Angle Spectroscopic Coronagraph (LASCO)*, *Sol. Phys.*, 162, 357.
- Burlaga, L., Sittler, E., Mariani, F., & Schwenn, R. 1981, *Magnetic loop behind an interplanetary shock - Voyager, Helios, and IMP 8 observations*, *J. Geophys. Res.*, 86, 6673.
- Burlaga, L. F. 1988, *Magnetic clouds and force-free fields with constant alpha*, *J. Geophys. Res.*, 93, 7217.
- Chae, J., Denker, C., Spirock, T. J., Wang, H., & Goode, P. R. 2000, *High-Resolution H α Observations of Proper Motion in NOAA 8668: Evidence for Filament Mass Injection by Chromospheric Reconnection*, *Sol. Phys.*, 195, 333.
- Chen, J. 1996, *Theory of prominence eruption and propagation: Interplanetary consequences*, *J. Geophys. Res.*, 101, 27499.
- Chen, J. & Garren, D. A. 1993, *Interplanetary magnetic clouds: Topology and driving mechanism*, *Geophys. Res. Lett.*, 20, 2319.

- Chen, J., Howard, R. A., Brueckner, G. E., Santoro, R., Krall, J., Paswaters, S. E., St. Cyr, O. C., Schwenn, R., Lamy, P., & Simnett, G. M. 1997, *Evidence of an Erupting Magnetic Flux Rope: LASCO Coronal Mass Ejection of 1997 April 13*, *Astrophys. J. Lett.*, 490, L191+.
- Chen, J., Santoro, R. A., Krall, J., Howard, R. A., Duffin, R., Moses, J. D., Brueckner, G. E., Darnell, J. A., & Burkepile, J. T. 2000, *Magnetic Geometry and Dynamics of the Fast Coronal Mass Ejection of 1997 September 9*, *Astrophys. J.*, 533, 481.
- Choudhuri, A. R. 1986, *The dynamics of magnetically trapped fluids. I - Implications for umbral dots and penumbral grains*, *Astrophys. J.*, 302, 809.
- de Boer, C. R. 1993, *Speckle-Interferometrie und ihre Anwendungen auf die Sonnenbeobachtung*, Ph.D. Thesis.
- . 1996, *Noise filtering in solar speckle masking reconstructions.*, *Astron. Astrophys. Suppl.*, 120, 195.
- Delaboudiniere, J.-P., Artzner, G. E., Brunaud, J., Gabriel, A. H., Hochedez, J. F., Millier, F., Song, X. Y., Au, B., Dere, K. P., Howard, R. A., Kreplin, R., Michels, D. J., Moses, J. D., Defise, J. M., Jamar, C., Rochus, P., Chauvineau, J. P., Marioge, J. P., Catura, R. C., Lemen, J. R., Shing, L., Stern, R. A., Gurman, J. B., Neupert, W. M., Maucherat, A., Clette, F., Cugnon, P., & van Dessel, E. L. 1995, *EIT: Extreme-Ultraviolet Imaging Telescope for the SOHO Mission*, *Sol. Phys.*, 162, 291.
- Denker, C. 1997, *Two-dimensional speckle spectroscopy of the moustache phenomenon on the Sun.*, *Astron. Astrophys.*, 323, 599.
- . 1998, *Speckle Masking Imaging of Sunspots and Pores*, *Sol. Phys.*, 180, 81.
- Denker, C., de Boer, C. R., Volkmer, R., & Kneer, F. 1995, *Speckle masking imaging of the moustache phenomenon.*, *Astron. Astrophys.*, 296, 567.
- Denker, C., Didkovsky, L., Ma, J., Shumko, S., Varsik, J., Wang, J., Wang, H., & Goode, P. R. 2003, *Imaging magnetographs for high-resolution solar observations in the visible and near-infrared wavelength region*, *Astronomische Nachrichten*, 324, 332.
- Denker, C. & et al. 2001, in ASP Conf. Ser. 236: *Advanced Solar Polarimetry – Theory, Observation, and Instrumentation*, 463–+.
- Denker, C. & et al. 2002, in ASP Conf. Ser. 286: *Current Theoretical Models and Future High Resolution Solar Observations: Preparing for ATST*, 23–+.
- Denker, C. & et al. 2003, *To Be Determined*, *Astronomische Nachrichten*, 323, 3.
- Denker, C. & Wang, H. 1998, *High Spatial Resolution Observations of a Small delta SPOT*, *Astrophys. J.*, 502, 493.
- Denker, C., Yang, G., & Wang, H. 2001, *Near Real-Time Image Reconstruction*, *Sol. Phys.*, 202, 63.

- Dere, K. P., Brueckner, G. E., Howard, R. A., Michels, D. J., & Delaboudiniere, J. P. 1999, *LASCO and EIT Observations of Helical Structure in Coronal Mass Ejections*, *Astrophys. J.*, 516, 465.
- Didkovsky, L. & et al. 2003, *To Be Determined*, *Astronomische Nachrichten*, 323, 3.
- Fried, D. L. 1966, *Optical Resolution Through a Randomly Inhomogeneous Medium for Very Long and Very Short Exposures*, *Optical Society of America Journal*, 56, 1372.
- Frigo, M. & Johnson, S. G. 1998, in *Proc. IEEE Intl. Conf. on Acoustics, Speech, and Signal Processing*, Vol. 3, Seattle, WA, 1381–1384.
- Geist, A., Beguelin, A., Jiang, W., Mancheck, R., & Sunderam, V. 1994, *PVM: Parallel Virtual Machine: A Users' Guide and Tutorial for Networked Parallel Computing*, MIT Press, New York.
- Giovanelli, R. G. 1982, *Sunspot geometry and pressure balance*, *Sol. Phys.*, 80, 21.
- Goode, P. R., Wang, H., Marquette, W. H., & Denker, C. 2000, *Measuring Seeing from Solar Scintillometry and the Spectral Ratio Technique*, *Sol. Phys.*, 195, 421.
- Goodman, J. W. 1985, *Statistical optics*, New York: Wiley, 1985.
- Gopalswamy, N., Shimojo, M., Lu, W., Yashiro, S., Shibasaki, K., & Howard, R. A. 2003, *Prominence Eruptions and Coronal Mass Ejection: A Statistical Study Using Microwave Observations*, *Astrophys. J.*, 586, 562.
- Gosling, J. T., Hildner, E., MacQueen, R. M., Munro, R. H., Poland, A. I., & Ross, C. L. 1974, *Mass ejections from the sun - A view from SKYLAB*, *J. Geophys. Res.*, 79, 4581.
- Gosling, J. T., McComas, D. J., Phillips, J. L., & Bame, S. J. 1991, *Geomagnetic activity associated with earth passage of interplanetary shock disturbances and coronal mass ejections*, *J. Geophys. Res.*, 96, 7831.
- Harrison, R. A. 1994, *A statistical study of the coronal mass ejection phenomenon*, *Advances in Space Research*, 14, 23.
- Hirayama, T. 1974, *Theoretical Model of Flares and Prominences. I: Evaporating Flare Model*, *Sol. Phys.*, 34, 323.
- Hirzberger, J., Vazquez, M., Bonet, J. A., Hanslmeier, A., & Sobotka, M. 1997, *Time Series of Solar Granulation Images. I. Differences between Small and Large Granules in Quiet Regions*, *Astrophys. J.*, 480, 406.
- Howard, R. A., Sheeley, N. R., Michels, D. J., & Koomen, M. J. 1985, *Coronal mass ejections - 1979-1981*, *J. Geophys. Res.*, 90, 8173.
- Hundhausen, A. 1999, in *The many faces of the sun: a summary of the results from NASA's Solar Maximum Mission.*, 143–+.

- Illing, R. M. E. & Hundhausen, A. J. 1983, *Possible observation of a disconnected magnetic structure in a coronal transient*, J. Geophys. Res., 88, 10210.
- Jones, H. P., Duvall, T. L., Harvey, J. W., Mahaffey, C. T., Schwitters, J. D., & Simmons, J. E. 1992, *The NASA/NSO spectromagnetograph*, Sol. Phys., 139, 211.
- Kahler, S. W. 1992, *Solar flares and coronal mass ejections*, Annu. Rev. Astron. Astrophys., 30, 113.
- Keil, S. L., Rimmele, T., Keller, C. U., Hill, F., Radick, R. R., Oschmann, J. M., Warner, M., Dalrymple, N. E., Briggs, J., Hegwer, S. L., & Ren, D. 2003, in *Innovative Telescopes and Instrumentation for Solar Astrophysics*. Edited by Stephen L. Keil, Sergey V. Avakyan . Proceedings of the SPIE, Volume 4853, pp. 240-251 (2003), 240–251.
- Keller, C. U. 1995, *Properties of Solar Magnetic Fields from Speckle Polarimetry. (Ludwig Biermann Award Lecture 1994)*, Reviews of Modern Astronomy, 8, 27.
- Kentischer, T. J., Schmidt, W., Sigwarth, M., & Uexkuell, M. V. 1998, *TESOS, a double Fabry-Perot instrument for solar spectroscopy*, Astron. Astrophys., 340, 569.
- Knox, K. T. & Thompson, B. J. 1974, *Recovery of images from atmospherically degraded short-exposure photographs*, Astrophys. J. Lett., 193, L45.
- Kopp, R. A. & Pneuman, G. W. 1976, *Magnetic reconnection in the corona and the loop prominence phenomenon*, Sol. Phys., 50, 85.
- Korff, D. 1973, *Analysis of a Method for Obtaining Near Diffraction Limited Information in the Presence of Atmospheric Turbulence*, Optical Society of America Journal, 63, 971.
- Kuhn, J. R., Lin, H., & Loranz, D. 1991, *Gain calibrating nonuniform image-array data using only the image data*, PASP, 103, 1097.
- Kumar, A. & Rust, D. M. 1996, in ASP Conf. Ser. 95: *Solar Drivers of the Interplanetary and Terrestrial Disturbances*, 315–+.
- Labeyrie, A. 1970, *Attainment of Diffraction Limited Resolution in Large Telescopes by Fourier Analysing Speckle Patterns in Star Images*, Astron. Astrophys., 6, 85.
- Leka, K. D. & Skumanich, A. 1998, *The Evolution of Pores and the Development of Penumbrae*, Astrophys. J., 507, 454.
- Leka, K. D. & Steiner, O. 2001, *Understanding Small Solar Magnetic Structures: Comparing Numerical Simulations to Observations*, Astrophys. J., 552, 354.
- Lohmann, A. W., Weigelt, G., & Wirmitzer, B. 1983, *Speckle masking in astronomy - Triple correlation theory and applications*, Appl. Opt., 22, 4028.
- Low, B. C. 1996, *Solar Activity and the Corona*, Sol. Phys., 167, 217.

- MacQueen, R. M. & Fisher, R. R. 1983, *The kinematics of solar inner coronal transients*, Sol. Phys., 89, 89.
- Mouradian, Z., Soru-Escout, I., & Pojoga, S. 1995, *On the two classes of filament-prominence disappearance and their relation to coronal mass ejections*, Sol. Phys., 158, 269.
- Nindos, A. & Zirin, H. 1998, *Properties and Motions of Ellerman Bombs*, Sol. Phys., 182, 381.
- November, L. J. & Simon, G. W. 1988, *Precise proper-motion measurement of solar granulation*, Astrophys. J., 333, 427.
- Parker, E. N. 1979, *Sunspots and the physics of magnetic flux tubes. IX - Umbral dots and longitudinal overstability*, Astrophys. J., 234, 333.
- Pehlemann, E. & von der Luehe, O. 1989, *Technical aspects of the speckle masking phase reconstruction algorithm*, Astron. Astrophys., 216, 337.
- Qiu, J., Ding, M. D., Wang, H., Denker, C., & Goode, P. R. 2000, *Ultraviolet and H α Emission in Ellerman Bombs*, Astrophys. J. Lett., 544, L157.
- Rucklidge, A. M., Schmidt, H. U., & Weiss, N. O. 1995, *The abrupt development of penumbrae in sunspots*, Mon. Not. R. Astron. Soc., 273, 491.
- Rust, D. M. 1994, *Spawning and shedding helical magnetic fields in the solar atmosphere*, Geophys. Res. Lett., 21, 241.
- Scharmer, G., Owner-Petersen, M., Korhonen, T., & Title, A. 1999, in ASP Conf. Ser. 183: High Resolution Solar Physics: Theory, Observations, and Techniques, 157–+.
- Schlichenmaier, R. & Collados, M. 2002, *Spectropolarimetry in a sunspot penumbra. Spatial dependence of Stokes asymmetries in Fe I 1564.8 nm*, Astron. Astrophys., 381, 668.
- Schlichenmaier, R., Jahn, K., & Schmidt, H. U. 1998, *Magnetic flux tubes evolving in sunspots. A model for the penumbral fine structure and the Evershed flow*, Astron. Astrophys., 337, 897.
- Shine, R. A., Title, A. M., Tarbell, T. D., Smith, K., Frank, Z. A., & Scharmer, G. 1994, *High-resolution observations of the Evershed effect in sunspots*, Astrophys. J., 430, 413.
- Sobotka, M., Bonet, J. A., & Vazquez, M. 1993, *A High-Resolution Study of Inhomogeneities in Sunspot Umbrae*, Astrophys. J., 415, 832.
- Sobotka, M., Bonet, J. A., Vazquez, M., & Hanslmeier, A. 1995, *On the Dynamics of Bright Features in Sunspot Umbrae*, Astrophys. J. Lett., 447, L133+.

- Sobotka, M., Brandt, P. N., & Simon, G. W. 1997, *Fine structure in sunspots. I. Sizes and lifetimes of umbral dots*, *Astron. Astrophys.*, 328, 682.
- . 1999a, *Fine structure in sunspots. III. Penumbral grains*, *Astron. Astrophys.*, 348, 621.
- Sobotka, M., Vázquez, M., Bonet, J. A., Hanslmeier, A., & Hirzberger, J. 1999b, *Temporal Evolution of Fine Structures in and around Solar Pores*, *Astrophys. J.*, 511, 436.
- Solanki, S. K., Ruedi, I. K., & Livingston, W. 1992, *Infrared lines as probes of solar magnetic features. II - Diagnostic capabilities of Fe I 15648.5 Å and 15652.9 Å*, *Astron. Astrophys.*, 263, 312.
- Spirock, T. & et al. 2001, in ASP Conf. Ser. 236: *Advanced Solar Polarimetry – Theory, Observation, and Instrumentation*, 65–+.
- Stachnik, R. V., Nisenson, P., Ehn, D. C., Hudgin, R. H., & Schirf, V. E. 1977, *Speckle image reconstruction of solar features*, *Nature*, 266, 149.
- Stellmacher, G. & Wiehr, E. 1991, *Modelling the moustache phenomenon in network regions*, *Astron. Astrophys.*, 251, 675.
- Strous, L. H., Scharmer, G., Tarbell, T. D., Title, A. M., & Zwaan, C. 1996, *Phenomena in an emerging active region. I. Horizontal dynamics.*, *Astron. Astrophys.*, 306, 947.
- Thomas, J. H. & Weiss, N. O., eds. 1992, *Sunspots: Theory and observations; Proceedings of the NATO Advanced Research Workshop on the Theory of Sunspots*, Cambridge, United Kingdom, Sept. 22-27, 1991.
- Title, A. M., Tarbell, T. D., Topka, K. P., Ferguson, S. H., Shine, R. A., & SOUP Team. 1989, *Statistical properties of solar granulation derived from the SOUP instrument on Spacelab 2*, *Astrophys. J.*, 336, 475.
- Varsik, J. R. 1995, *Calibration of the Big Bear Videomagnetograph*, *Sol. Phys.*, 161, 207.
- Volkmer, R., von der Luehe, O., Kneer, F., Staude, J., Hofmann, A., Schmidt, W., Sobotka, M., Soltau, D., Wiehr, E., Wittmann, A., & Berkefeld, T. 2003, in *Innovative Telescopes and Instrumentation for Solar Astrophysics*. Edited by Stephen L. Keil, Sergey V. Avakyan . *Proceedings of the SPIE*, Volume 4853, pp. 360-369 (2003)., 360–369.
- von der Luehe, O. 1984, *Estimating Fried's parameter from a time series of an arbitrary resolved object imaged through atmospheric turbulence*, *Optical Society of America Journal*, 1, 510.
- . 1993, *Speckle imaging of solar small scale structure. I - Methods*, *Astron. Astrophys.*, 268, 374.
- Wang, H., Denker, C., Spirock, T., Goode, P. R., Yang, S., Marquette, W., Varsik, J., Fear, R. J., Nenow, J., & Dingley, D. D. 1998, *New Digital Magnetograph At Big Bear Solar Observatory*, *Sol. Phys.*, 183, 1.

- Wang, H. & Zirin, H. 1992, *Flows around sunspots and pores*, Sol. Phys., 140, 41.
- Weigelt, G. & Wirtitzer, B. 1983, *Image reconstruction by the speckle-masking method*, Optics Letters, 8, 389.
- Weigelt, G. P. 1977, *Modified astronomical speckle interferometry 'speckle masking'*, Optics Communications, 21, 55.
- Weiss, N. O., Brownjohn, D. P., Matthews, P. C., & Proctor, M. R. E. 1996, *Photospheric Convection in Strong Magnetic Fields*, Mon. Not. R. Astron. Soc., 283, 1153.
- Williams, R. E., Blacker, B. S., Dickinson, M., Ferguson, H. C., Fruchter, A. S., Giavalisco, M., Gilliland, R. L., Lucas, R. A., McElroy, D. B., Petro, L. D., & Postman, M. 1996, in *Science with the Hubble Space Telescope - II*, 33–+.
- Wilson, R. M. & Hildner, E. 1984, *Are interplanetary magnetic clouds manifestations of coronal transients at 1 AU?*, Sol. Phys., 91, 169.
- Wood, B. E., Karovska, M., Chen, J., Brueckner, G. E., Cook, J. W., & Howard, R. A. 1999, *Comparison of Two Coronal Mass Ejections Observed by EIT and LASCO with a Model of an Erupting Magnetic Flux Rope*, Astrophys. J., 512, 484.
- Wu, S. T., Guo, W. P., & Dryer, M. 1997, *Dynamical Evolution of a Coronal Streamer - Flux Rope System - II. A Self-Consistent Non-Planar Magnetohydrodynamic Simulation*, Sol. Phys., 170, 265.
- Wu, S. T., Guo, W. P., Michels, D. J., & Burlaga, L. F. 1999, *MHD description of the dynamical relationships between a flux rope, streamer, coronal mass ejection, and magnetic cloud: An analysis of the January 1997 Sun-Earth connection event*, J. Geophys. Res., 104, 14789.
- Yang, G., Xu, Y., Denker, C., & Wang, H. 2003, *High-Spatial Resolution Observations of Pores and the Formation of a Rudimentary Penumbra*, Astrophys. J., in press.
- Yi, Z. & Molowny-Horas, R. 1995, *Correlation tracking technique for measurement of transverse chromospheric motions*, Astron. Astrophys., 295, 199.
- Yurchyshyn, V. B., Wang, H., Goode, P. R., & Deng, Y. 2001, *Orientation of the Magnetic Fields in Interplanetary Flux Ropes and Solar Filaments*, Astrophys. J., 563, 381.
- Zirin, H. & Mosher, J. M. 1988, *The Caltech solar site survey, 1965-1967*, Sol. Phys., 115, 183.
- Zwaan, C. 1987, *Elements and patterns in the solar magnetic field*, Annu. Rev. Astron. Astrophys., 25, 83.